Title	Photo-electrochemical Etching of Nitride Semiconductors for Electron Device Application
Author(s)	渡久地，政周
Degree Grantor	北海道大学
Degree Name	博士(工学)
Dissertation Number	甲第15073号
Issue Date	2022-03-24
DOI	https://doi.org/10.14943/doctoral.k15073
Doc URL	https://hdl.handle.net/2115/85235
Type	doctoral thesis
File Information	Masachika_Toguchi.pdf

Doctoral Dissertation

Photo-electrochemical Etching of Nitride Semiconductors for Electron Device Applicaiton

（窒化物半導体に対する光電気化学エッチングと電子デバイス応用）

Masachika Toguchi

Graduate School of information Science and Technology,
Hokkaido University

－ 2022 －

Doctoral Dissertation

Photo-electrochemical Etching of Nitride Semiconductors for Electron Device Applicaiton

（窒化物半導体に対する光電気化学エッチングと電子デバイス応用）

A dissertation submitted in partial fulfillment of the requirement for
the degree of Doctor of Philosophy (Engineering)
to Hokkaido University

February, 2022

by

Masachika Toguchi

Graduate School of information Science and Technology,
Hokkaido University

Dissertation Supervisor
Professor Taketomo SATO

HOKKAIDO
UNIVERSITY

Acknowledgements

This dissertation describes a research work carried out at Research Center for Integrated Quantum Electronics (RCIQE) under the supervision of Prof. Taketomo Sato, while I was the graduate student of the Graduate School of Information Science Technology, Hokkaido University, from 2018 to 2022.

I would like to express my deepest gratitude to Prof. Taketomo Sato for giving me the opportunity to work in RCIQE and for spending a lot of time on supporting my research, including guidance of experiment, advices for my research plans, discussions on experimental results, and instructive corrections of my research papers and presentations. Thanks to his enthusiasm supports and encouragements, I was able to have an invaluable experience that will be of great help to my future work.

I would like to acknowledge the chief examiner and the co-examiners of my dissertation, Prof. Junichi Motohisa, Prof. Tamotsu Hashizume, and Prof. Seiya Kasai, for spending their precious time on reviewing my dissertation and providing valuable suggestions that helped me to improve the quality of dissertation. I would also like to acknowledge other members of my dissertation committee, Prof. Kazuhisa Sueoka, Prof. Megumi Akai, Prof. Tetsuya Asai, Prof. Masayuki Ikebe, Prof. Tetsuya Uemura, Prof. Hiromichi Ohta, Prof. Hiroki Habazaki for reviewing my dissertation and giving me valuable comments at dissertation defense.

I would like to acknowledge Prof. Shinjiro Hara, Prof. Masamichi Akazawa, Prof. Katsuhiro Tomioka for their guidance and supports. I could do a productive research because they create and maintain a wonderful research environment, RCIQE.

I would also like to thank everyone who collaborated with me, Dr. Fumimasa and Mr. Noboru Fukuhara from SCIOCS Corporation, Mr. Sadaharu Yagyu and Mr. Hiroaki Hayashi from Mitsubishi Electric Corporation, Dr. Hiroshi Amano, Dr. Yoshio Honda and Dr. Manato Deki from Nagoya University, and Dr. Makoto Miyoshi from Nagoya Institute of Technology, and others. Thanks to your support and discussions with you, my research was able to progress efficiently and produce meaningful results.

I am very grateful to the current members of EC group, Mr. Kosaku Ito, Mr.

Hiroki Ogami, Mr. Kota Kubo, Mr. Yuto Osawa, Mr. Takuya Togashi and Mr. Ryota Ochi, and the former members, Mr. Keisuke Uemura, Mr. Keisaku Ito, Mr. Satoru Matsumoto, Mr. Hirofumi Kida, Ms. Sayaka Ohmi, Mr. Xiaoyi Zhang, Mr. Masaaki Edamoto and Dr. Yusuke Kumasaki for their countless supports, including guidance of experiments, constructive discussions at weekly meetings, and kind personal consultations.

I am also grateful to my seniors, Dr. Kenya Nishiguchi, Dr. Shota Kaneki, Dr. Kenta Saito and Dr. Ryoma Horiguchi, my peers, Mr. Kazuki Inada, Mr. Katsuma Shimizu, Mr. Yuji Ando, Mr. Katsuya Iida, Mr. Tatsuya Oyobiki, Mr. Tetsuro Kadowaki, Mr. Hajime Uetake, Mr. Shohei Kitajima, Mr. Yuya Yamamoto, Mr. Masahiro Sasaki, Mr. Yusuke Minami and Mr. Michihito Shimauchi, my juniors and everyone who has interacted with me. Thanks to all of you, I was able to have a fun and productive student life.

Special thanks go to people who have (had) belonged to RCIQE. I would like to thank technicians and secretaries, Mr. Nobuyuki Miyazaki, Mr. Kiyotake Nagakura, Ms. Mizuho Tanaka, and Ms. Chieko Akiyama, for their countless supports. I could not accomplish my research without the dedicated help of all the members of RCIQE.

I would like to express my appreciation to the Japan Society for the Promotion of Science (JSPS) that supported me financially through the Research Fellowships for Young Scientists from 2020 to 2022.

Finally, I wish to dedicate this work to my family, Hajime Toguchi, Wakae Toguchi, Rina Toguchi, Rika Toguchi and Crystal, whose encouragement helped me keep trying.

This research was made possible by the warm support of many people, including those whose names I have not included here. Finally, I would like to thank once again all the people who have supported me in every way.

February 14, 2021

Masachika Toguchi

Contents

Chapter 3:
Experimental technique 27

Chapter 4:
Anisotropic Photo-electrochemical etching for low-doped GaN 49

Chapter 5:

Chapter 6:

Chapter 7:

Chapter 1

Introduction

1.1. Background

1.1.1. A state of power electronics

In recent years, our lives have been undergoing a transition from the traditional lifestyle, which is often referred to as the "fourth industrial revolution [1]," and policies are being implemented to realize a "super-smart society (Society 5.0)," where all people and things are connected by IoT to share vast amounts of data, which will be used to develop the economy and solve various social issues by digitizing various parts of our lives, such as remote work, cashless, IoT, and smart cities. As a result, the use of electric and electronic devices is expected to continue to increase. The increase in the utilization rate is naturally directly related to the consumption of energy, and it is expected that the electrical energy consumption of electrical and electronic devices will continue to increase in the future. However, Japan's current power generation methods are largely dependent on thermal power generation[2] using coal, oil, and natural gas, and the increase in supply against the increase in demand for electrical energy will lead to environmental problems such as global warming. Therefore, energy conservation by improving the efficiency of power usage is being considered as one of the most important issues. In order to save energy in electrical and electronic equipment, it is essential to improve the performance of power devices and systems that are responsible for converting and controlling power. Currently, silicon (Si) Metal-Oxide-Semiconductor (MOS) transistors are the mainstream of power devices, but as Si is already approaching its physical limits, the use of new semiconductor materials is being widely considered for innovative performance improvement of transistors.

1.1.2. A state of wireless communication

The transition in lifestyle is also affecting the field of wireless communication systems. The explosive spread of mobile communication devices such as smartphones has led to a rapid increase in the volume of mobile communication traffic. Fig. 1.1 shows the transition of the volume of mobile communication traffic over the past 10 years.

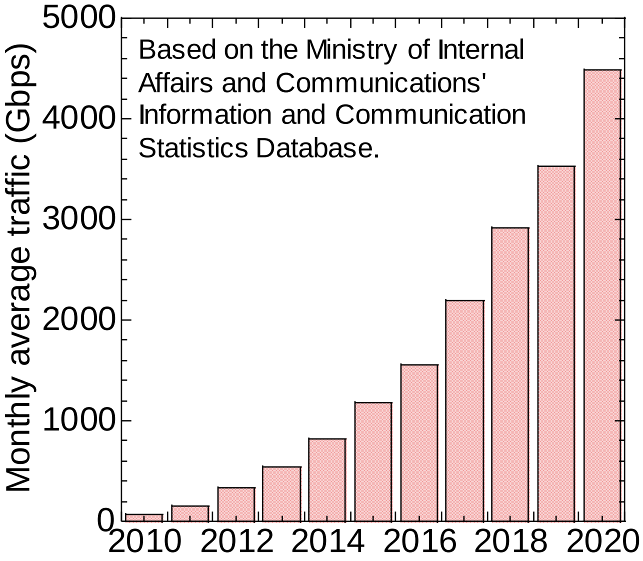

Fig.1.1 the transition of the volume of mobile communication traffic over the past 10 years [3].

As the figure clearly shows, the traffic volume has been increasing rapidly year by year, and this trend is expected to continue thereafter. As a result, the 4th generation mobile communication technologies (4G) such as LTE and LTE-Advanced, which have been used in the past, will not be able to withstand the traffic volume and will become overwhelmed. In addition, as the IoT mentioned above becomes more widespread, it is expected that everything will communicate with each other in the future, and the number of devices connected to the Internet will become enormous. In addition, when the IoT is applied to fields such as medical care and disasters, not only will data capacity increase, but also high reliability and ultra-low latency performance will be required.

In 2020, the 5th generation mobile communication (5G) was put into practical use to meet the above requirements. However, no mobile communication technology has yet been developed that can meet all three requirements of 5G: high-speed, high-capacity communication, ultra-mass terminal connections, and ultra-reliability. In particular, in 5G, high-frequency devices that can support high-speed and high-capacity communications have not yet been commercialized, and the emergence of new devices that can withstand the 5G environment is required. In September 2015, the ITU formulated the IMT Vision Recommendation, which summarizes the main capabilities and concepts of 5G. In September 2015, the ITU formulated the IMT Vision Recommendation 4), which summarizes the main capabilities and concepts of 5G. The main requirements for 5G communication devices are shown in Figure 1.2.

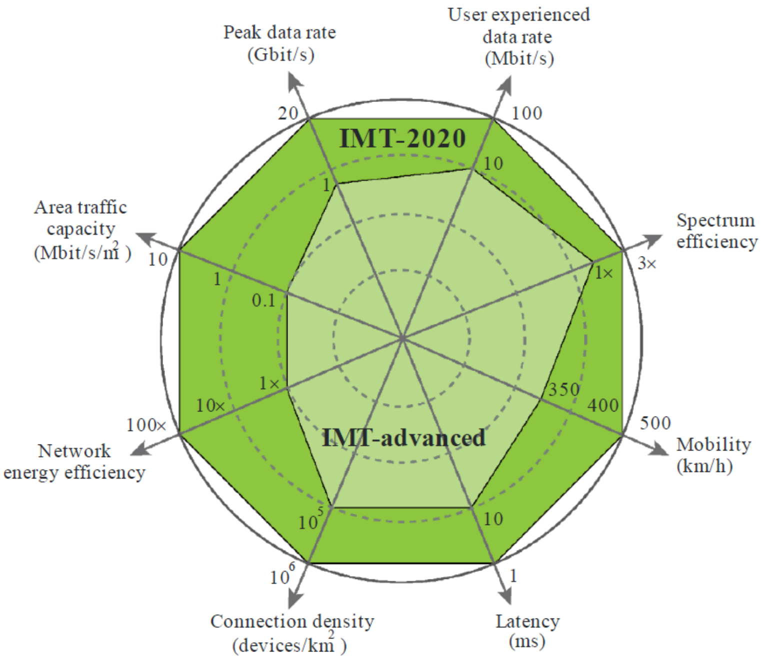

Fig.1.2 Requirements for 5G in IMT Vision Recommendations4)

Specifically, the requirements are as follows: (1) High speed communication: While 4G communication speed was up to about 1 Gbps for downlink and several hundred Mbps for uplink, the requirements for 5G are up to about 20 Gbps for downlink and 10 Gbps for uplink, more than 10 times faster than 4G, (2) Ultra-low latency communication: The latency in 5G is estimated to be around 1 millisecond, which is about one-tenth that of 4G; (3) Multiple simultaneous connections: In contrast to 4G, where around 100,000 terminals per km2 can be connected simultaneously, 5G requires around 1 million terminals per km2 to be connected simultaneously. In the IoT era, this means that even if there are a huge number of sensors and terminals (e.g., smart factories, smart meters, infrastructure maintenance and management), there should be no interruption in communication. 5G communication terminals are required to have 10 times higher performance than 4G. In order to meet this requirement, InP-based devices that can operate in submillimeter to millimeter waves have problems such as insufficient breakdown voltage due to their narrow forbidden band width, making it difficult to achieve high output power.

1.1.3. Application of Nitride Semiconductors

In order to meet the above requirements in the field of power devices and high frequency devices, nitride semiconductors such as gallium nitride (GaN) are currently attracting attention as a new semiconductor material. The crystalline properties of GaN include short bond lengths, wide band gaps, and strong interatomic bonding energies, which provide GaN-based devices with advantages over Si devices in terms of thermal, chemical, and mechanical stability, high breakdown electric fields, and high saturation drift rates, advantages over Si devices. The table 1.1 summarizes the properties of gallium nitride and silicon, as well as SiC, which is a wide-gap semiconductor like nitride semiconductors.

	E_G [eV]	ε	μ [cm²/Vs]	E_c [10^6 V/cm]	V_s [10^7 cm/s]	JFM $(E_cV_s/\pi)^2$	BFM $(\varepsilon\mu E_c{}^{3)}$
Si	1.1	11.8	1350	0.3	1.0	1	1
GaN	3.39	9.0	900 1300 (2DEG)	3.3	2.5	760	650
6H-SiC	3.0	9.7	370^a 50^c	2.4	2.0	260	110

Table 1.1 Properties of Si, GaN and SiC

E_G: Bandgap, ε: Relative permittivity, μ: Electron mobility, E_c: Breakdown field, V_s: Saturation velocity, JFM: Johnson's Figure of Merit, BFM: Baliga's Figure of Merit

The Baliga's Figure of Merit (BFM) is an indicator for the use of these semiconductor materials in power devices. This is the denominator in the equation relating on-resistance to breakdown voltage, and since GaN has a very high BFM when compared to Si and SiC, power devices using GaN will have very low on-resistance. There is also another index, the Johnson's Figure of Merit (JFM), which represents the relationship between power and cutoff frequency, and it shows that GaN is very attractive in high power high frequency devices. For example, trench-gate Metal-Oxide-Semiconductor (MOS) transistors, which are vertical transistors based on

GaN, can be highly integrated and driven at high power. In addition, high electron mobility transistors (HEMTs), which utilize high-density two-dimensional electron gas (2DEG) accumulated at the aluminum gallium nitride (AlGaN)/GaN hetero-interface, excel in high-power, high-frequency, and low ON-resistance operation due to their high breakdown voltage. It is hoped that the widespread use of these nitride semiconductor-based electronic devices will lead to significant advances in energy conservation and 5G applications. However, although nitride semiconductors have attractive electrical properties, their high chemical resistance poses a challenge to the processing technology used in device fabrication.

1.1.4. Concerns about device processing

Device processes for nitride semiconductors started in the 1990s, so they are still in the process of development compared to Si device processes, which were first studied in the 1950s. Examples of device processes include crystal growth, cleaning and drying, ion implantation and heat treatment, lithography, etching, and film deposition (oxide film and metal). Improvements in device performance have always progressed in tandem with process technology. For example, the maturation of the growth process has led to the introduction of freestanding GaN substrates, which have improved the positive performance of electronic devices. In recent years, as the ion implantation process has matured and the Mg activation rate has increased, the development of D-MOSFETs has begun, which were previously impossible to fabricate with GaN. The maturation of the etching process has led to the development of a variety of three-dimensional structures, which is helping to solve a variety of device issues. Thus, we can see that the maturity of process technology is very important for device breakthroughs.

Among the various processes, I am particularly interested in etching technology. The etching process is essential for device fabrication and plays a very important role in determining the performance of the device. Conventional semiconductor etching process can be roughly divided into two categories: wet etching and dry etching. Wet etching is an etching process using a chemical solution. It has been used for a long time as a semiconductor processing technology for Si and GaAs because of its low damage and ease of use. However, nitride semiconductors have very high chemical resistance, so it is difficult to process them by conventional wet etching.

Therefore, dry etching, a physical etching technique using plasma, has been used for nitride semiconductors in the past. However, there is one problem in the device process using dry etching. After dry etching, damage such as crystal defects and disordered bonding is introduced into the semiconductor surface, and it has been reported that such damage causes increased leakage current and threshold instability when devices are fabricated. Therefore, a new low-damage processing technology is now needed to replace dry etching.

1.2. Objective

In this paper, we focused on "photoelectrochemical (PEC) etching" as a new low-damage etching technique instead of dry etching, and investigated its application to nitride semiconductor electronic device fabrication processes. Specifically, for GaN and AlGaN nitride semiconductors, we clarified the photoelectrochemical characteristics of the electrolyte/nitride semiconductor interface, and developed an "anisotropic etching technique" for forming trench structures with high aspect ratios, a "recessed etching technique" for precisely controlling the threshold voltage of transistors, and an "etching technique" for improving the compatibility with existing contactless PEC etching process," which simplifies the electrochemical cell to improve its compatibility with existing semiconductor device processes. In particular, we found "etching self-stop phenomenon" in contactless PEC etching for AlGaN/GaN heterostructure, and achieved higher process controllability than conventional dry etching technology. The developed technique was applied to the fabrication process of recessed-gate AlGaN/GaN HEMTs, and its usefulness was discussed.

1.3. Outline of this thesis

This thesis consists of 7 chapters.

Chapter 1 described the background and purpose of this research. It discussed the need to improve the performance of power devices and the need for low-damage processing techniques for nitride semiconductors.

Chapter 2 describes the basic principles of electrochemistry that are important for understanding this thesis, especially the band structure and carrier transport at the semiconductor/electrolyte interface using semiconductor electrodes, and the phenomena necessary for understanding electrochemical processing technology up to the electrochemical reaction. In addition, examples of reported processing techniques for nitride semiconductors using electrochemical reactions are given.

Chapter 3 describes the experimental techniques involved in all chapters. It describes the general setup for electrochemical experiments, the basic principles of dry etching techniques used in device processing, and the principles of each device used for post-etching structural evaluation and optical and electrical characterization.

Chapter 4 shows the analyzed results of the electric field absorption effect observed at the electrolyte/GaN interface and developed an anisotropic PEC etching technique for GaN using this effect. By calculating the change in the optical absorption coefficient at each wavelength based on the potential barrier generated at the electrolyte/GaN interface and reproducing the experimental values of photocurrent values, we demonstrated that the Franz-Keldysh (F-K) effect occurs at the interface. We also applied the developed anisotropic PEC etching technique to initially processed low-donor-density GaN samples, and discussed the structural control and its usefulness for the formation of trench structures with high aspect ratio.

Chapter 5 shows the results that contactless PEC (CL-PEC) etching using acidic aqueous solution containing sulfuric acid radicals ($SO^{4\cdot-}$) was developed, and the results of applying it to the etching of GaN monolayer were presented. The results of the CL-PEC etching of GaN using acidic aqueous solutions containing $S_2O_8^{2-}/SO4^{\cdot-}$ are shown. It was clarified that the production rate of $SO4^{\cdot-}$, which is directly related to the etching rate, was demonstrated to be the same for both solutions by experiments and theoretical analysis, and the flatness of the etched surface was also confirmed to be the same. In addition, we demonstrated that the development of acid-based solutions can directly use positive photoresists as etching masks, which dramatically increases their suitability for existing device processes.

Chapter 6 shows the results that based on the results of Chapter 5, recessing of AlGaN/GaN heterostructures was performed using CL-PEC etching, and the surface conditions after etching and the electrical characteristics of various devices fabricated on the etched surface were evaluated. We found that the etching stopped in the middle of the upper layer of AlGaN (self-stop phenomenon) after recess processing by CL-PEC etching, and the remaining thickness of AlGaN at that time showed high uniformity within the sample surface. As a result of electrical characterization, Schottky-Barrier diodes, MIS-capacitors, Schottky-HEMTs and MIS-HEMTs fabricated on the recessed surface showed a decrease in leakage current compared to the devices fabricated on the non-recessed surface, and the threshold voltage increased in the positive direction as designed by the recess fabrication. The threshold voltage shifts positively as per the recess fabrication design. Furthermore, we found that the CL-PEC etching significantly improved the uniformity of device characteristics and discussed the factors behind this. From these results, it is shown that this etching method is promising as a nitride semiconductor device process.

The research will be concluded in **Chapter 7**.

Reference

[1] Cabinet Office, “Prospects for Expanding the Virtuous Circle”, White Paper on Japan’s Economy 2016-2017.

[2] Agency for Natural Resources and Energy, “White Paper on Energy 2021”.

[3] Ministry of Internal Affairs and Communications, “Information and Communication Statistics Database”.

[4] ITU-R, “IMT Vision-Framework and overall objectives of the future development of IMT for 2020 and beyond”.

[5] U. K. Mishra, P. Parikh, and Y. -F. Wu, "AlGaN/GaN HEMTs – an overview of device operation and applications", vol. 90, pp. 1022−1031, 2002.

[6] N. Ikeda, Y. Niiyama, H. Kambayashi, Y. Sato, T. Nomura, S. Kato, and S. Yoshida, "GaN Power Transistors on Si Substrates for Switching Applications", vol. 98, pp. 1151−1161, 2010.

Chapter 2

Semiconductor electrochemistry

2.1. Introduction

Since Luigi Galvani found "animal electricity" and Alessandro Volt indicated the relationship between electricity and chemistry in the late 18th century, "Electrochemistry" has been intensively researched among the various research area for a long time. Electrochemistry on semiconductor electrode is much useful because it is applicable to various kinds of functionalization technique of semiconductors. In **Chapter 2**, some essential aspects of semiconductor electrochemistry, especially related to practical etching of semiconductors, will be briefly described. Electrochemical fundamentals described in this chapter form the basis for the work in later chapters. In addition, typical examples which shows unique and practical features of electrochemical process on semiconductors were briefly presented.

2.2. Basic principles of electrochemistry [1]

2.2.1. Redox reactions

Electrochemical reactions are chemical reactions that involve electrically charged particles, electrons and ions. A substance that, when dissolved in water, splits into positively and negatively charged ions in various proportions without the application of an electric field is called an electrolyte, and a metal that is immersed in the electrolyte and undergoes an electrochemical reaction with the electrolyte by applying a voltage if necessary is called an electrode. Electrochemical reactions can be roughly divided into two types: reactions that receive electrons are called reduction reactions, and reactions that release electrons are called oxidation reactions. Electrodes that undergo reduction reactions are called cathodes, and electrodes that undergo oxidation reactions are called anodes.

$$\mathrm{Ox} \rightarrow Ox^{+} + e^{-}: \text{Oxidation Reaction}$$

$$\mathrm{Red} + e^{-} \rightarrow Red^{-} : \text{Reduction Reaction}$$

This reaction obeys the following Faraday's law of electrolysis.

$$\mathrm{m} = \frac{Q}{F}\left(\frac{M}{z}\right)$$

m: amount of material that has changed(g), Q: amount of electricity flowed(C),
M: molar mass of substance(g mol^{-1}),
F: Faraday constant(96485 C mol^{-1}),
z: number of electrons involved in the material change of a single molecule

Faraday's law states that the amount of material changed at each electrode by an electrochemical reaction is proportional to the amount of electricity flowing through it, and that the mass of material changed by the same amount of electricity is proportional to the molar mass of the material divided by the number of electrons involved. This means that by monitoring the amount of charge passing through, we can estimate the amount of reaction that has occurred on the electrode surface. This will be discussed in detail later.

2.2.2. Oxidation-reduction potential and the Nernst equation

Since electrons and ions have electric charges, their chemical potentials are affected by the electrostatic potentials of the electrode and solution layers in which they exist. The chemical and electrostatic potentials are collectively called the electrochemical potential. The electrochemical potential of electrons in the electrode phase is expressed by the following equation.

$$\tilde{\mu}_e{}^M = \mu_e{}^M - F\phi^M \ .$$

$\tilde{\mu}_e{}^M$: Electrochemical potential of electrons, $\mu_e{}^M$: Chemical potential of electrons,
ϕ^M: Internal potential of electrode phase

The internal potential is represented by the sum of the external potential of the electrode surface with respect to infinity in a vacuum and the surface potential that depends on the charge distribution on the surface. Ions in the solution phase are also charged bodies, as are electrons, so the potential can be expressed by the same equation.

$$\tilde{\mu}_i{}^M = \mu_i{}^\circ + RT\ ln\, a_i - z_i F \phi^L\ .$$

$\tilde{\mu}_i{}^M$: Electrochemical potential of ions, $\mu_i{}^\circ$: Chemical potential of the standard state of an ion,
a_i: Ion activity (equivalent to concentration in dilute solution), z_i: Charge number,
ϕ^L: Internal potential of solution phase

Using these equations, consider the electrode potential (redox potential) when the following electrochemical reactions are in equilibrium at the electrode surface.

$$O^{z+} + ne^- \longrightarrow R^{(z-n)+}\ .$$

Since the electrochemical reaction occurs at the interface between the electrode phase and the solution phase, we define the redox potential E as follows:

$$\mathrm{E} \equiv \phi^M - \phi^L\ .$$

The electrochemical potentials of oxidized O and reduced R are expressed as follows:

$$\tilde{\mu}_O{}^M = \mu_O{}^\circ + RT\ln\ a_O - zF\phi^L\ ,$$
$$\tilde{\mu}_R{}^M = \mu_R{}^\circ + RT\ln\ a_R - (z-n)F\phi^L,$$

respectively. At equilibrium, the electrochemical potentials of each are equal, so

$$\tilde{\mu}_O{}^M + n\,\tilde{\mu}_i{}^M = \tilde{\mu}_R{}^M\ .$$

Using these equations, the electrode potential E can be expressed as:

$$\mathrm{E} \equiv \phi^M - \phi^L = -\frac{(\mu_R{}^\circ - \mu_O{}^\circ - n\,\mu_e{}^M)}{nF} + \frac{RT}{nF}\ln\frac{a_O}{a_R}\ .$$

The expression in parentheses in the first term on the right-hand side of this equation corresponds to the standard Gibbs energy ΔG^∘ for this electrochemical reaction, so

$$E^{\circ} = -\frac{(\mu_R{}^{\circ} - \mu_O{}^{\circ} - n\,\mu_e{}^{M})}{nF} = -\frac{\Delta G^{\circ}}{nF}.$$

and rewriting, the electrode potential E becomes

$$\mathrm{E} = E^{\circ} + \frac{RT}{nF}\ln\frac{a_O}{a_R},$$

where E° is called the standard redox potential, or standard potential. This equation is called the Nernst equation, and it is a very important equation for the redox potential.

When the metal electrode is immersed in the electrolyte, if the Fermi level is more positive than the redox potential, the transfer of electrons from the electrode to the redox species takes place and a reduction reaction occurs. This transfer takes place until the redox potential equals the Fermi level of the electrode.

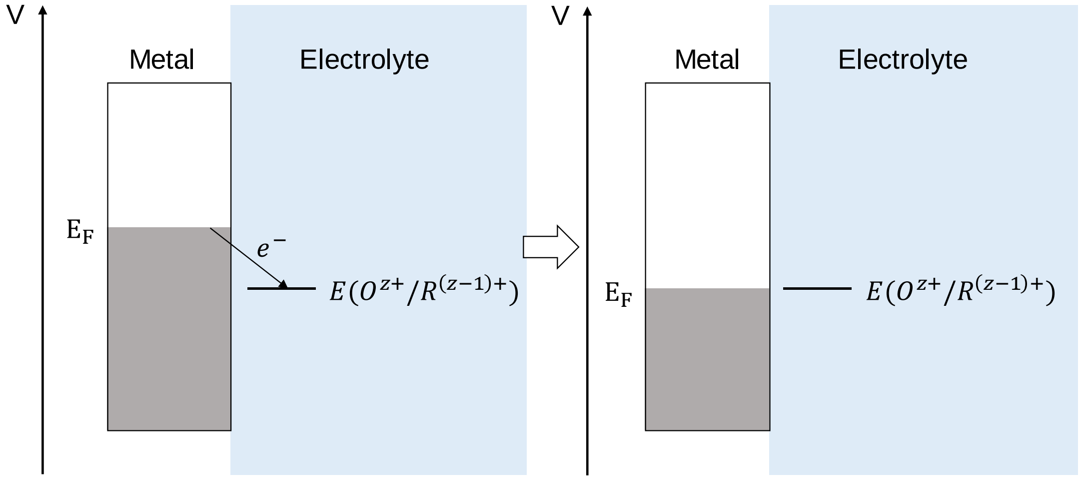

Fig.2.1 Electron transfer when a metal electrode is immersed in an electrolytic solution

After equilibrium is reached, if the electrodes are wired and a charge is supplied (voltage applied) from an external power source, the Fermi level will increase, and the transfer of electrons from the metal to the redox species will take place again.

2.2.3. Rate-limiting process of electrode reactions

The electrode reaction mainly involves the transfer of charge at the electrode/solution interface, which is called the charge transfer process. After the charge transfer process is completed, the equilibrium state of the concentration of the substances involved in the reaction is broken in the solution near the electrode surface due to the reaction, and mass transfer occurs. This is called the mass transfer process. After the mass transfer process is completed, charge transfer corresponding to the electric current is carried out in the solution phase by the potential swimming of electrolyte ions. This is called the ion-electric conduction process. In electrochemical reactions, the reaction rate is limited (rate-limiting) by the slowest of these three processes, but in actual reaction systems, the reaction is effectively rate-limiting by either the charge-transfer process or the mass-transfer process, since an excess of indicator electrolyte, which is not involved in the reaction, is added to prevent the ion-electrical conduction process from becoming rate-limiting. In effect, the reaction is rate-limiting. Here, we will discuss the charge transfer process in some detail.

Initially, the following electrode reactions are considered to occur in the charge transfer process.

$$\mathrm{O} + \mathrm{n}e^- \underset{V(k)}{\longleftrightarrow} R\ .$$

v: Reaction rate per unit surface area of electrode(mol s^{-1} cm^{-2}),
k: Velocity constant (cm s^{-1})

The reaction rate and rate constant on the oxidation side are v_o and k_O, respectively, and those on the reduction side are v_R and k_R, respectively. The concentrations of the oxidant O and the reductant R at the electrode surface (at the distance x=0 from the electrode surface and at time t) are $c_o(0,t)$, $c_R(0,t)$ (mol cm^{-3}), and each reaction rate can be expressed as follows:

$$v_O = k_o c_o(0,t), \qquad v_R = k_R c_R(0,t).$$

From Faraday's law, there is a relationship between the amount of electricity Q(C) and the number of moles of O or R produced (consumed) by the reaction N(mol), where Q = -nFN, so the Faraday current I(A) flowing from each reaction is expressed as follows:

$$\text{Faraday Oxide Current: } I_O \equiv \frac{dQ}{dt} = -nF\frac{dN}{dt} = -nFAv_O\ ,$$

$$\text{Reduced Faraday current: } I_R \equiv \frac{dQ}{dt} = nF\frac{dN}{dt} = nFAv_R\ .$$

From this equation, we can see that the current flowing during an electrochemical reaction represents the rate of the redox reaction. The current flowing through the electrode is actually expressed as the sum of the oxidation current and the reduction current, so the current i (A/cm^2) per unit area that can be observed in the external circuit is

$$\mathrm{i} = -\mathrm{nF}(v_O - v_R).$$

2.3. Electrochemistry at semiconductor electrode

2.3.1. Potential distribution of semiconductor/electrolyte interface

So far, we have discussed the case where a metal is used as an electrode, which is common in electrochemical systems, but we will now discuss the case where a semiconductor is used as an electrode. The electrochemical potential of electrons in a semiconductor is also generally expressed in terms of Fermi levels. When a semiconductor is brought into contact with an electrolytic solution, it behaves in the same way as when a semiconductor is brought into contact with a metal. In other words, if the redox potential of the redox species in the electrolyte is more positive than the Fermi level of the semiconductor, electrons are transferred from the semiconductor to the redox species, and the Fermi level decreases, reaching an equilibrium state when the redox potential and Fermi level match. At this time, a space charge layer is created on the semiconductor side. When an n-type semiconductor with an ohmic junction on the back side is used as an electrode, a barrier is considered to exist at the semiconductor/electrolyte interface, similar to a Schottky junction with a metal.

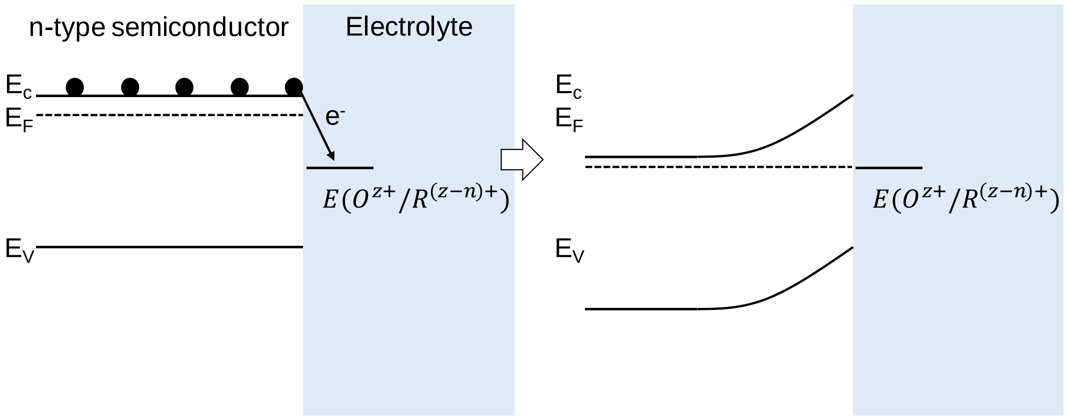

Fig.2.2 Transition from contact between semiconductor and electrolyte to equilibrium state

2.3.2. Redox reactions under polarization

When a positive voltage is applied to the semiconductor electrode, no oxidation reaction occurs. When a negative voltage is applied, a reduction reaction occurs when the electrode potential becomes more negative than the flat band potential, which is the potential equivalent to the bend of the band. In other words, a current-potential curve showing rectification characteristics is obtained.

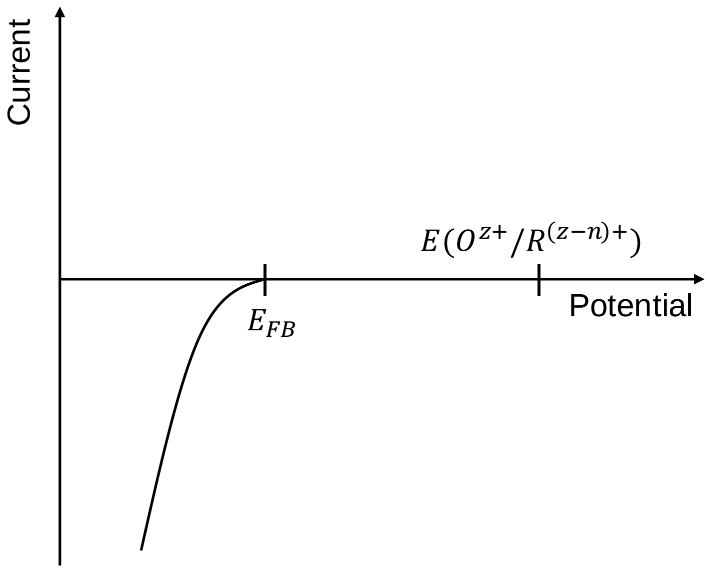

Fig. 2.3 Current-potential curve of a semiconductor in electrolytic solution

As for the oxide and Ga compound semiconductors, they are in equilibrium in solution as shown in the following equation.

$$\mathrm{M-OH} \rightleftharpoons M - O^{-} + H^{+}$$

Therefore, when the pH of the electrolyte increases (hydrogen ion concentration decreases), the reaction tilts to the right and the surface becomes negatively charged, so the energy level of the semiconductor electrode becomes relatively high with respect to the electrolyte. The ratio of potential increase to pH at this time is expressed as -59 mV/pH.

2.3.3. Redox reactions under illumination

When a semiconductor electrode is irradiated with light having an energy greater than the forbidden band width of the semiconductor, electrons are excited from the valence band to the conduction band at the semiconductor surface, and holes are generated in the valence band. The electrons move to the bulk side along the potential slope of the space charge layer, while the holes accumulate on the surface. At this time, if the redox potential of the redox species present in the solution is higher than the energy level of the valence band, holes will take away electrons from the redox species, i.e., photo-oxidation reaction of the redox species will occur. The photo-oxidation reaction carried out by this process occurs when the electrode potential is more positive than the flat band potential. On the contrary, if it is more negative than the flat band, the electrons will follow the slope of the potential to the interface, and thus the reduction reaction of redox species will occur.

There are two characteristics of the current-potential curve during light irradiation. The first is that the photo-oxidation reaction takes place on the positive side of the flat-band potential, but the potential is more negative than the redox potential when using a normal metal electrode. In other words, the redox potential is apparently shifted by light irradiation, which indicates that an electrochemical reaction is taking place with the help of light energy. This phenomenon is called photosensitized electrolytic oxidation. Similarly, a p-type semiconductor electrode can perform photosensitized electroreduction, in which the reduction reaction proceeds at a potential more positive than the redox potential of the redox species.

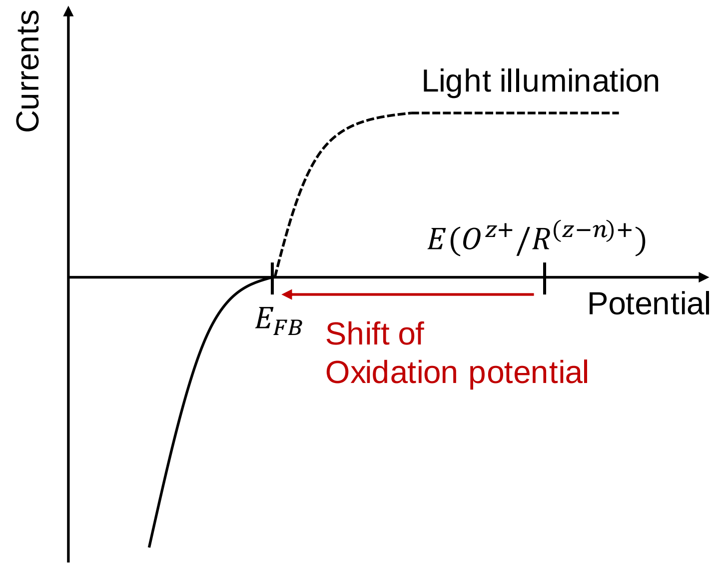

Fig. 2.4 Current-potential curve of a semiconductor under light irradiation

The second feature is that when the potential is shifted from the flat band to the positive side to some extent, a saturation current appears. This appears even when the concentration of redox species is sufficiently high. The reason for this is that the oxidation reaction proceeds by means of holes generated by light irradiation, and the number of holes generated per unit time by light irradiation depends on the intensity of the irradiated light. In other words, the reaction rate of the oxidation reaction is governed by the number of holes generated by the absorption of light per unit time. In other words, this saturation current value is proportional to the light intensity. If the current does not reach the saturation current, the same number of holes will be generated, but the holes that are not used for the reaction will be deactivated by recombining with excited electrons. At this time, there is a concept of quantum efficiency Φ as a parameter that indicates the proportion of electrons and holes that can be used electrochemically, and it is defined as follows:

$$\phi(\%) = \frac{\text{Number of electrons in photocurrent}}{\text{Number of photons in incident light}} \times 100$$

2.4. Electrochemistry at semiconductor electrode

2.4.1. Anodic dissolution of nitride semiconductors

Most semiconductors are susceptible to anodic reactions by holes, because the semiconductor electrodes themselves are anodically dissolved in the electrolyte. The presence of a hole (h+) in the local bonding at the surface means that one electron in the bonding orbital has been removed. In the case of gallium arsenide (GaAs), Gerischer and Mindt 8) proposed that the trapping of a hole at this semiconductor surface can be represented by the reaction of a nucleophile (X-) with one of the positively charged surface atoms, resulting in the removal of an electron. The remaining unpaired electron is no longer in the Valence Band (VB) state, but has an energy level with a band gap close to VB, similar to an acceptor state. It has been found that four more holes are needed to completely dissolve one GaAs. This is a qualitative explanation of the anodic dissolution of semiconductors. From the above discussion, it is clear that holes are required on the electrode surface for the anodic dissolution of semiconductors. p-type semiconductors have a large number of holes as carriers in VB, so anodic dissolution can occur by applying a potential ($>E_{FB}$) to the electrode. On the other hand, for n-type semiconductors, anodic dissolution in the dark is difficult because there are few holes in VB to begin with. n-type semiconductors have no holes in VB, so light irradiation is the main method to cause anodic dissolution.

As described in section 2.3.3, semiconductor electrodes can absorb photon energy and generate excited electrons and holes in the Conduction Band (CB) and VB by light irradiation, causing anodic dissolution. Anodic dissolution under light irradiation is called "photo-assisted electrochemical etching". In this method, the anodic reaction can be caused by transferring holes from VB of the semiconductor electrode to the electrolyte: (1) the irradiated light (photon) has an energy greater than the band gap, and (2) the applied potential is greater than the flat band potential. These features allow photo-assisted electrochemical etching to achieve excellent etching selectivity in terms of band gap 9), dopant type 10), etc. 11).

Fig. 2.5 shows a typical example of material-selective photo-assisted electrochemical etching reported by A. R. Stonas and co-workers 9).

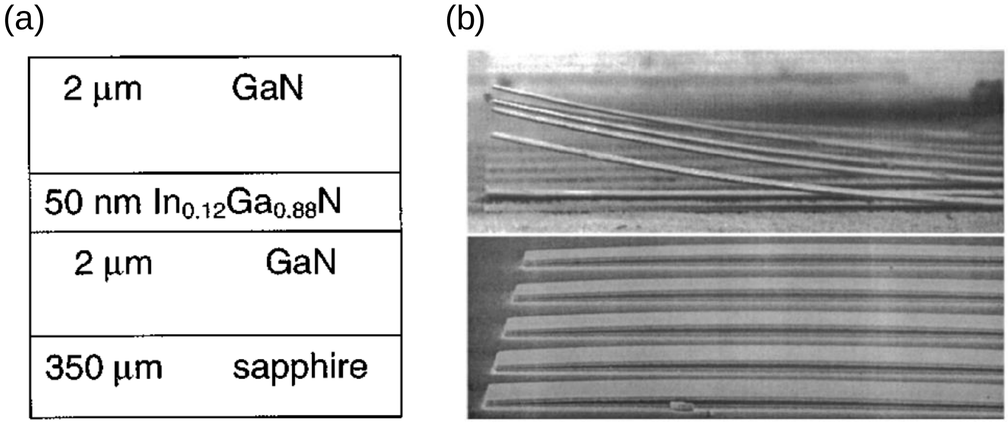

Fig.2.5 (a) Schematic illustration of sample structure and (b) SEM image of sample after material-selective etching by photo-assisted electrochemical process [9]: GaN cantilevers curved upwards by the removal of InGaN layer and the relief of substrate-induced strain.

The $In_{0.12}Ga_{0.88}N$ (low bandgap energy relative to GaN) layer on GaN can be selectively removed using a GaN filter to limit the wavelength of illumination. After the selective removal of InGaN, the GaN cantilever curved upward due to the relaxation of the inherent strain gradient in the as-grown material.

Dopant-selective photo-assisted electrochemical etching has also been actively studied. n-type semiconductors have a lower flat-band potential than p-type semiconductors, and thus n-type semiconductors can be selectively anodically etched

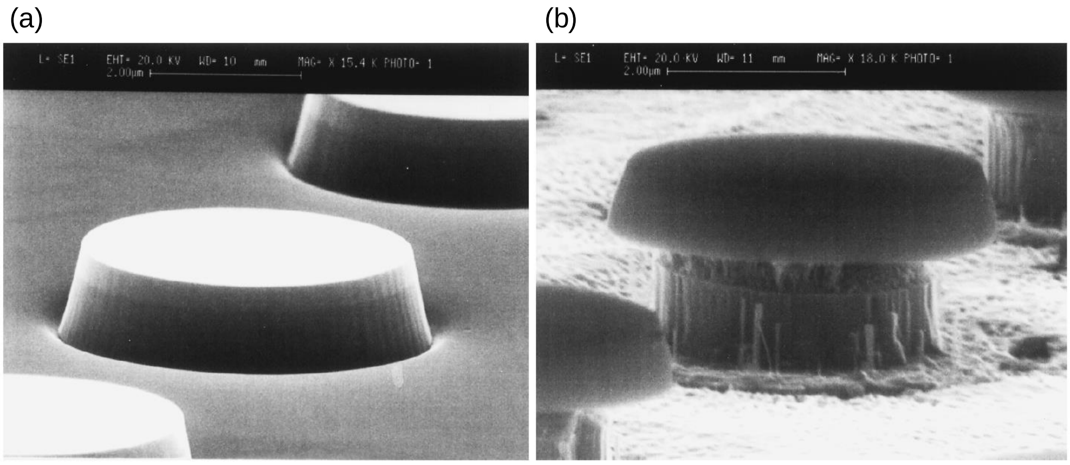

Fig. 2.6 SEM images of p-on-n GaN columns (a) before and (b) after dopant-selective etching by photo-assisted electrochemical process [10].

rather than p-type semiconductors. Fig. 2.6 shows a typical example of dopant-selective photo-assisted electrochemical etching reported by C. Youtsey et al [10]. The lower layer of n-type GaN is selectively etched, while the upper layer of p-type GaN remains unchanged, resulting in a mushroom-shaped structure.

Another well-known practical application of photoassisted electrochemical etching is defect-selective etching; C. Youtsey et al. reported on whisker-like structures formed by photoassisted electrochemical etching [11]. TEM observations revealed that the whiskers correspond to edge dislocations and mixed dislocations, as shown in Figure 2.7. Dislocation-like defects act as recombination centers that prevent holes from contributing to the anodic reaction.

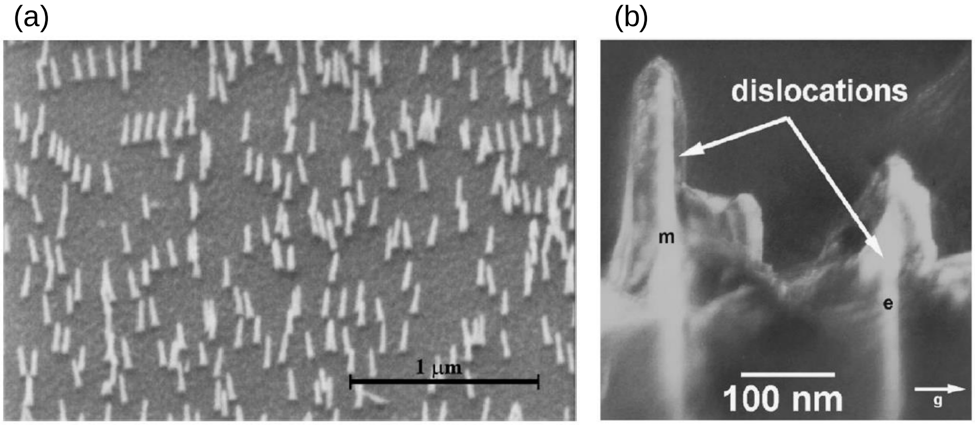

Fig.2.7 (a) The SEM image of GaN whisker-shaped structure, and (b) the cross-sectional TEM image of whisker, showing that both edge (e) and mixed (m) dislocations are associated with whisker formation [11].

2.4.2. Potential distribution of semiconductor/electrolyte interface

In the second half of the 20th century, the discovery of luminescent porous Si formed by electrochemical processes triggered a great deal of interest in porous semiconductors. At the same time, porous structures were formed in various III-V semiconductors, and their unique properties were emphasized.

In n-type III-V semiconductors, the formation of porous structures due to anodic dissolution in the dark has been well reported; as discussed in Sections 2.3.2 and 2.4.1, the amount of anodic current due to holes is generally small in n-type semiconductors because holes are minority carriers. However, when the electrode is strongly polarized in the anodic direction, a steep increase in the anodic current is usually observed. This increase in the anode current is thought to be related to the holes generated by the avalanche effect caused by the m-depletion layer electric field. Under high electric field, avalanche breakdown may be initiated by a small number of electrons tunneling from VB or RED to CB. When the field strength of the depletion layer electric field reaches a critical value, the tunneling electrons are accelerated enough to defeat the other bound electrons, leading to the generation of new electron-hole pairs. Avalanche breakdown is thought to be preferentially initiated at dislocations, point defects, and scratches, so local anodic dissolution can occur. This local dissolution leads to the formation of new pits, and local anodic dissolution due to avalanche breakdown may occur at low potentials as in the previous process. Repetition of these cycles allows for pore growth in n-type semiconductors. p-type III-V semiconductors often undergo uniform dissolution, called electropolishing, because of the uniform distribution of holes in VB.

Porous structures of III-V semiconductors exhibit the following new and attractive properties compared to bulk materials.

A) In a porous semiconductor with an indirect band gap, the band-edge luminescence is dramatically enhanced in photoluminescence (PL) properties 12).
B) Blue shift of emission near the band edge of PL due to quantum confinement effect 13,14).
C) Dramatic increase in optical second harmonic generation (SHG) from porous GaP films 15).
D) Jet-black surface appearance due to extremely low reflectance in the visible region 16).
E) Refractive index change due to porosity 17).
F) Reduction of substrate-induced strain, which is typically observed in GaN grown on foreign substrates 18,19).

Reference

[1] N. Sato, "Electrochemistry at Metal and Semiconductor Electrode", Elsevier Science, Amsterdam, 1998.

[2] R. A. Marcus, "On the Theory of Oxidation-Reduction Reactions Involving Electron Transfer. I", J. Chem. Phys., vol. 24, pp. 966−978, 1956.

[3] P. Delehay, and C. W. Tobias, "Advance in Electrochemistry and Electrochemical Engineering, volume 1: Electrochemistry", Interscience Publishers, New York, 1961.

[4] W. Schokley, "Electrons and Holes in Semiconductors", Van Nostrand, Newyork, 1950.

[5] H. Gerischer, "The impact of semiconductors on the concepts of electrochemistry", Electrochim. Acta, vol. 35, pp. 1677−1699, 1990.

[6] M. A. Butler, "Photoelectrolysis and physical properties of the semiconducting electrode WO_2", J. Appl. Phys., vol. 48, pp. 1914−1920, 1977.

[7] R. Memming, "Charge transfer kinetics at semiconductor electrodes", Ber. Bunsenges. Phys. Chem., vol. 91, pp. 353−361, 1987.

[8] H. Gerischer, W. Mindt, "The mechanisms of the decomposition of semiconductors by electrochemical oxidation and reduction", Electrochim. Acta, vol. 13, pp. 1328−1341, 1968.

[9] A. R. Stonas, N. C. MacDonald, K. L. Turner, S. P. DenBaars, and E. L. Hu, "Photoelectrochemical undercut etching for fabrication of GaN microelectromechanical systems", J. Vac. Sci. Technol. B, vol. 19, pp. 2838−2841, 2001.

[10] C. Youtsey, G. Bulman, and I. Adesida, "Dopant-selective photoenhanced wet etching of GaN", J. Electron. Mater., vol. 27, pp. 282−287, 1998.

[11] C. Youtsey, L. T. Romano, and I. Adesida, "Gallium nitride whiskers formed by selective photoenhanced wet etching of dislocations", Appl. Phys. Lett., vol. 73, pp. 797−799, 1998.

[12] K. Kuriyama, K. Ushiyama, K. Ohbora, Y. Miyamoto, and S. Takeda, "Characterization of porous GaP by photoacoustic spectroscopy: The relation between band-gap widening and visible photoluminescence", Phys. Rev. B, vol. 58, pp. 1103−1105, 1998.

[13] L. T. Canham, "Silicon quantum wire array fabrication by electrochemical and chemical dissolution of wafers", Appl. Phys. Lett., vol. 57, pp. 1046−1048, 1990.

[14] T. Fujino, T. Sato, and T. Hashizume, "Size-Controlled Porous Nanostructures Formed on InP(001) Substrates by Two-Step Electrochemical Process", Jpn. J. Appl. Phys., vol. 46, pp. 4375−4380, 2007.

[15] I. M. Tiginyanu, I. V. Kravetsky, G. Marowsky, and H. L. Hartnagel, "Efficient Optical Second Harmonic Generation in Porous Membranes of GaP", Phys. Status. Solidi A, vol. 175, pp. R5−R6, 1999.

[16] T. Sato, N. Yoshizawa, and T. Hashizume, "Realization of an extremely low reflectance surface based on InP porous nanostructures for application to photoelectrochemical solar cells", Thin Solid Films, vol. 518, pp. 4399-4402, 2010.

[17] E. Kikuno, M. Amiotti, T. Takizawa, and S. Arai, "Anisotropic Refractive Index of Porous InP Fabricated by Anodization of (111)A Surface", Jpn. J. Appl. Phys., vol. 34, pp. 177−178, 1995.

[18] A. P. Vajpeyi, S. J. Chua, S. Tripathy, and E. A. Fitzgerald, "Effect of carrier density on the surface morphology and optical properties of nanoporous GaN prepared by UV assisted electrochemical etching", Appl. Phys. Lett., vol. 91, p. 083110, 2007.

[19] K. Al-Heuseen, M. R. Hashim, and N. K. Ali, "Growth and Characterization of Tree-Like Crystalline Structures during Electrochemical Formation of Porous GaN", J. Electrochem. Soc., vol. 158, pp. D240−D243, 2011.

Chapter 3

Experimental technique

3.1. Introduction

Chapter 3 gives a brief overview of experimental techniques for formation and characterization of nitride semiconductor microstructures. EC cell in which redox reactions take place, and a potentiostat which is needed to control electrode potential precisely, are first described, followed by EC characterization techniques in Section 3.2; Inductive Coupled Plasma-Reactive Ion Etching" was a dry etching technique commonly used in nitride semiconductor fabrication processes in Section 3.3; nitride semiconductors after EC process are characterized by various techniques: the structural characteristics were evaluated by scanning electron microscopy (SEM) and atomic force microscopy (AFM) described in Section 3.4; the optical characteristics were evaluated by ultraviolet-visible-infrared (UV-VIS-IR) spectroscopy, photoluminescence (PL) spectroscopy described in Section 3.5; and the electrical characteristics were evaluated by current-voltage (*I*-*V*) measurements, and capacitance-voltage (*C*-*V*) measurements described in Section 3.6.

3.2. Electrochemical process and characterization

3.2.1. Three-electrode electrochemical cell and potentiostat

In this chapter, I will explain for the electrochemical-experimental system in detail. The electrochemical methods are roughly classified as follows: (1) potentiostatic electrolysis and (2) galvanostatic electrolysis. The potentiostatic electrolysis method is to apply the electrode potential to the electrode as a function of time by the external circuit and measure the current through the electrode. A potentiostat, described below, is used to control the electrode potential. The galvanostatic electrolysis method is to control the current as a function of time by an external circuit and observe the change in electrode potential, with a device called a galvanostat. This experiment was conducted by the potentiostatic electrolysis method.

A three-electrode system is conventionally used for electrochemical experiments. Fig.1 shows that a commonly used system.

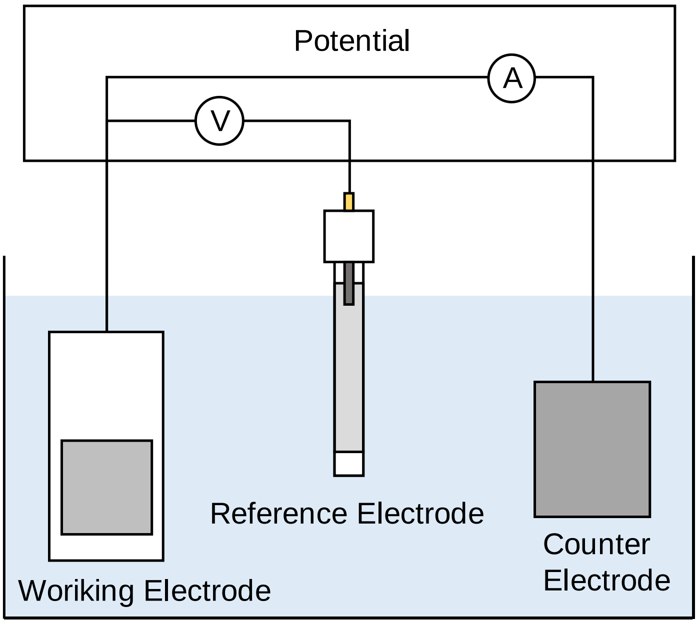

Fig.3.1. General three-electrode cell

The three types of electrodes (a working electrode, a reference electrode, and a counter electrode) are immersed in the electrolyte and wired with a potentiostat or galvanostat. The reason for using this three-electrode system is that oxidation and reduction reactions always occur in pairs in the electrochemical system. In order to observe them separately, one sets the conditions so that the reaction wanted to be seen occurs at the working electrode and the opposite reaction occurs at the counter electrode. Therefore, the current by the reaction flows between the working and the counter electrode. The reference electrode is utilized to control and measure the potential of the working electrode, and no current flows between the working and reference. When there are the sufficient supporting electrolyte in the electrolyte, the electrolyte resistance is small, however, when the electrolyte resistance is large, such as in a nonaqueous solvent system, the placement of the reference electrode should be considered. The electrode potential controled or measured by a potentiostat or galvanostat is the potential difference between the working electrode and the reference electrode, and when the current flows between the working electrode and the counter electrode, the potential difference decreases due to the ohm effect caused by the electrolyte resistance between the working electrode and the counter electrode. In order to suppress the ohm effect, the following method is used. In order to suppress this Ohm effect, it is better to place the reference electrode as close as possible to the working electrode. Next, we will describe in detail the working electrode, reference electrode, and potentiostat, which are particularly important in a three-electrode system.

A) working electrode

In the electrochemical reactions, the reaction of the substance to be observed is occurred at the working electrode and observed. The solvent of the substance and the material of the working electrode should be chosen so that they do not react with each other over a wide range of potentials. The potential range in which the solvent and electrode do not react is called the potential window of the electrode material. In the past, the dropping mercury electrode was most commonly used as working electrodes. The dropped mercury electrodes did not require pretreatment of the electrode surface because the electrode surface was constantly renewed, and measurement with good reproducibility was possible. However, the redox potential of mercury, $Hg^{2+} + 2e^- \rightarrow Hg$, is not very high, and if the ions that form with mercury ions, such as chlorine ions or hydroxide ions, are present in the solution, they are oxidized at a very low potential, resulting in a small potential window. The method was gradually discontinued due to the above problems.

Currently, platinum and gold electrodes are commonly used as working electrodes because they can be easily obtained in high purity and are easy to process. Platinum electrodes have a small potential window on the negative side because the overpotential required for hydrogen generation is much smaller than that of mercury electrodes, but on the contrary, the polarization region on the positive side extends to nearly +1.5 V vs SHE. The hydrogenation voltage of the gold electrode is larger than that of the platinum electrode but smaller than that of the mercury electrode. In these noble metal electrodes, the current due to the oxide film formation and its reduction current always flow in the positive side, but these currents and the hydrogen adsorption/desorption current are due to the surface reaction and only a certain amount of electricity flows. Therefore, it is possible to investigate other electrode reactions even in the potential region where these currents flow. In order to obtain reproducible results using solid electrodes, pretreatment of the electrode surface is important. It is common practice to polish the electrode surface with a suitable abrasive and then clean it with an ultrasonic cleaner.

B) Reference Electrode

The reference electrode is, as mentioned above, an electrode used to control or measure the potential of the working electrode. The reference electrode consists of a metal electrode part (silver, mercury, platinum, etc.), an internal electrolyte, a liquid contact part (ceramic, bicol, etc.) and a container that holds these three parts together. Most of the containers are made of a cylindrical glass with a liquid contact at the end. The liquid contact is made of a porous material, such as a bicol glass or a ceramic, to provide an electrical contact with the electrolyte. In addition, Teflon may be used as a container for its chemical resistance. The equilibrium potential of the electrode reaction is described by the Standard Hydrogen Electrode (SHE), which is the most basic reference electrode. However, because SHE is difficult to handle in actual use, a calomel electrode using mercury and silver-silver chloride electrodes using silver electrodes are often utilized due to the better reproducibility of the potential and easiness to handle.

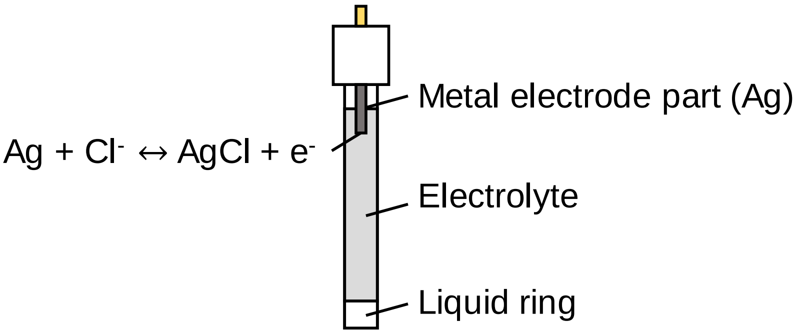

Fig.3.2. Schematic graph of silver-silver chloride electrode

At the electrode part of the reference electrode, reversible redox reactions, which are different for each electrode, occur in the equilibrium. The redox potential indicated by the reaction is the reference potential of the reference electrode. Naturally, because the equilibrium potential is different depending on the reactions, when a reference electrode other than SHE is utilized, it is necessary to consider to the difference of the potential. For an electrode where such equilibrium reactions are occurring, the electrode potential is kept constant because the potential cannot be manipulated externally with the quickly consumption of the reactions even if charge is given. The electrode is called a non-polarizable electrode. However, if a large amount of charge is given, the electrode potential may change due to the concentration changes caused by the reactions, and the reference electrode is controlled by a potentiostat so that no current flows through it. The following table shows the reactions occurred in the reference electrode and the potential difference SHE and the reference electrodes commonly used.

The name	The equilibrium reaciotns	The potential difference from SHE
SHE	$H_2 \Leftrightarrow 2H^+ + 2e^-$	-
Calomel electrode	$Hg + Cl^- \Leftrightarrow \frac{1}{2} Hg_2Cl_2 + e^-$	0.334 V (0.1 M KCl) 0.281 V (1.0 M KCl) 0.241 V (saturated KCl)
Silver-silver chloride electrode	$Ag + Cl^- \Leftrightarrow AgCl + e^-$	0.289 V (0.1 M KCl) 0.236 V (1.0 M KCl) 0.197 V (saturated KCl)

Table 3.1 Portential difference between each reference electrodes and SHE

As shown above, the electrode potential changes depending on the concentration of the electrolyte used even in the same electrode system.

C) Potentiostat

A potentiostat and a galvanostat used in the electrochemical measurements are fabricated by an integrated circuit called an operational amplifier. A simple basic principle of a potentiostat is shown below.

Considering the use in a three-electrode system, the potentiostat controls the potential of the working electrode with respect to the potential of the reference electrode, and outputs the current flowing between the working and counter electrodes as a voltage signal to an external circuit. First of all, if the external voltage is V_{ex}, the potential of the reference electrode is E_{RE}, and the potential of the working electrode is E_{WE}, it is required to control the difference between the external voltage and the potentials of the reference and working electrodes to be equal.

$$V_{ex} = E_{WE} - E_{RE}$$

If we assume that the working electrode is grounded, $E_{WE} = 0$, and $V_{ex} = -E_{RE}$, the circuit that satisfies this can be simply represented as shown in the following figure using a single operational amplifier.

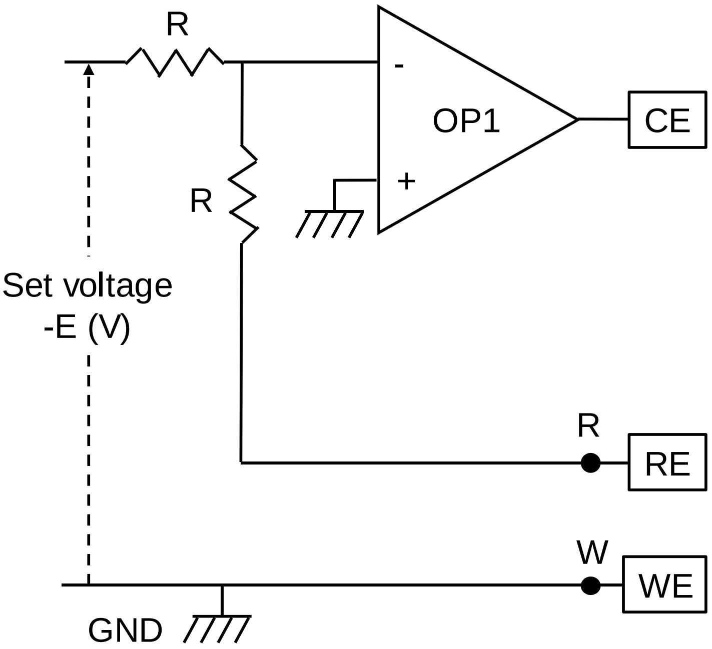

Fig.3.3. The most basic potentiostat circuit diagram

Since OP1 is in a virtual ground state as shown in Fig.3, all three terminals can be considered to be at the same potential as GND. From there, considering that both the WE circuit and the RE circuit have the same voltage drop across the same resistor, we can see that the potential at points R and W will be the same. The role of OP1 is to maintain the potential difference between the external voltage and RE and WE at the same level, and to do so, it outputs the necessary voltage and passes the current. Such an operational amplifier is called a current amplifier or control amplifier.

However, in order for the three-electrode system to function properly in actual measurement, it is a necessary condition that no current flows to the reference electrode. For this purpose, a voltage follower is used between OP1 and point R.

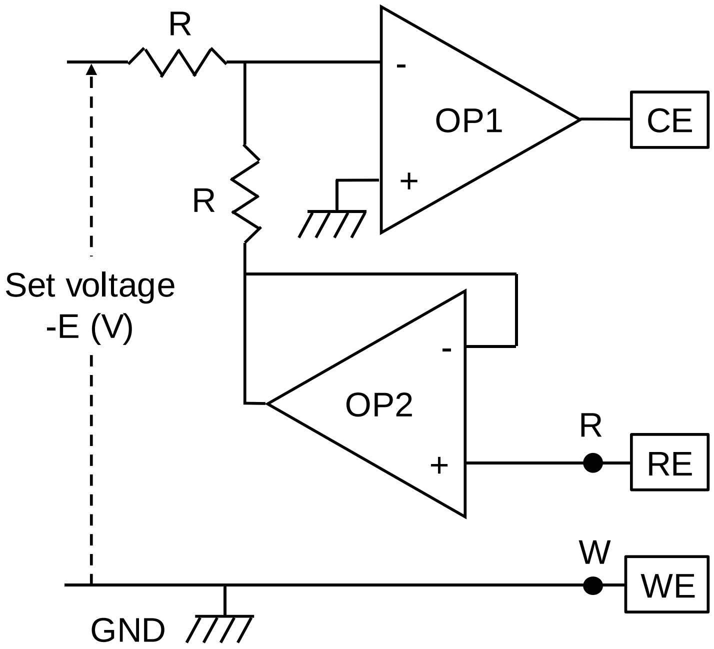

Fig.3.4 Circuit incorporating a voltage follower for potential stabilization

A voltage follower is a device that outputs the input voltage as it is, and is used when a very high input impedance is required to stabilize the voltage of interest, such as when measuring the electromotive force of a battery. By incorporating this element, it becomes possible to maintain the potential of RE stably without passing current through it.

Finally, we will consider measuring the current flowing between WE and CE. It is desirable to convert the current value into a voltage signal VI in order to output the current value to an X-Y recorder or to import it into a computer using an analog to digital conversion board. Therefore, an I-V conversion circuit using an operational amplifier is used.

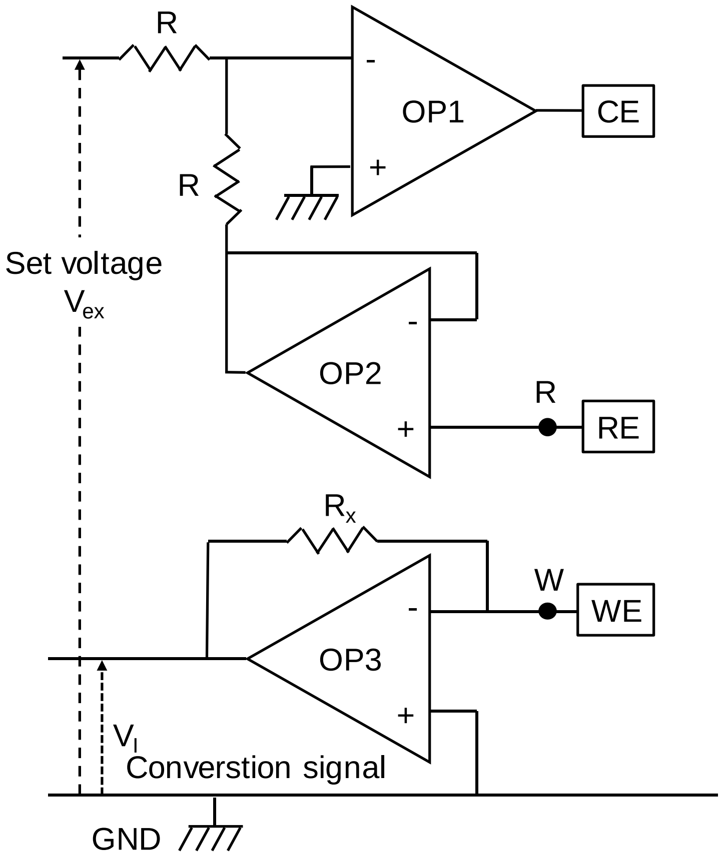

Fig.3.5 Circuit incorporating a voltage follower for potential stabilization

Again, since WE is virtual grounded, the potential difference between the external voltage and RE and WE is the same. Since the current flow is positive from WE to CE, the potentiostat outputs VI = IWERx.

As described above, the potentiostat is in principle composed of three operational amplifiers. In actual use, various mechanisms are incorporated to protect the operational amplifiers and stabilize the operation.

3.2.2. *Linear sweep and cyclic voltammetry*

In this chapter, cyclic voltammetry (also called CV potential scanning) is described, which is the most basic method of electrochemical measurement. This method records the transition of the current when the electrode potential is applied from the initial potential to a set reversal potential, then applied again to the reversal potential on the reverse bias side, and then returned to the initial potential. The current-potential curve obtained in this process is called a cyclic voltammogram. In the plot, a negative current indicates that the reduction reaction is preferentially carried out, while a positive current indicates that the oxidation reaction is preferentially carried out. This method is relatively easy to experiment with and sensitively reflects not only equilibrium parameters such as redox potential and diffusion information, but also kinetic parameters such as electrode reactions and chemical reactions in solution. Therefore, it has the advantage that electrode reactions can be grasped intuitively, and it is very useful as an initial diagnostic method, and is widely used in a wide range of fields such as inorganic, organic, polymer, and biochemistry. In addition, with the development of computers, the digital simulation analysis of cyclic voltammograms has recently made it possible to easily evaluate various parameters.

3.2.3. *Mott-Schottky plot*

As mentioned above, when a semiconductor is in contact with an electrolyte, the interface is like a Schottky junction in the equilibrium state. Therefore, by performing a Mott-Schottky plot, it is possible to determine the built-in potential, carrier density near the surface, and so on. The following is the derivation of the Mott-Schottky plot.

The band diagram near the interface in the equilibrium state is shown below.

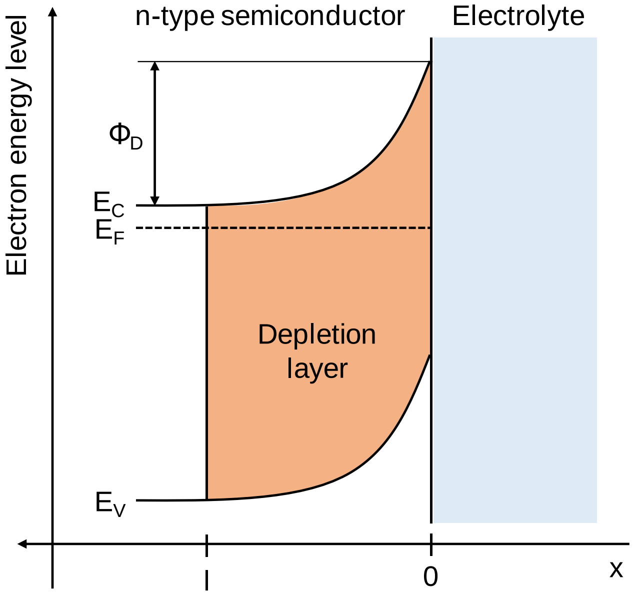

Fig.3.6 Schematic figure of the semiconductor/electrolyte interface at equilibrium

Here, the built-in potential is ϕ_D (eV), the interface is 0, the x-axis is in the bulk direction, and the depletion layer width is l(m). Assuming that all donor atoms are ionized in the depletion layer by the depletion approximation, the charge density per unit area in the depletion layer, Q(cm-2), is shown as:

$$Q = -qN_D l ,$$

where q(C) is the charge element and N_D is the donor density.

Also, if we set the Poisson equation in the x-axis direction in the depletion layer,

$$\frac{d^2\phi_{(x)}}{dx^2} = -\frac{\rho(x)}{\varepsilon} = \frac{qN_D}{\varepsilon} ,$$

wherewhere $\rho_{(x)}$ (cm^{-3}) is the charge density per unit volume, $\varphi_{(x)}$ is the potential in the x-axis direction, and ε is the dielectric constant of the semiconductor.

Integrating the above equation, we get

$$\frac{d\phi_{(x)}}{dx} = E\,(x) = \frac{qN_D}{\varepsilon}(x - l),$$

where E(x) is the electric field in the x-axis direction.

For this derivation, we used the fact that E(l) = 0. Furthermore, integrating the above equation for the electric field, we obtain

$$\phi_{(x)} = \frac{qN_D}{2\varepsilon}(\mathrm{x}-\mathrm{l})^2 + \mathrm{D}\,,$$

where D is an integration constant.
Since $\phi_{(0)} - \phi_{(l)}$ is equal to ϕ_D,

$$\phi_{(0)} - \phi_{(l)} = \phi_D = \frac{qN_D}{2\varepsilon} l^2$$

$$\therefore \mathrm{l} = \sqrt{\frac{2\varepsilon\phi_D}{qN_D}}.$$

This allowed us to determine the depletion layer width.

Now, we consider applying a voltage to the semiconductor in this equilibrium state. If we apply a positive bias V, the built-in potential increases and becomes: $\phi_D + \phi$. In the case of reverse bias, it is: $\phi_D - \phi$. Therefore, the expression for the depletion layer width considering the application of bias is shown as:

$$\mathrm{l} = \sqrt{\frac{2\varepsilon(\phi_D + \phi)}{qN_D}}.$$

Now, considering the charge density Q per unit area in the depletion layer, we have

$$\mathrm{Q} = -\mathrm{q}N_D\mathrm{l} = -\sqrt{2qN_D\varepsilon(\phi_D + \phi)}\,.$$

The electrical capacitance C obtained by differentiating this charge density with potential is shown as:

$$\mathrm{C} = \frac{dQ}{d\phi} = -\sqrt{\frac{qN_D\varepsilon}{2(\phi_D + \phi)}}.$$

This is called the Mott-Schottky equation.

This electrical capacitance C can be measured by applying a small AC voltage to it while a DC voltage is applied. If the value of C measured in this way for each potential is plotted with C^{-2} on the vertical axis and the potential on the horizontal axis, 1/C2 is shown as:

$$\frac{1}{C^2} = \frac{2(\phi_D + \phi)}{qN_D\varepsilon}$$

where the x-intercept is the potential $\phi = \phi_D$, i.e., the built-in potential.

Since the slope of the line is 2/qNDε, the donor density can be determined from this. This 1/C2-Φ plot is called the Mott-Schottky plot.

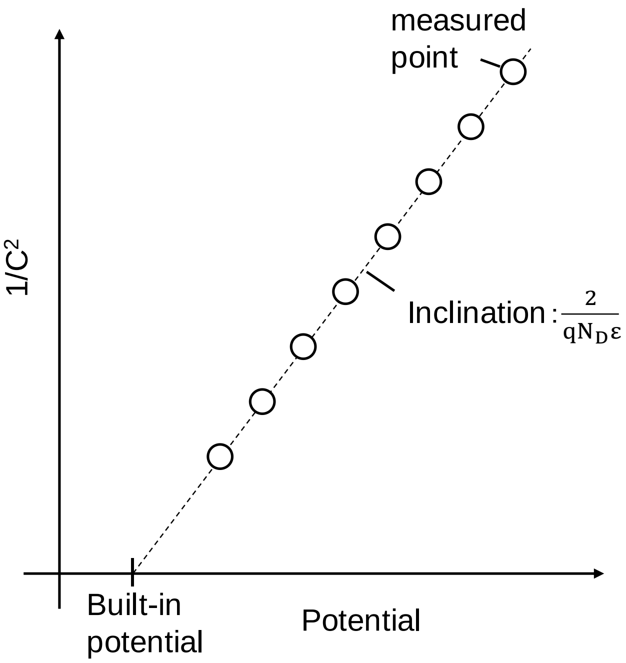

Fig.3.7. Commonly Mott-Schottky plots

3.2.4. *Photo-electrochemical measurement*

When photo-excitation occurs at a semiconductor electrode, the photo-effect on the redox reactions at the semiconductor/electrolyte interface is clearly visible. Since the change in the amount of redox reactions is observed by measuring the currents, the voltammogram measured in the state of photo-excitation reflects the photo-effect on the redox reaction. In this thesis, the measurement of voltammetry in the photo-excited state of the semiconductor electrode is called “photo-electrochemical measurement”. Fig. 3.8 shows a simple schematic diagram of the photoexcitation generated by light incident on a semiconductor. The schematic diagram shows (a) photon incidence, (b) generation of electron-hole pairs by photo-excitation, (c) separation of electron-hole pairs in the depletion layer, transport of electrons to the bulk side and holes to the semiconductor/electrolyte interface, and (d) interfacial carrier transfer across the semiconductor/electrolyte interface, respectively.

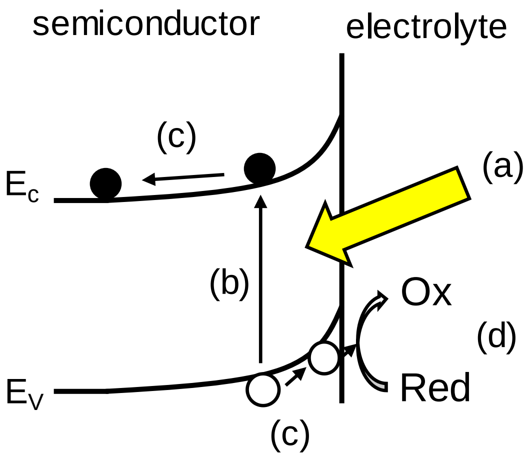

Fig. 3.8. The simple description of photo-effect in a semiconductor

The rate at which incident photons are converted into the redox currents is called the incident photon current efficiency, which is expressed by the following equation[2)]:

$$\mathrm{IPCE}(\%) = \frac{hc\left|J_{\mathrm{ph}} - J_{\mathrm{dark}}\right|}{q\lambda P_{\mathrm{IN}}} \times 100,$$

where h is Planck's constant, c is speed of light, q is elementary charge, P_{IN} is light intensity, and J_{ph} and J_{dark} are current density under irradiation and dark condition, respectively. Thus we can calculate IPCE from the results measuring current of electrodes under monochromatic light.

Since the IPCE is affected by the efficiency of each elements in the optical effect, the combined information of these elements is obtained. When illuminated with light of energy below the band gap, the IPCE is almost zero because basically no photocurrent is generated. When illuminated with light of energy above the band gap, the IPCE is usually defined by the efficiency of carrier separation. Since the optical carriers are separated by the depletion layer in the semiconductor at the semiconductor/electrolyte interface, the relationship between the depletion layer width and the light penetration length is important. When the light penetration length is much smaller than the depletion layer width, the IPCE is high because most of the light carriers can contribute to the redox reactions. On the other hand, if the light penetration length is much larger than the depletion layer width, only some of the photo-carriers contribute to the redox reaction, and the remaining carriers are removed by recombination, resulting in the low IPCE. In nitride semiconductors, because of the direct transition type, the photo-absorption efficiency is high, and when illuminated with the light having an energy higher than the band gap, the IPCE is high even if the depletion layer width is not increased by applying a voltage.

3.3. Plasma Etching Process

3.3.1. Inductive Coupled Plasma Reactive Ion Etching (ICP-RIE) [7)]

The role of etching in the semiconductor process is to process various thin film materials that make up electronic devices and fine patterns on the semiconductor surface according to the mask pattern. For applications that do not require fine patterns, wet etching is employed, in which the wafer is immersed in an etchant that is suited to the characteristics of the target material for a specified period of time. This method has inexpensiveness of the equipment and highly productively since a large number of wafers can be processed at once. On the other hand, however, it has some disadvantages such as difficulty in controlling the etching reaction rate to keep it constant, inability to detect the end period of etching, and difficulty in processing the etchant. Therefore, the application of plasma process was considered as an alternative to wet etching, and it was introduced to IC manufacturing in the early 1970s. This type of etching utilizing plasma is also called plasma etching or dry etching without the electrolyte. The plasma used for etching at that time had a high gas pressure of several tens of Pa and a low discharge power, so the average free process of ions was about 0.1 mm and the density was about 10^{10} cm^{-3}. Therefore, the contribution of ions to etching can be neglected because the energy of ions incident on the wafer is small and their number is also small. Taking the etching of Si as an example, a gas containing CF_4 is discharged and F atoms are generated in the plasma by the following dissociation reaction.

$$CF_4 + e \rightarrow CF_3 + F + e$$

The generated F atoms diffuse to the wafer surface and etch Si by causing the following reactions on the surface.

$$\mathrm{Si} + 4\mathrm{F} \rightarrow SiF_4$$

However, in plasma etching, F atoms fly into the wafer surface from random directions by collisions. Therefore, if only these pure chemical reactions are used, in addition to depth etching, side etching proceeds from the edge of the mask, resulting in isotropic etching as in wet etching. In isotropic etching, undercuts occur under the mask, resulting in an inaccurate finish to the mask pattern. For this reason, there is a limit to the application of isotropic etching to fine patterns, although some efforts are made to form patterns with dimensions that include the undercut in the mask design stage. Therefore, in wafer processes such as LSI, anisotropic etching, in which side etching hardly occurs and etching proceeds only in the depth direction as per the mask, is indispensable. Such etching can be achieved by accelerating ions of rare gases such as Ar with an electric field and launching them vertically into the wafer. This is because sputtering occurs when the fast ions hit the layer to be processed, knocking out its constituent atoms. However, in this type of sequential physical etching, the difference in etching speed (selectivity ratio) depending on the material is small, so both the mask and the substrate are etched in the same manner, making it difficult to selectively process only the layer to be etched. Therefore, plasma etching technology has been developed to ensure sufficiently small etch rate for the mask and substrate, and anisotropic etching for the layer to be processed. As a typical example, reactive ion etching using CCP with parallel plate electrodes was first put to practical use in the 1980s, and in the 1990s, etching systems using high density plasma such as ICP were developed. These systems utilize the advantages of both chemical and physical etching, and have become the mainstream of plasma etching today. The features of plasma etching can be summarized as follows.

Plasma is explained here. Particles, such as atoms, molecules, ions, and electrons, obtain energy from outside and increase their kinetic energy, causing matter to undergo phase transitions from solid to liquid to gas. The gas molecules further dissociate into atoms. As the temperature of the dissociated gas is further increased, the energy from the thermal motion of the atoms becomes greater and greater, and some or all of the electrons are freed from the bonds of the nucleus. Plasma is a state in which a large number of atoms are ionized, producing groups of electrons and ions, which are mixed together. Since the amount of positive and negative electricity is almost equal, the plasma as a whole remains neutral.

In the plasma generation process, the use of a high-frequency power supply instead of a DC power supply is very important because it enables discharge even when there are insulators on the electrodes. One of the most widely used methods is RF discharge using radio frequency band. There are two methods of generating RF discharges: CCP and inductively coupled plasma (ICP). Figure * shows an example of ICP, which is being applied to etching because of its ability to produce high density plasma at relatively low gas pressure.

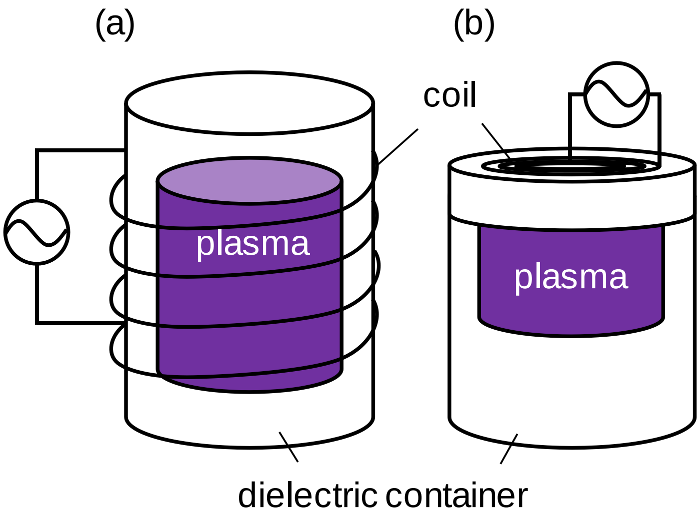

Fig.3.9 The way of generate inductively coupled RF discharges
(a) cylindrical (b) plane

Finally, we will discuss the damage caused by plasma. Plasma can cause the following two types of damage on the etching surface that do not occur in wet etching: 1) physical damage due to ion impact, and 2) electrical damage due to charge. Physical damage can be evaluated by the incident energy and grain flux of the ions, and can be estimated from the sheath tube voltage and plasma density. On the other hand, electrical damage includes dielectric breakdown due to charge-up of the gate dielectric of MOS devices.

3.4. Structural characterization

3.4.1. Scanning electron microscopy (SEM)

In a scanning electron microscope (SEM), a stream of electrons generated by an electron gun is accelerated to the speed of light and then narrowed down to an electron beam that irradiates the surface of a sample. Depending on the interaction between the sample and the electron beam (electron probe), the electrons can be divided into those that are reflected from the sample, those that pass through the sample, and those that excite the atoms inside the sample. Electrons reflected from the sample surface have different reflectance depending on the elements on the surface, so the reflected electrons can be obtained by detecting the reflected electrons. Similarly, the transmitted electrons are diffracted through the crystal and are used for transmission electron microscopy (TEM) by using their diffraction patterns. Electrons that penetrate several tens of nanometers into the sample excite internal electrons and emit X-rays, cathode rays, and secondary electrons into the sample; the secondary electrons are the main source of information for SEM detection, while other reflected electrons can be extracted separately because they have different energies.

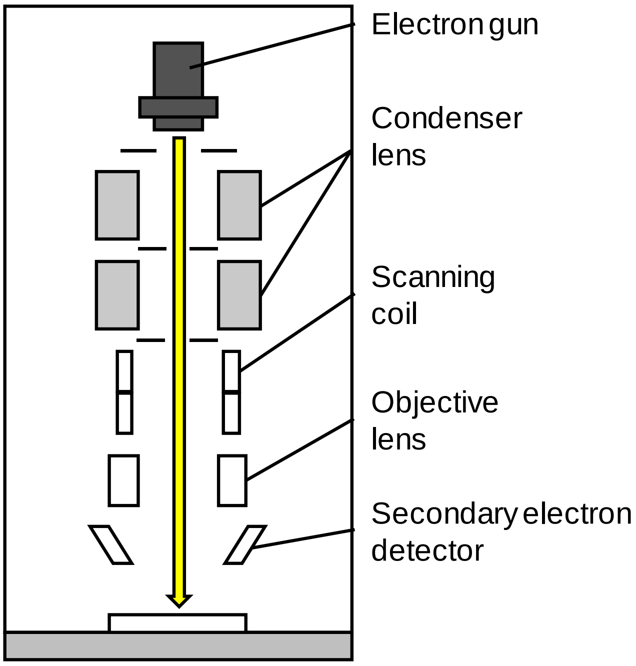

Fig.3.10 Schematic graph of SEM

3.4.2. Atomic force microscopy (AFM)

The atomic force microscopy (AFM), which is one of a scanning probe microscopy (SPM), provides three-dimensional surface topography by detecting the attractive and repulsive forces between a cantilever and an object surface [4]. Though the lateral resolution of AFM is relatively low, the vertical resolution can be up to sub-angstrom. The interaction between a cantilever and an object is monitored by an optical probe to read a minute Z-direction displacement: changes in the cantilever deflection or oscillation amplitude are determined by detecting the changes in the laser beam reflected on the back of the cantilever. Z-axis drive of the cantilever can be accurately operated by using a piezo device.

The operation modes of the AFM systems can be classified into two groups: "contact mode" and "tapping mode". In the contact-mode AFM, cantilever deflection affected by contacting a cantilever on an object are utilized to provide a topography. The change in cantilever deflection is monitored by the optical probe while raster-scanning the object. A cantilever deflection is kept constant by adjusting the vertical position of scanner to maintain an optical signal constant. This feedback loop maintains a constant force between a cantilever and an object during imaging. In the tapping-mode AFM, cantilever oscillation during tapping the tip on the surface is utilized to provide a topography. The optical probe monitors the root-mean-square (RMS) amplitude of cantilever oscillation. An oscillation amplitude is kept constant by adjusting the vertical position of scanner. This feedback loop maintains a constant distance between a cantilever and an object during imaging. Since tapping mode AFM can provide a topography without contacting an object sample, no damage is induced during imaging. Furthermore, the lateral, shear forces present in contact mode can be eliminated. These features enable us to obtain the topography of soft, fragile, and adhesive surfaces without damaging them.

In this study, we used OLYMPUS LEXT4500 which integrating optical microscope and an AFM system, enabling to obtain both microscopic image and topological image of the area of interest. AFM was operated at tapping mode to obtain the surface topography without damaging on samples. Silicon tips (OLYMPUS OMCL-AC240TS-C3) with radius of 7 nm and resonance frequency of 70 kHz were used as cantilever.

3.5. Optical characterization

3.5.1. Ultraviolet-visible-infrared (UV-VIS-IR) spectroscopy

UV, visible, and near-infrared spectroscopic methods differ greatly depending on the sample being measured, but in this section, we will discuss methods for measuring semiconductors.

Each semiconductor material has its own band structure, which causes interaction with light. When a semiconductor is irradiated with monochromatic light, some of the photons are reflected from the surface, while the rest enter the semiconductor. The incident photons are absorbed as they enter the semiconductor, and the unabsorbed photons are emitted by the backside, which are detected as transmitted light. The band gaps of most semiconductors are located in the ultraviolet, visible, and near-infrared regions (about 1100 nm for Si and about 360 nm for GaN), and by irradiating light in these wavelength regions, it is possible to obtain reflection, absorption, and transmission spectra that are unique to the semiconductor properties. This is called ultraviolet, visible, and near-infrared spectroscopy.

In the above process of reflection, absorption, and transmission of light, if the reflectance is R, the absorption rate is A, and the transmission rate is T, the relationship R+A+T=1 is established. In general, it is difficult to derive the absorption coefficient directly, so in many cases, the absorption coefficient is derived by measuring the reflectance and transmittance using a photometer.

As shown in the figure below, consider the case where light is incident from medium 1 to medium 2.

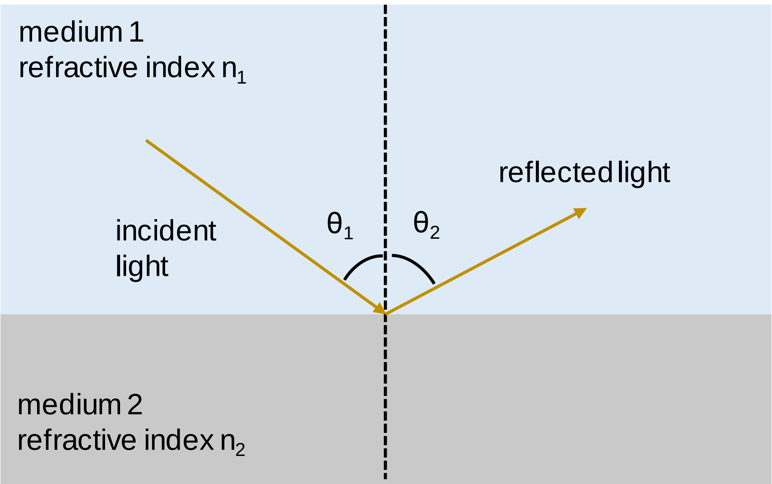

Fig.3.11 Schematic graph of an incident from medium 1 to medium 2

The reflectance is respectively different for p-polarized and s-polarized light as:

$$R_p = \left(\frac{n_2 cos\theta_1 - n_1 con\theta_2}{n_1 con\theta_2 + n_2 cos\theta_1}\right)^2$$

$$R_s = \left(\frac{n_1 cos\theta_1 - n_2 con\theta_2}{n_1 con\theta_1 + n_2 cos\theta_2}\right)^2.$$

This is called the Fresnel equation. In the case of measuring the vertical reflectance, the angle of incidence and the angle of reflection are both zero, so

$$R_p = R_s = \left(\frac{n_2 - n_1}{n_2 + n_1}\right)^2.$$

In particular, if the medium 1 is the atmosphere, the refractive index can be considered to be almost unity, which can be further simplified and the reflectance can be considered to reflect only the refractive index of medium 2.

3.6. Electrical characterization

3.6.1. Current-voltage (I-V) measurement

In this study, we measured current-voltage (*I-V*) characteristics of Ni/AlGaN/GaN diodes and HEMTs after EC process. We employed Agilent B1500A Semiconductor Device Analyzer in which built-in HDD and DVD drive, Windows 7 are embedded. The instrument is totally operated with Agilent EasyEXPERT software installed in B1500A itself. IV measurement module is Keysight B1517A High Resolution Source/Measure Unit with following specification: source and measurement range up to 100 V, 0.1 A; minimum measurement resolution of 1 fA, 0.5 µV; minimum source resolution of 5 fA, 25 µV.

3.6.2. Capacitance-voltage (C-V) measurement

In this study, we measured capacitance-voltage (*C*-*V*) characteristics of Ni/AlGaN/GaN diodes after EC process. We employed Yokogawa-Hewlett-Packard 4192A Impedance Analyzer. The instrument is connected to the external laptop computer using GPIB interface. Measurements are automatically carried out using a control-software which is developed with National Instrument LabVIEW. The measurement duration per point and resolution are approximately 1.1 s and 0.1 pF, respectively.

Reference

[1] J. Bard, and L. R. Faulkner, "Electrochemical Methods, Fundamentals and Applications", John Wiley & Sons, New York, 2013.

[2] Z. Chen, H. N. Dinh, and E. Miller, "Photoelectrochemical Water Splitting: Standards, Experimental Methods, and Protocols", Springer-Verlag New York, New York, 2013.

[3] J. I. Goldstein, and H. Yakowitz, "Practical Scanning Electron Microscopy: Electron and Ion Microprobe Analysis", Springer US, New York, 1975.

[4] G. Binnig, and C. F. Quate, "Atomic Force Microscope", Phys. Rev. Lett., vol. 56, pp. 930–933, 1986.

[5] B. L. Anderson, and R. L. Anderson, "Fundamentals of Semiconductor Devices", McGraw-Hill Companies, New York, 2005.

[6] G. D. Gilliland, "Photoluminescence spectroscopy of crystalline semiconductors", Mater. Sci. Eng., vol. R18, pp. 99–400, 1997.

[7] Y. Ichikawa, T. Sasaki, and N. Tsutsui, “Plasma Semiconductor Process Enigineering Introduction to Film Deposition and Etching”.

Chapter 4

Anisotropic PEC etching for low-doped GaN

4.1. Introduction

As mentioned in Chapter 1, Gallium Nitride (GaN) is a semiconductor material that has a higher breakdown electric field and saturation electron velocity than silicon, which is currently the mainstream material in the field of power devices. There are two main types of the GaN-based devices, which are a horizontal device or a vertical device. Currently, the mainstream of GaN-based devices is a horizontal device that utilizes 2DEGs accumulated at the AlGaN/GaN heterostructure interface, and this type of device has already been commercialized. Although these devices are very useful for high-frequency devices, there are some problems from the viewpoint of power devices. One example is the difficulty of threshold voltage control. Although there are several methods to shift the threshold voltage in the positive direction, it is difficult to set the threshold to a large voltage value, such as over 3-5V. In addition, in order to achieve a breakdown voltage value exceeding 1kV, the distance between the gate and drain must be increased, which is a trade-off for high integration.

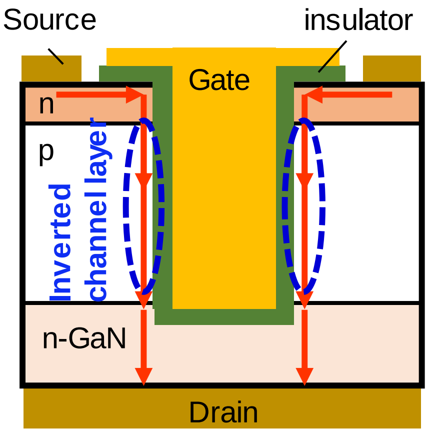

Fig. 4.1 Schematic diagram of a trench gate MOSFET device structure

Therefore, in the field of power devices, GaN-based vertical transistors are very attractive. This is also due to the fact that GaN crystal growth technology has recently become so advanced that it is now possible to develop freestanding GaN substrates with low dislocation density and high quality. Vertical transistors have the high breakdown voltage and low on-resistance, and in addition, the channel layer extends vertically, which has the advantage of enabling to have both higher breakdown voltage and higher integration. Among the GaN vertical transistors, the trench gate MOSFET is one of the major transistors. Its schematic diagram of the device structure is shown in Fig. 1.

The structure of this device was first reported in 2008, and unlike the GaN-based devices utilizing 2DEGs, it has normally-off operation. In recent years, the trench-gate MOSFETs have shown great promise as low-loss power transistors, with low on-resistance of less than 2 $\mathrm{m\Omega\ cm^{-2}}$, high current density, and breakdown voltages exceeding 1.2 kV*). However, like other nitride semiconductor devices, this device also faces has the problem involved in the damage in the etching process. In particular, since the trench gate structure requires a larger amount of etching than horizontal devices, the damage introduced by dry etching is larger than in other lateral devices, and the desired performance as expected from the material characteristics has not been obtained. Therefore, the establishment of low-damage etching technology for the trench stucture is desired.

As mentioned in Chapter 1, I have been focusing on Photo-Electrochemical (PEC) etching technology, which is utilizing photoelectrochemical reactions, as this low-damage etching technology. However, there is a problem in applying PEC etching to trench gates. The anisotropic PEC etching technology to fabricate high aspect ratio structure on an n-type GaN substrate with relatively low donor density of around 10^{16}~10^{17} cm^{-3} has not yet been established. The trench-gate MOSFETs often have a lamination structure of n+-p-n, so it is important to perform anisotropic etching on substrates with different doping densities. For the n^+-GaN substrate, it has been reported that it is possible to fabricate very high quality high aspect ratio structures by electrochemical (EC) etching using local breakdown [6)], as described in Chapter 2. In principle, the same should be possible for p-type GaN, where holes are the majority carriers. However, this technique cannot be applied to n-GaN, which has a relatively low donor density. This is because the applied voltage required for breakdown is an order of magnitude higher than for n^+-GaN substrates. Therefore, EC etching cannot be used for n-GaN substrates, however, on the other hand, it is also difficult to fabricate high-quality, high-aspect-ratio structures using PEC etching.

Figure 2 shows a schematic diagram of the fabrication of a porous structure, which is the high aspect ratio structure, of n-GaN by PEC etching.

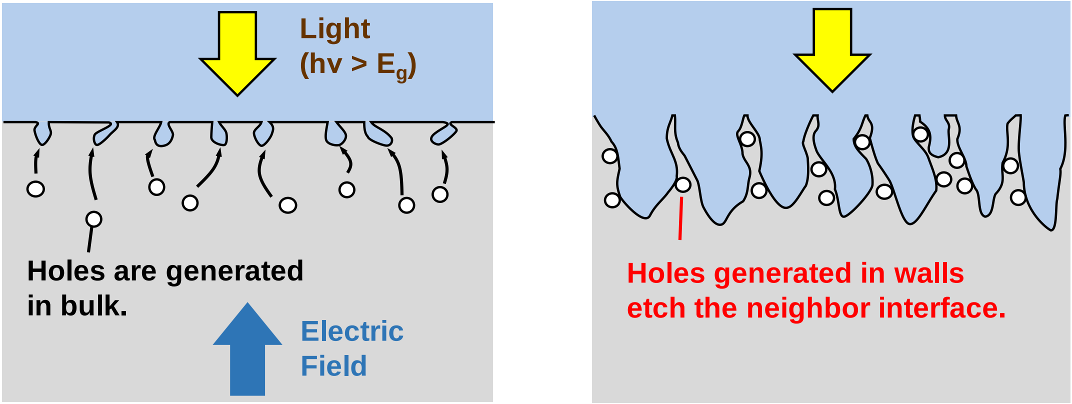

Fig. 4.2 Schematic diagram of porous structure fabrication of n-GaN substrate using PEC etching (a) Initial stage (b) sufficient irradiation time

In the initial stage of fabrication, the porous structure is self-organized. However, after sufficient fabrication time has elapsed, due to the principle of PEC etching in which the entire surface is illuminated by light and holes are supplied, holes are generated even within the pore walls, and these holes are used to dissolve the nearby pore walls. As a result, the porous structure does not grow above a certain depth because the top surface area is lost due to the dissolution. This is the reason why it is not possible to fabricate high aspect ratio structures with PEC etching, and is a problem for fabricating trench structures on n-GaN substrates. In order to fabricate high-aspect-ratio structures, it is important to supply holes locally only to the areas to be etched, such as the tips of the pores.

In order to solve the problem, I focused on the unique optical absorption property of GaN at the GaN/electrolyte interface in the presence of a high electric field, namely the Franz-Keldysh (F-K) effect. As mentioned in Chapter 2, the F-K effect is a phenomenon in which light with a longer wavelength than the normal wavelength can be absorbed, which is called as “sub-bandgap light” in this chapter, in a semiconductor under a high electric field. In other words, it is a phenomenon where light with energy below the band gap, which cannot be absorbed normally, can be absorbed with the help of the electric field. When a voltage is applied to a substrate with an uneven structure such as a porous structure, a high electric field exists at the tip of the pores, even though a breakdown does not occur. Therefore, there is an absorption coefficient of the sub-bandgap light at the pore tips that cannot be absorbed in the bulk, and if sub-bandgap light is illuminated from the surface in this state, the light is transmitted through the surface where there is no absorption coefficient, while the light is absorbed at the tip of the pores where there is a high electric field. The experiment was based on the concept that carriers are supplied only at the tip of the pores, and a high aspect ratio structure can be fabricated.

In this Chapter, I analyzed the electric field absorption effect observed at the GaN/electrolyte interface for the GaN substrate with the initial processing structure, and developed the anisotropic PEC etching technique for GaN using F-K effect. By calculating the change in the optical absorption coefficient at each wavelength based on the potential barrier generated at the GaN/electrolyte interface and reproducing the experimental values of photocurrent values, I demonstrated that the F-K effect occurs at the interface. I also applied the developed anisotropic PEC etching technique to low donor density GaN samples with the initial structure, and discussed the structural controllability for the fabrication of trench structure and its usefulness.

4.2. Experimental details

The electrochemical experiments were performed using a three-lectrode cell [5,6]. We used a 3-μm-thick n-type GaN layer with N_D = 5×10^{16} cm−3 grown on (0001) freestanding GaN substrate as a working electrode. First, we conducted photo-electrochemical (PEC) measurements on a planar GaN electrode using a 0.1 mol/L phosphatebuffered salt (PBS) solution with a pH of 7.4. Then, porous structures were formed by PECetching in a mixture of 1 mol/L H_2SO_4 and 1 mol/L H_3PO_4 with a pH of 1.4. From the Mott-Schottky analysis, we obtained an N_D of 4.9×10^{16} cm^{-3}, which is very consistent with the designed value. For the anisotropic EC etching of the n-type GaN layer, the porous structure was first formed by photo-assisted EC etching under irradiation of light with a higher hv than E_G. Then, we tried to extend the pores in the depth direction utilizing a sub-bandgap light with a lower hv than E_G. For all experiments, a monochromatic light passing through band-path filters was irradiated in the top-side illumination mode. The structural properties of the porous GaN structures were evaluated by scanning electron microscopy (SEM).

4.3. Franz-Keldysh effect

First, I will discuss the F-K effect, which is very important phenomenon in this experiment. When light is incident on a semiconductor, the absorption coefficient, the reflection coefficient, and the refractive index of the light are changed by applying an electric field to the semiconductor. The effect is called as “electro-absorption”. In the photo-absorption spectrum of a semiconductor, a sharp increase in the absorption coefficient is observed at wavelengths shorter than those corresponding to the band gap energy. This is called the fundamental photo-absorption edge of the semiconductor. W. Franz and L.V. Keldysh independently treated the electric field change of the fundamental photo-absorption edge in 1958, and showed that the wavelength of the absorption edge shifts to the long wavelength side in proportion to the square of the applied electric field, and that this shift is sufficiently large to be observable at 10^5~10^6 V/cm*).

The band structure of a semiconductor under an electric field is bent. Under a high electric field, F, applied to a semiconductor, the electron and hole wavefunction seeps into the forbidden band and exponentially decreases. In such a situation, sub-bandgap absorption is possible due to photon-assisted tunneling throughout the forbidden band 7). The phenomenon is F-K effect. Recently, Maeda et al. 8) have reported that sub-bandgap absorption was observed in GaN pn-junction diodes whose current transport characteristics were well explained by considering the F-K effect. The absorption coefficient, α, can be expressed as follows 7).

$$\alpha(\omega,F) \simeq \frac{\alpha_b}{32\pi^2}\frac{f(F)}{(E_g-\hbar\omega)} exp\left\{-\frac{4}{3f(F)}\left[\frac{2m_r(E_g-\hbar\omega)}{\hbar^2}\right]^{\frac{3}{2}}\right\},$$

where $$f(F) = qF\frac{2m_r}{\hbar^2}. \qquad (1)$$

Here, ω is the angular frequency of light, q is the elementary charge, $\hbar$ is the reduced Planck constant, and mr is the reduced electron-hole mass. In this study, α_b is regarded as a constant physical parameter, whose value was determined by fitting it to the current–voltage (I–V) characteristics (discussed later).

4.4. Electro-absorption at GaN/Electrolyte interface

In the n-GaN/electrolyte interface, as mentioned in Chapter 3, there is a potential barrier and a depletion layer electric field. In order to calculate the depletion layer electric field, the built-in potential (V_{bi}) is indispensable. Therefore, I performed C-V measurements in the electrolyte and created a Mott-Schottky plot based on the results. The results are shown in Figure 4.3.

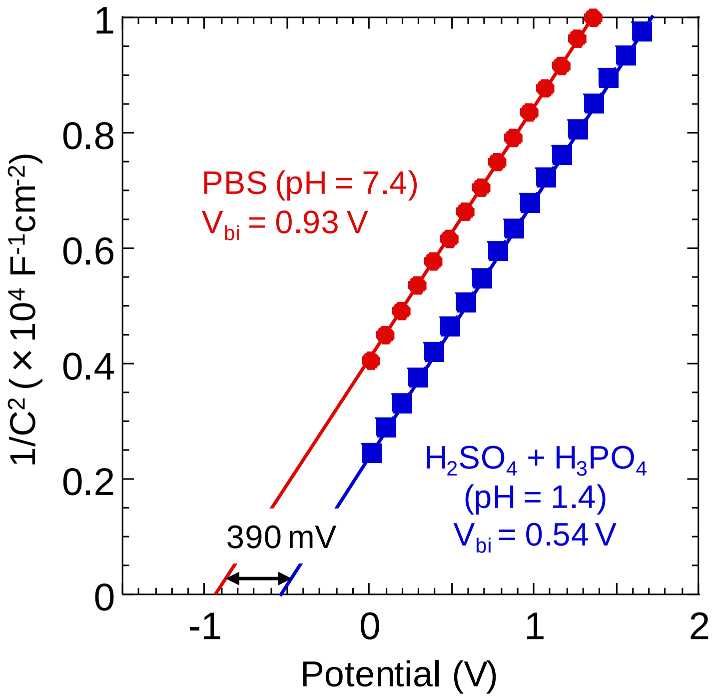

Fig. 4.3 Mott-Schottky plots measured in each electrolyte

Red circles are the result of the measurement in PBS at pH 7.4, and the V_{bi} was 0.93V. The blue circles are the result of measurement in a mixture of 1 mol/L H_2SO_4 and 1 mol/L H_3PO_4 at pH 1.4, and the V_{bi} was 0.54V. The difference in the V_{bi} was 0.39 V, which was almost the same as the difference in the V_{bi} calculated from the shift in pH using the Nernst equation.

The electric field *F* in the depletion layer at the GaN/electrolyte interface was calculated using the obtained V_{bi}. In this calculation, the V_{bi} was fixed at 0.93 V in PBS. The results are shown in Figure 4.4 (a).

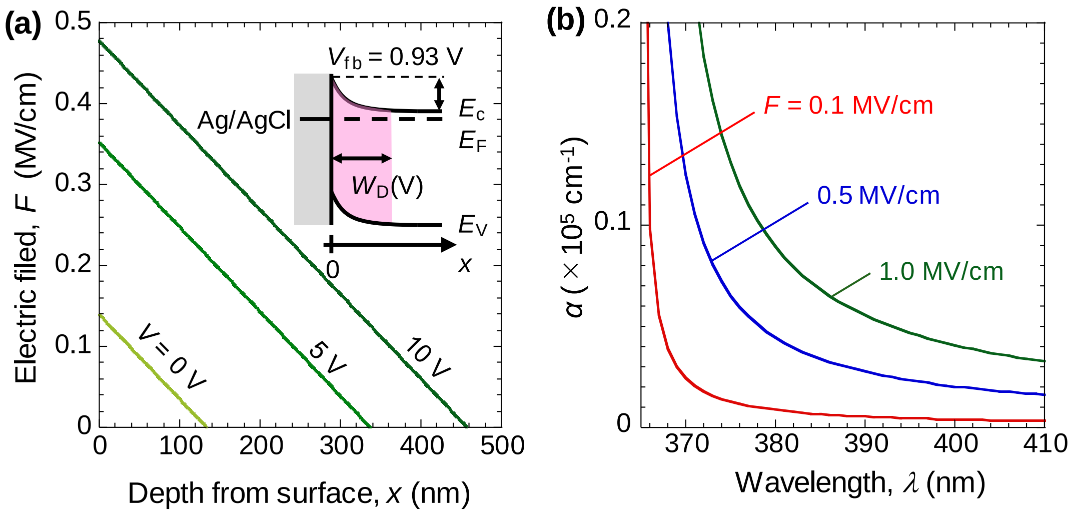

Fig.4.4. (a) Calculation of the *F* induced in the depletion layer as a function of *x* under applied *V*. (b) Theoretical curves of α calculated for sub-bandgap illumination.

The depletion layer width, $W_D(V)$, and the electric field, $F(x, V)$, were represented as a function of the applied voltage, *V*, by the following equation [9].

$$W_D(V) = \sqrt{\frac{2\varepsilon_0\varepsilon_s}{qN_D}\left(V_{fb} - V\right)} \qquad (2)$$

$$F(x, V) = \frac{qN_D}{\varepsilon_0\varepsilon_s}\left(W_D(V) - x\right) \qquad (3)$$

where, ε_0 and ε_s are the permittivity of vacuum and the relative permittivity of GaN, respectively. In the Fig. 4.4 (a), the vertical axis represents the electric field strength in the depletion layer, and the horizontal axis represents the depth x in the bulk direction when the GaN/electrolyte interface is 0. I also calculated the electric field when the applied voltage was 0, 5, and 10 V, respectively. The highest electric field, F_{max}, is induced to the surface of n-GaN, which was obtained using $x = 0$ in Eq. (3). As shown in Fig. 4.4 (a), I found that F_{max} approached 0.5 MV/cm at $V = 10$ V in the present case with $V_{\mathrm{fb}} = 0.93$ V and $N_{\mathrm{D}} = 4.9 \times 10^{16}$ cm^{-3}.

Fig. 4.4 (b) shows α calculated using the above Eq. (1) with varying F. As shown in the Fig. 4.3 (b), the result shows that even the sub-bandgap light can be absorbed at the GaN/electrolyte interface with a high electric field.

4.5. Simulation of Photocurrents under UV light illumination

From the above results, it was found that sub-bandgap absorption could occur sufficiently in this experimental system, so I actually irradiated sub-bandgap light to the GaN sample in the electrolyte and discussed whether the sub-bandgap absorption was occur and it was due to the F-K effect.

Figure 4.5 (a) shows the experimental data of I–V characteristics measured on planar n-GaN electrodes under illumination with a P_{in} of 0.2 mW/cm^2.

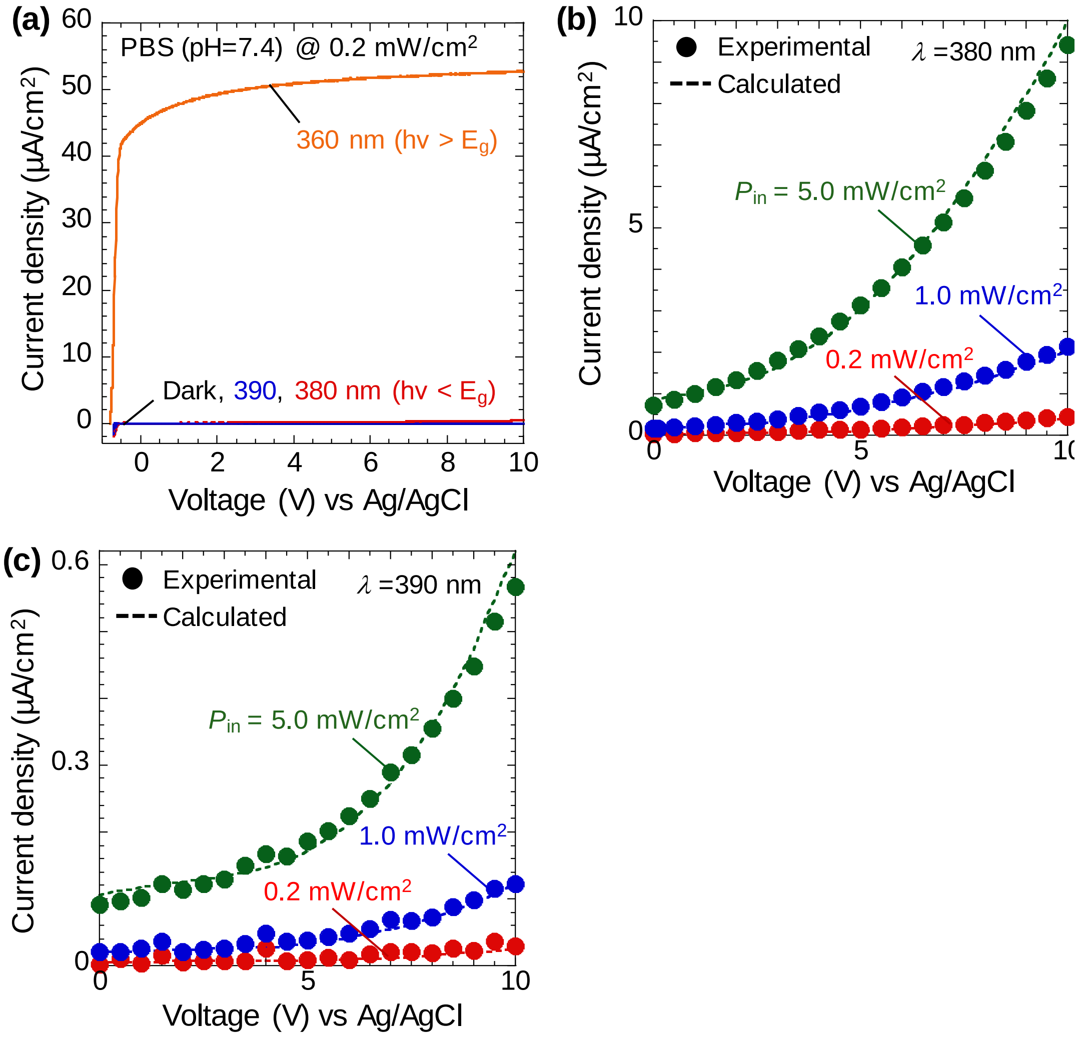

Fig. 4.5. Photocurrents measured on n-type planar GaN in PBS electrolyte with (a) $\lambda = 360$, 380, and 390 nm at $P_{in} = 0.2$ mW/cm^2. Experimental and theoretical curves obtained with (b) $\lambda = 380$ nm at $P_{in} = 0.2$, 1.0, and 5.0 mW/cm^2, and (c) $\lambda = 390$ nm at $P_{in} = 0.2$, 1.0, and 5.0 mW/cm^2

The potential barrier formed at the electrolyte/n-GaN interface gave us rectifying behavior like that of a Schottky diode. A large photocurrent was observed under illumination with $l = 360$ nm ($hv > E_g$), where no current was detected under illumination with $l = 380$ nm and 390 nm as well as in the dark condition. However, as P_{in} increased, photocurrents were clearly observed even under sub-bandgap illumination. Figs 4.5 (b) and 4.5 (c) show the photocurrents observed under illumination with $l = 380$

nm and 390 nm, respectively. The photo-currents exponentially increased with increasing V, and the values strongly depended on P_{in}. This behavior was quite different from the current saturation characteristics observed at l = 360 nm.

We conducted a theoretical analysis on the I–V characteristics to explain the photocurrents observed under sub-bandgap illumination. For the calculation, we divided the depletion layer into an infinitesimal length, dx, and a at each point was calculated using Eq. (1). The number of photons reached at x was represented by $F_0 \exp(-ax)$, where F_0 is the photon flux of incident light. Then, the total photocurrents, I [A/cm^2], were obtained by the following equation [8,10].

$$I_{(V)} = q\Phi_0 \left\{1 - exp\left(-\int_0^{W_D} \alpha_{(\omega,F_{(x,V)})} dx\right)\right\} \tag{4}$$

The photocurrents calculated using Eq. (4) were compared with the experimental data in Figs. 2(b) and (c). Here, a_{b}, which appeared in Eq. (1), was set to be 1.35×10^{-17} eV·cm^2, which is not far from the estimation of 1.07×10^{-17} eV·cm^2 for the case of n-GaN layer grown on a sapphire substrate.[11] The theoretical curves showed good agreement with all the experimental data obtained by changing P_{in} in the range of 0.2 – 5.0 mW/cm^2 for both l = 380 nm and 390 nm. These results indicate that the photo-currents obtained under sub-bandgap illumination could be explained by taking into account the Franz-Keldysh effect.

4.6. Anisotropic PEC etching for low-doped GaN

From the above results, it was confirmed experimentally and computationally that the F-K effect was observed at the GaN/electrolyte interface, which resulted in the absorption of sub-bandgap light. Next, we irradiated the initial structure with sub-bandgap light and discussed whether localized etching occurs and whether it is possible to fabricate a high-aspect-ratio structure. In this experiment, a porous structure was used as the initial structure. The porous structure can be self-organized by PEC etching, and has both simplicity and low damage.

Before actually irradiating the porous structure with sub-bandgap light, I performed the potential simulation at the GaN/electrolyte interface with a one-dimensional (1D) Poisson's equation to see if there was really an electric field at the tip of the pores that could absorb the sub-bandgap light. The schematic diagram of the assumed porous structure is shown in Fig. 4.6 (a).

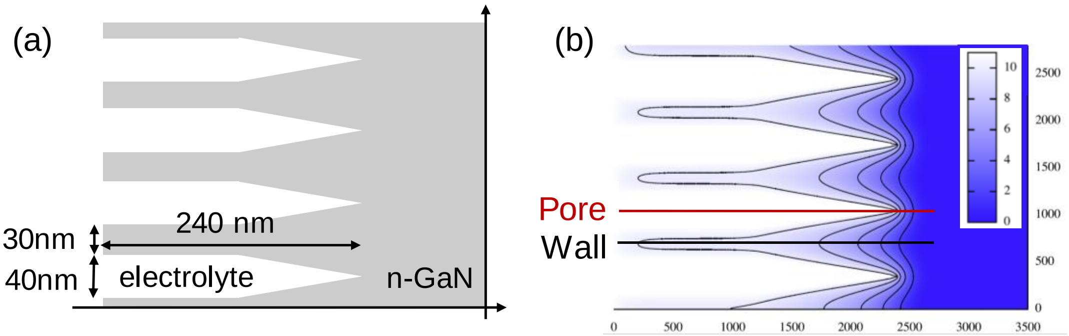

Fig.4.6 (a) Conceptual diagram of the porous structure used in the simulation
(b) The result of potential simulation using the 2D Poisson equation

The assumed porous structure had a pore diameter of 40 nm, a pore wall of 30 nm, and a pore depth of 240 nm. The potential distribution in the GaN sample was simulated with a potential difference of 1 eV and an applied voltage of 10 V at the GaN/electrolyte interface. The results are shown in Fig. 4.6 (b). We can see that the equipotential lines are clustered near the tip of the pore, suggesting the presence of a steep potential gradient, or strong electric field. Using the simulation result, I calculated the electric field distribution at the center of the pores across the tip and at the center of the pore walls. The results are shown in Fig. 4.7 (a).

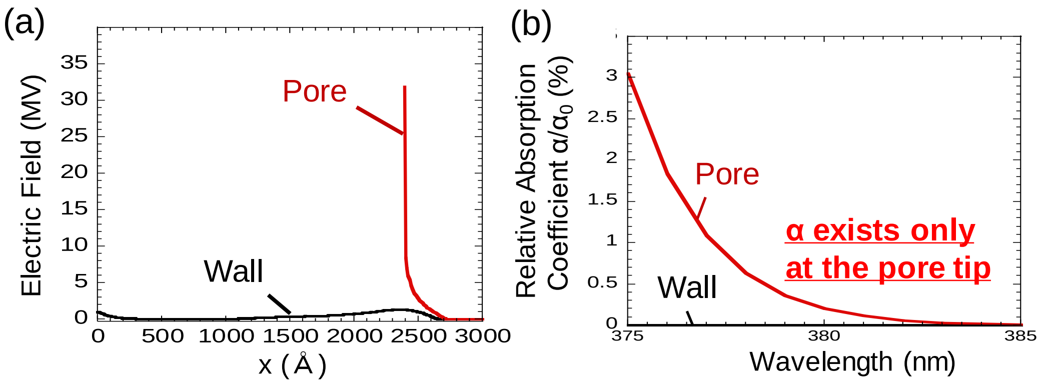

図 4.7 (a) Electric field distribution on the pore wall and inside the pore in the above simulation results (b) Absorption coefficients for each wavelength on the pore wall and inside the pore calculated based on (a).

In Fig. 4.7 (a), the vertical axis shows the electric field intensity, and the horizontal axis is the depth x in the above porous structure. It can be seen that there is a very strong electric field at around 240 nm, which is just the pore tip. I also calculated the distribution of the absorption coefficient using the calculated electric field distribution and the above equation (3). The result is shown in Figure 4.7 (b). It can be confirmed that the absorption coefficient of the wavelength around 380 nm exists only at the pore tip. From this result, it is confirmed that in the porous substrate, the absorption coefficient of light at 380 nm exists only near the pore tips where a very strong electric field exists. These results indicate that when the porous structure is under illumination with sub-bandgap light, the sub-bandgap photo-absorption does not occur inside the pore walls where there is no absorption coefficient, but only at the pore tips where there is a high electric field, which leads to sub-bandgap photo-absorption, local carrier supply and thus anisotropic local etching.

Based on the above results, the initial porous structure was fabricated and the morphology changes under illumination wtih sub-bandgap light in the structure were evaluated. Figure 3 (a) shows the SEM images of the initial porous sample formed just after the PEC etching with λ = 360 nm.

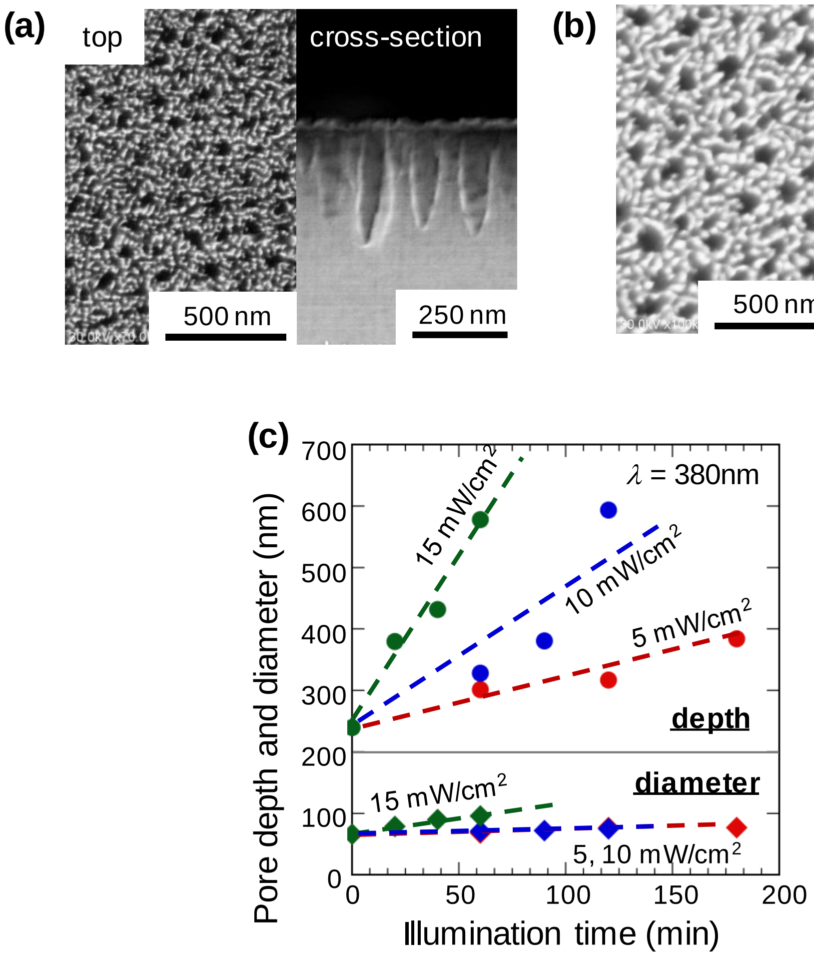

Fig. 4.8. SEM images of porous GaN samples formed by photo-assisted EC etching (a) before and (b) after the sub-bandgap illumination for 2 hours (λ = 380 nm at P_{in} = 15 mW/cm^2, and V = 10 V). (c) Average pore diameter and pore depth measured as a function of illumination time of sub-bandgap light.

The average values of the pore depth and diameter were 240 nm and 65 nm, respectively. The pore depth did not become deeper even with the longer processing time in the case of λ = 360 nm, as previously reported [5)]. Fig. 4.8 (b) shows the typical SEM images of the samples after a V of 10 V was applied for 2 hours under irradiation of light with λ = 380 nm at a P_{in} of 10 mW/cm^2. The average pore depth increased to 600 nm, but the pore diameter did not change that much after the sub-bandgap illumination. We have also conducted the irradiation of the sub-bandgap light with λ = 390 nm on the porous samples, however, could not see the significant difference in the pore shape between the two samples except for the pore length. This result suggests that the photo-assisted EC etching due to the sub-bandgap absorption preferentially proceeded at the pore tip, in which the high-electric filed was induced.

The average pore diameter and pore depth of the samples prepared by the sub-bandgap illumination are summarized in Fig. 3(c). In the case of the illumination at a P_{in} of 15 mW/cm^2, the pore diameter moderately increased with increasing illumination time. This is probably because the photo-carriers were also generated near the top surface under illumination with a higher P_{in}, in which the pore walls were slightly etched in the lateral direction. In the case of the illumination at a P_{in} of 5 and 10 mW/cm^2, the lateral etching rate of the pore wall was very small (below 0.1 nm/min). On the other hand, the etching rates in the vertical direction were much larger than those in the lateral direction, and they depended strongly on P_{in}. The vertical etching rates were roughly estimated as 5.6, 1.9, and 0.8 nm/min for a P_{in} of 15, 10, and 5 mW/cm^2, respectively. These results indicate that the pore depth formed on n-type GaN could be controlled by the light intensity, P_{in}, and time of sub-bandgap illumination.

4.7. Conclusion

In this Chapter 4, I analyzed the electro-absorption observed at the GaN/electrolyte interface and developed an anisotropic PEC etching technique of n-GaN with the initial structure. By calculating the electric field in the depletion layer based on the potential barrier at the GaN/electrolyte interface and the absorption coefficients at each wavelength based on the electric field strength, I indicated that sub-bandgap photo-absorption occurred at the interface. I measured the experimental photocurrent values of the sub-bandgap light and reproduced the experimental values by calculation using an equation that takes the F-K effect into account, and theoretically and experimentally demonstrated that sub-band photo-absorption occurred at the interface and that the F-K effect was involved in the absorption. In addition, by irradiating low-donor density GaN samples with the initial porous structure with sub-band light and evaluating the change in the surface morphology, I demonstrated that the local etching by PEC etching was possible even for low-donor density GaN samples. As a result, I indicated that it could be possible to establish a low-damage trench fabrication technique using PEC etching on low-donor-density GaN substrates.

Reference

[1] J. D. Beach, R. T. Collins, and J. A. Turner, *J. Electrochem. Soc.*, **150**, A899 (2003).

[2] K. Fujii, T. Karasawa, and K. Ohkawa, *Japanese J. Appl. Physics, Part 2 Lett.*, **44**, 4–7 (2005).

[3] A. P. Vajpeyi, S. J. Chua, S. Tripathy, and E. Fitzgerald, *Eurochem. Solid-State Lett.*, **8**, G85–G88 (2005).

[4] K. Al-Heuseen, M. R. Hashim, and N. K. Ali, *J. Electrochem. Soc.*, **158**, D240 (2011).

[5] A. Watanabe, Y. Kumazaki, Z. Yatabe, and T. Sato, *ECS Electrochem. Lett.*, **4**, H11–H13 (2015).

[6] Y. Kumazaki, S. Matsumoto, and T. Sato, *J. Electrochem. Soc.*, **164**, H477–H483 (2017).

[7] H. Haug and S. W. Koch, *Quantum Theory of the Optical and Electronic Properties of Semiconductors*, 5th ed., p. 349-370, World Scientific Co. Pte. Ltd, Singapore, (2012).

[8] T. Maeda et al., *Appl. Phys. Lett.*, **112**, 252104 (2018).

[9] S. M. Sze, *Physics of Semiconductor Devices*, 2nd ed., p. 248, John Wiley& Sons, New York, (1981).

[10] S. M. Sze, *Physics of Semiconductor Devices*, 2nd ed., p. 755, John Wiley& Sons, New York, (1981).

[11] J. F. Muth et al., *Appl. Phys. Lett.*, **71**, 2572–2574 (1997).

Chapter 5

Contactless Photo-electrochemical etching for GaN

5.1. Introduction

Gallium Nitride (GaN) is expect to apply to various devices, for example light emitter of blue or ultraviolet region, high power transistors and photoelectric conversion, due to the good optical and electric characteristics 1-7). Etching process is very important process among the entire fabrication process of GaN decices. Wet etching that had traditionally used for silicon or germanium cannot be used for GaN due to the chemical resistivity 8). Therefore, dry etching utilizing plasma is the main current for fabrication process of GaN devices. However, there is the subject that the etching technology introduce various damage on semiconductor surface owing to collision of plasma atoms and the damage lead to degradation of device performance 9-12).

Photo-Electrochemical (PEC) etching is low-damage etching for nitride semiconductors 13-19). In this method, the etching proceeds with the cycle of anodization on the semiconductor surface with holes supplied with photo-excitation and ions in the electrolyte and dissolution of the anodized surface in the pH controlled electrolyte. Compared with dry etching method, advantages of the method are low-damage etching and high controllability of the etching amount. There are many reports of the application of PEC etching with removal of the surface damage after dry etching or fabrication of the deep trench structure, mesa structure and recessed gate structure 20-25).

Recently, Contactless PEC (CL-PEC) etching which is the simplified PEC etching has been reported 26-35). The conventional PEC etching, as mentioned above, needs the contact to the external circuit in order to collect electrons supplied by photo-excitation and sealing the contact part from the electrolyte. On the other hand, for CL-PEC etching, the electrons are consumed by oxidizing agents in the electrolyte, so it can omit the various process of PEC etching which doesn't match the device process. In the etching, a sulfate radical ($SO4^{\cdot -}$) is commonly used as the strong oxidizing agents which consume the electrons. Two $SO4^{\cdot -}$ radicals are generated by photocomposition of a peroxysulfate ($S_2O_8^{2-}$) ion under the illumination of UV light with a wavelength below 310 nm 36, 37).

In this chapter, I simplified the CL-PEC etching process more for application to GaN based device process. Including our past reports, the potassium hydroxide (KOH) based electrolyte containing $S_2O_8^{2-}$ ions has been only used for CL-PEC etching so far. In these reports, titanium (Ti) or silica (SiO_2) thin layers has been used as the etching mask, which need two step process of deposition and patterning for the fabrication. In order to suit CL-PEC etching process to GaN based device process, I simplified the etching mask fabrication process. Specifically, I developed the phosphoric acid (H_3PO_4) based electrolyte for CL-PEC etching and demonstrated that positive type photoresist film was directly available as the etching mask in the electrolyte, which was not suitable to the KOH based electrolyte for the weakness of alkaline electrolyte. First, for investigation of basic etching electrolyte characteristics, I measured pH change of the electrolyte under illumination of UVC light and calculated $SO4^{\cdot -}$ radical production rate, which was a key parameter to determine the etching rate, from the pH change. Next, I measured the transmittance of the electrolytes containing various $K_2S_2O_8$ density and designed the CL-PEC etching setup for a GaN sample from the results. Finally, I conducted CL-PEC etching of a GaN sample with the positive type photoresist etching mask in the developed H_3PO_4 based electrolyte and discussed the CL-PEC etching in the weak acid electrolyte from the viewpoint of the durability of the etching mask, the etching rate and the surface morphology after the etching.

5.2. Experimental details

In this experimental, each $K_2S_2O_8$ electrolyte with various density was prepared by dissolving $K_2S_2O_8$ powder (molecular weight = 270.32 g mol^{-1}) in deionized water at room temperature, to prevent $SO4^{\cdot -}$ radicals from forming because of heat. The KOH based electrolyte was a 1:1 mixture containing 0.01 mol l^{-1} KOH electrolyte and 0.05 mol l^{-1} $K_2S_2O_8$ electrolyte. Likewise, the H_3PO_4 electrolyte was a 1:1 mixture containing 0.01 mol l^{-1} H_3PO_4 electrolyte and 0.05 mol l^{-1} $K_2S_2O_8$ electrolyte. As an UVC light source, we used an SK-BUVC-0860 (Shikoh Tech LLC) light source, which was a deep-UV flexible surface light with a luminous array film having a center wavelength λ of 260 nm and a FWHM of 55 nm. In order to measure the UVC light intensity, we used a UV intensity meter (Ushio, UIT-250) with a UVC detector (Ushio, UVD-S254).The pH value of the electrolyte was measured using a multi pH-meter, PC700 (Eutech Instruments). The transmittances of the electrolytes were measured using an ultraviolet and visible photometer UV-1700 (Shimadzu Corporation).

We used n-type GaN (n-GaN) epitaxial layers grown by metal organic vapor phase epitaxy on free-standing GaN (0001) substrates produced by a void-assisted separation method [38, 39]. The carrier concentration, thickness, and threading dislocation density of the n-GaN layers were 5 × 10^{16} cm^{-3}, 3 µm, and 3 × 10^{6} cm^{-2}, respectively. The sample size was 7 × $7mm^2$, which is much smaller than the illumination area of 80 × 60 mm^2. As mentioned above, I used a positive type photoresist film was utilized as an etching mask formed on the n-GaN sample surface. A Megaposit™ SPR6810 photoresist was spin-coated at 500 rpm for 3 s and 5000 rpm for 30 s to obtain a 950-nm-thick film on the n-GaN surface. After a photolithography process, the patterned sample was hard-baked in an oven at 110 °C for 10 min. The laser microscope images were obtained using a laser microscope OLS4500 (Olympus Co., LTd.). Etching depth and morphology were evaluated using a DEKTAK-150 (Bruker) surface profiler and an atomic force microscope (AFM) with an L-trace II (Hitachi High-Tech Science Corporation).

5.3. PH change under UVC illumination and sulfate radicals production rate

In order to develop the H_3PO_4 based electrolyte containing $S_2O_8^{2-}$ ions for CL-PEC etching, I discussed the behavior change of $S_2O_8^{2-}$ ions concerned with production rate of $SO4^{\cdot -}$ radicals on the basis on the difference of basic electrolyte, which are KOH or H_3PO_4. Specifically, I measured the pH change of two electrolytes under UVC illumination and compared the results.

As mentioned in the introduction, a $S_2O_8^{2-}$ ion is decomposed two $SO_4^{\cdot -}$ radicals by absorbing UV light with a wavelength below 310 nm*). A $SO_4^{\cdot -}$ radical has very strong oxidizablity, cause an oxidizing reaction at the moment and change into a sulfate (SO_4^{2-}) ion. In the CL-PEC etching of GaN, the whole anodizing and dissolution reaction of GaN involving $SO_4^{\cdot -}$ radicals is represented as:

$$\mathrm{GaN} + \mathrm{photo\ carriers}\ (3h^{+} + 3e^{-}) + 3SO_4{}^{\cdot -} \rightarrow Ga^{3+} + 3SO_4{}^{2-} + \frac{1}{2}N_2, \quad (1)$$

where the description of intermediate products (such Ga_2O_3) is omitted for simplification. As described in the reaction (1), the photo-generated holes are used for the oxidation of the GaN surface and the electrons are consumed for the reduction of the $SO_4^{\cdot -}$ radicals. The $SO_4^{\cdot -}$ radicals play an important role as a cathode to collect the electrons with the strong oxidizability and the anodization on the GaN surface can progress without the contact to an external circuit in the CL-PEC etching. Therefore, the production rate of $SO_4^{\cdot-}$ radicals under UV illumination is a key parameter to determine the etching rate.

On the other hand, $SO_4^{\cdot-}$ radicals relate not only to collect the electrons on the GaN surface but also to oxidize water molecules in the electrolyte. The oxidization of water is represented as:

$$SO_4^{\cdot-} + \frac{1}{2}H_2O \rightarrow SO_4^{2-} + H^+ + \frac{1}{2}O_2. \quad (2)$$

Most of $SO_4^{\cdot-}$ radicals are used for the oxidation of water everywhere in the electrolyte rather than oxidization on the GaN surface at the total consumption. If the oxidization reaction occurs, pH of the electrolyte decreases. In other words, pH change in the electrolyte containing $S_2O_8^{2-}$ ions over time under UV illumination indicates the production rate of $SO_4^{\cdot-}$ radicals.

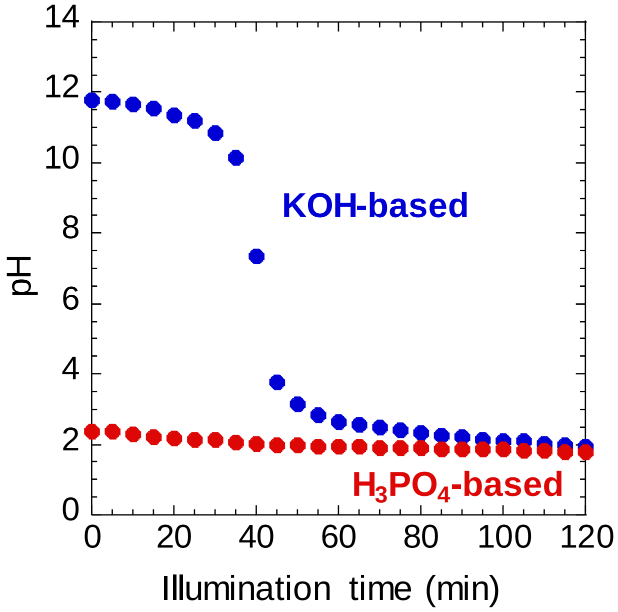

Figure 5.1. PH change for every 5 min in the KOH and H_3PO_4 based electrolytes containing $S_2O_8^{2-}$ ions under the UV illumination. The blue circles were the pH in the KOH based electrolytes and the red circles were the pH in the H_3PO_4 based electrolytes.

Figure 5.1 shows pH change for every 5 min in the KOH and H_3PO_4 based electrolytes containing $S_2O_8^{2-}$ ions under the UVC illumination in this experiment.
During the measurement, the electrolytes were not stirred. The initial pH value in the KOH based electrolyte was 11.79 in an alkaline region, which was a mixture the strong alkali, KOH, and the weak acid $S_2O_8^{2-}$. However, the pH value had been decreased over time under the UVC illumination, reached an acid region at 45 min and continued to decrease after that. Eventually, the pH value was 1.96 at 120 min. In contrast, the initial pH value in the H_3PO_4 based electrolytes was 2.37 in an acid region, which was a mixture the weak acid, H_3PO_4, and the weak acid $S_2O_8^{2-}$. The pH value had been gradually decreased over time under the UVC illumination and was 1.79 at 120 min. In this connection, although the pH value decrease obtained under the UVC illumination, under UVA illumination with the wavelength of 360 nm, the pH value had been constant over time.

As shown in the reaction (2), the oxidization of a water molecule by two $SO_4^{\cdot-}$ radicals produce two hydrogen (H^+) ions. After the oxidization, the pH value decreases as the density of H^+ ions increases. Therefore, the pH decrease under the UVC illumination can be regard as neutralization titration of KOH based electrolyte with $SO_4^{\cdot-}$ radicals. The pH value before and after the neutralization point arrival are respectively represented as:

$$\mathrm{pH} = -\log_{10}\left(\frac{1.0\times10^{-14}}{[OH^-]_i - x\cdot t}\right) \text{ for pH } \geq 7 \quad \text{(3a)}$$

and

$$\mathrm{pH} = -\log_{10}\left(x\cdot(t - t_n)\right) \text{ for pH} < 7, \quad \text{(3b)}$$

where $[OH^-]_i$ is the initial density of hydroxide (OH^-) ions, x is the production rate of the H^+ ions, t is the UVC illumination time and t_n is the time it takes for arrival at the neutralization point with pH = 7.0.

The above two equations (3a) and (3b) were used to calculate the production rate of H^+ ions in the experiment from the pH change of each electrolytes at each time. In the KOH-based electrolyte, the initial concentration of hydroxide ions [OH-] was 6.17×10^{-3} mol/L, from a pH value of 11.79 at t = 0. Next, t_n was extrapolated against the previous plot of pH change to obtain t_n = 40 min. At this time, the H^+ ion production rate x did not change in either the alkaline or acidic regions, and was 1.54×10^{-4} mol/L. It was also constant regardless of time.

In order to confirm the fact that the production rate of H^+ ion was independent of pH, I also calculated the pH change of H_3PO_4-based electrolyte, which could be calculated simply by the following equation, since the pH of H_3PO_4-based electrolyte was always in the acidic region.

$$\mathrm{pH} = -\log_{10}([H^+]_i + x \cdot t)\ for\ pH < 7, \ (4)$$

where $[H^+]_i$ is the initial density of H^+ ions. The $[H^+]_i$ was calculated of 4.07×10^{-3} mol l^{-1} with the initial pH value of 2.37. Using the above equation, the production rate of H^+ ions in the H_3PO_4 electrolyte was found to be 1.54×10^{-4} mol/L, the rate similar to that of the KOH-based electrolyte. In other words, it was reconfirmed that the production rate of H^+ ions was independent of pH. This increase in H^+ ions (and decrease in OH^- ions) was due to the oxidation of $SO_4^{\cdot-}$ radicals. The result that the production rate of H^+ ions is constant regardless of pH and time suggests that the production rate of $SO_4^{\cdot-}$ radicals, which is very important in etching, is also constant regardless of pH and time.

5.4. Transmittance measurement and determination of CL-PEC etching setup for GaN

A $S_2O_8^{2-}$ ion generates two $SO_4^{\cdot-}$ radicals by photodecomposition with absorption of UV light with the wavelength of below 310 nm. On the other hand, anodization on the GaN surface is caused with holes supplied by the photo-absorption with the wavelength of below 365 nm in an electrolyte. In other words, the UV light with the wavelength of below 310 nm can generate $SO_4^{\cdot-}$ radicals and supply holes on the GaN surface at the same time, and it can simplify the setup of CL-PEC etching for GaN. In this case, the balance of the absorption amount of the UV light in the electrolyte and on the GaN surface is an important factor for the etching characteristics, for example, the etching rate or the surface morphology after the etching. The absorption amount in the electrolyte and on the GaN surface can be determined with the density of the electrolyte and the distance from the GaN surface to the electrolyte surface, respectively. In order to determine the amount and the setup for CL-PEC of GaN is described later, I measured transmittances of $K_2S_2O_8$ electrolytes with the various $K_2S_2O_8$ density. Figure 5.2 shows the transmittance of the various $K_2S_2O_8$ electrolytes in the range from 0.01 mol l-1 to 0.1 mol l^{-1} corresponding with the each wavelength.

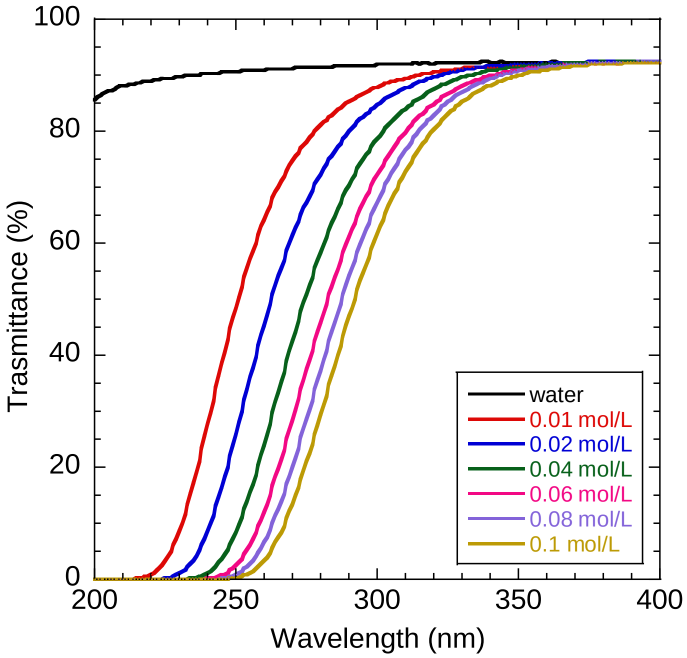

Fig. 5.2. Transmittance of K2S2O8 electrolytes at various density: 0 (water), 0.01, 0.02, 0.04, 0.06, 0.08, and 0.10 mol l^{-1}.

In the experiment, a 1 cm path cell length was used. As shown in Fig. 5.2, the transmittances of the $K_2S_2O_8$ electrolytes decreased as the wavelength increased or the density increased.

The absorption coefficients of the $K_2S_2O_8$ electrolytes to the each wavelength can be calculated by Lambert's Law shown as:

$$I = I_0 e^{-\alpha x}, \quad (5)$$

where I_0 is the light intensity before incidence, α is the absorption coefficient of the electrolyte, x is the optical pass length and I is the light intensity after passing x. In addition, the absorption amount of the electrolyte can be determined by the above relation.

5.5. CL-PEC etching for GaN

In the section 6.2, the pH in the KOH based electrolyte under the UVC illumination was found to change from alkaline region to acid region over a neutralization point as time passed. The pH instability could adversely affect the etching of GaN, because Ga_2O_3 is insolubility in the electrolyte containing pH of around 7.0. In addition, the production rate of $SO_4^{\cdot -}$ radicals under the UVC illumination were independent of the electrolyte. Therefore, in this experiment, I conducted the CL-PEC etching for GaN in the H_3PO_4 based electrolyte and discussed the results from the viewpoint of the etching rate and the surface roughness comparing with the results in the KOH based electrolyte.

Fig. 5.3 shows the setup of the CL-PEC etching in this experiment.

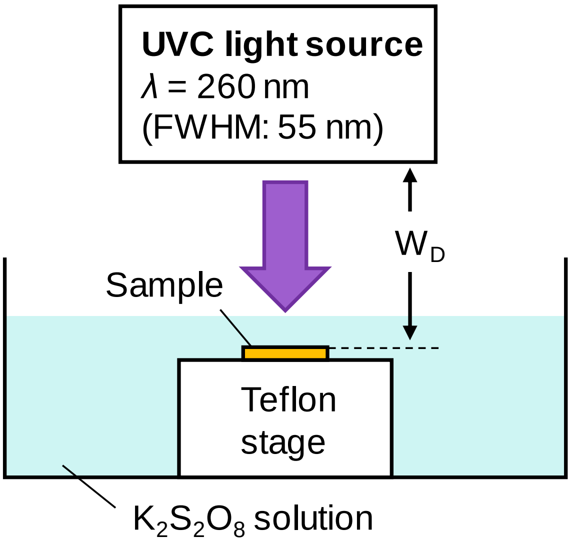

Fig. 5.3. Experimental setup used in this experiment.

The H_3PO_4 based electrolyte was used in this experimental was a mixture containing 0.01 mol l^{-1} H_3PO_4 electrolyte and 0.05 mol l^{-1} $K_2S_2O_8$ electrolyte as the same in section 6.2. In addition, the distance from the GaN surface to the electrolyte surface was determined of 0.5 cm. Under the $K_2S_2O_8$ density and the distance, a proportion of the photo absorption amount in the electrolyte and the arrival amount on the GaN surface was 50 % and 50 %, when the UVC light with a wavelength of 260 nm, which was the center wavelength of the used light source in this experiment, was irradiated in parallel with the GaN surface in the electrolte. The intensity of the illuminated UVC light was determined of 4.0 mW cm^{-2} with a working distance (W_D) of 4 cm, which was the distance from the GaN surface to the UVC light source.

The Fig. 5.4 shows the n-GaN sample structure used in this experiment.

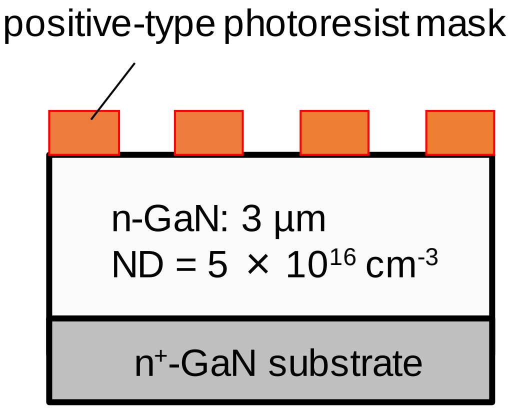

Fig. 5.4. The n-GaN sample structure used in this experimental.

The doping density (N_D) of the n-GaN sample was 5× 10^{16} cm^{-3}. In addition, a positive type photoresist film was directly used as the etching mask after the photolithography, which was the advantage of the H_3PO_4 based electrolyte compared with the KOH based electrolyte.

After the CL-PEC etching of GaN, I initially discussed the durability of the photoresist mask. Figures 5.5 (a) and (b) show the laser microscope images on the sample surface before and after the etching for 105 min.

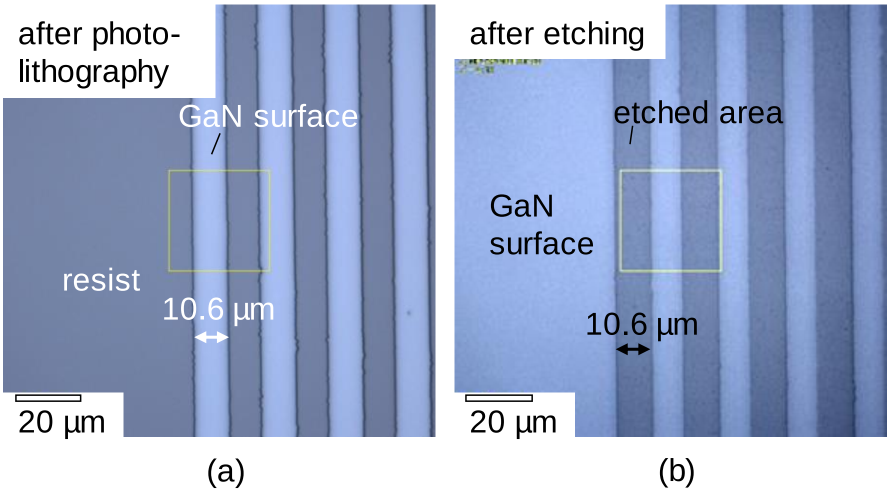

Fig. 5.5. The laser microscope images on the sample surface with the patterned-photoresist mask (a) before and (b) after the etching.

The pattern of the photoresist mask was the line-and-space pattern with the line width of 10.6 μm. For the figures 5.5 (a) and (b), the (a) was the image with the photoresist mask and the (b) was the image without the photoresist mask on the sample surface. The appearance change of the photoresist mask didn't observed and the line width of 10 μm was equal as shown in the Fig. 5.5 before and after the etching. The results indicate that the positive type photoresist film has the sufficient durability to the acid electrolyte and a function as an etching mask in the CL-PEC etching and the employment of the photoresist film can simplify the etching process for the application to the GaN device process.

Figure 5.6 shows the correlation between the etching depth and the etching time.

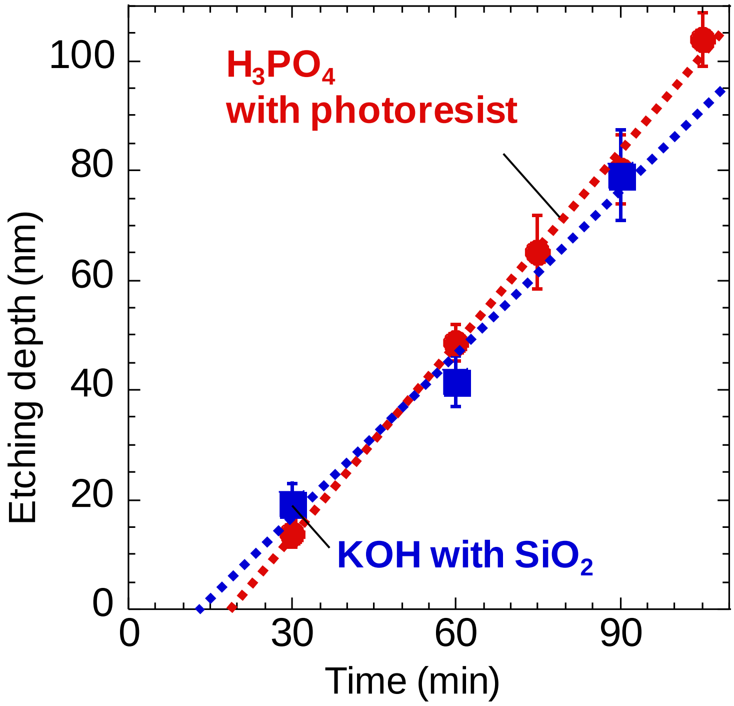

Fig. 5.6. The correlation between the etching depth and the etching time. The red circles was the results in the H3PO4 based electrolyte and the blue squares was the reported in the KOH based electrolyte [35)].

The red circles and the red broken line was the correlation in the H_3PO_4 based electrolyte in this experiment, and the blue squares and the blue broken line was the reported correlation in KOH based electrolyte[35)]. In this connection, the conditions involved in incident light intensity, the UVC source and the contained density of $K_2S_2O_8$ except for the kind of base electrolyte was almost the same in this experiment and the report. As shown in the Fig 5.6, the etching depth linearly increased to the etching time over the initial incubation period. The origin of incubation period has not been clarified yet. The similar behaviors have been reported for both dry- and wet-etching of semiconductors, where the residual contamination and formation natural oxide film are sited as possible causes. The etching rate in the H_3PO_4 based electrolyte was about 1.17 nm min^{-1}, which was equivalent to the reported etching rate of 1.0 nm min^{-1} in the KOH based electrolyte. The equality must be resulting from the independence of the $SO_4^{\cdot-}$ radical production rate on the pH in the electrolyte as found in the section 5.2.

Figures 5.7 (a) and (b) show the AFM images on the sample surface after the etching for 30 min and 60 min, respectively.

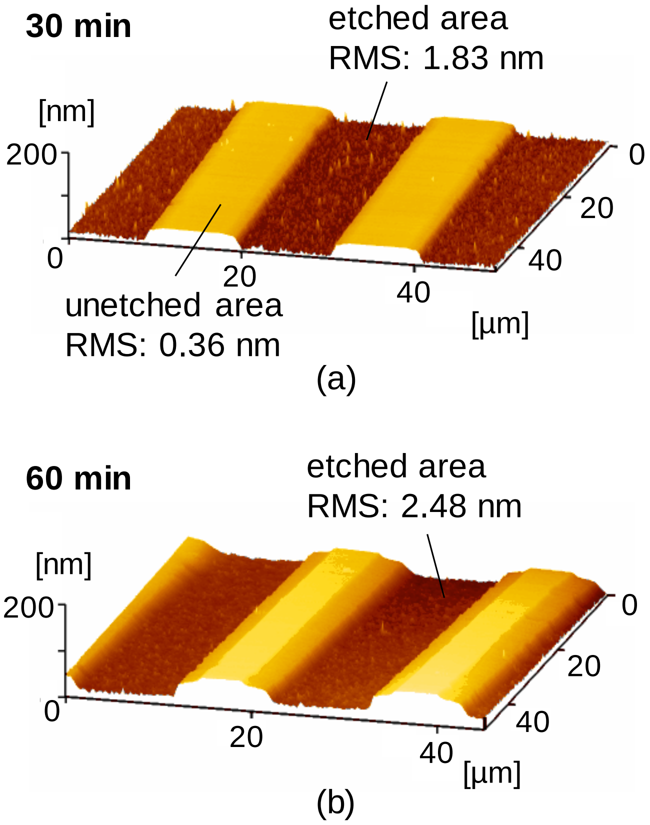

Fig. 5.7. The AFM images on the sample surface after etching for (a) 30 min and (b) 60 min in this experiment.

The roughness on the etched surface was 1.83 and 2.48 nm (root mean square: RMS), as determined from the AFM observation in the 7 × 7 μm^2 area, which was comparable to the above reported results in KOH based electrolyte). While sharp corners were observed at the boundary between the etched and unetched surface after the etching for 30 min, the round corners were observed at the boundary after the etching for 60 min as shown in Fig. 5.7 (a) and (b). The results should be due to the poor adhesion of the photoresist mask to the GaN surface and the associated undercut, which is expected to be cancelled by the optimization of a film-coating process.

5.6. Conclusion

In this chapter, I conducted the development of the new $K_2S_2O_8$ containing electrolyte, the transmittance measurement of the $K_2S_2O_8$ electrolyte, the CL-PEC etching of n-GaN with the photoresist film as the etching mask and discussed the characteristics. Through the measurement of the pH change in the both KOH and H_3PO_4 electrolytes containing $S_2O_8^{2-}$ ions under UVC illumination and the analysis of the results, the production rate of the $SO_4^{\cdot -}$ radicals by photodecomposition of $S_2O_8^{2-}$ ions was found to be independent on the pH in the electrolyte. Through the measurement of the transmittance of UVC light in the $K_2S_2O_8$ electrolytes with various concentration, the transmittance was found to decrease as the concentration increased. In addition, the balance of the photo absorption amount in the electrolyte and the incident light intensity on the GaN surface was established in the CL-PEC etching of n-GaN by the $K_2S_2O_8$ concentration of the electrolyte and the distance from the GaN surface to the electrolyte surface determined in consideration for the absorption coefficients calculated by Lambert’s Law. Eventually, I conducted the CL-PEC etching of n-GaN with a photoresist film as an etching mask in the developed H_3PO_4 based electrolyte. I found that the photoresist mask had sufficient durability to the electrolyte, and the etching rate and the surface morphology on the sample surface after the etching were equivalent to the reported ones. These results indicate that the CL-PEC etching in the acid electrolyte is promising for application to the fabrication process of GaN devices.

Reference

[1] J. I. Pankove, and J. E. Berkeyheiser, Proc. IEEE 60, 1456 (1972).

[2] S. Nakamura, T. Mukai, and M. Senoh, Appl. Phys. Lett. 64, 1687 (1994).

[3] S. Nakamura, M. Senoh, S. Nagahama, N. Iwasa, T. Yamada, T. Matsushita, H. Kiyoku, and Y. Sugimoto, Jpn. J. Appl. Phys. 35, L74 (1996).

[4] S. Nakamura, M. Senoh, S. Nagahama, N. Iwasa, T. Yamada, T. Matsushita, Y. Sugimoto, and H. Kiyoku, Appl. Phys. Lett. 69, 4056 (1996).

[5] B. J. Baliga, IEEE Electron Device Lett. 10, 455 (1989).

[6] U. K. Mishra, L. Shen, T. E. Kazior, and Y. F. Wu, Proc. IEEE 96, 287 (2008).

[7] T. Kachi, Jpn. J. Appl. Phys., 53, 100210 (2014).

[8] S. J. Pearton, J. C. Zolper, R. J. Shul, and F. Ren, J.Appl.Phys. 86, 1 (1999).

[9] X. A. Cao, H. Cho, S. J. Pearton, G. T. Dang, A. P. Zhang, F. Ren, R. J. Shur, L. Zhang, R. Hickman, and J. M. V. Hove, Appl. Phys. Lett. 75, 232 (1999).

[10] T. Hashizume, and R. Nakasaki, Appl. Phys. Lett. 80, 4564 (2002).

[11] Z. Mouffak, A. Bensaoula, and L. Trombetta, J. Appl. Phys. 2, 727 (2004).

[12] Z. Yatabe, J. T. Asubar, and T. Hashizume, J. Phys. D: Appl. Phys. 49, 393001 (2016).

[13] M. S. Minsky, M. White, and E. L. Hu, Appl. Phys. Lett. 68, 1531 (1996).

[14] C. Youtsey, I. Adesida, L. T. Romano, and G. Bulman, Appl. Phys. Lett. 72, 560 (1998).

[15] L. H. Peng, C. W. Chuang, J. K. Ho, C. N. Huang, and C. Y. Chen, Appl. Phys. Lett. 72, 939 (1998).

[16] I. M. Huygens, K. Strubbe, and E. P. Gomes, J. Electrochem. Soc. 147, 1797 (2000).

[17] T. Rotter, D. Mistele, J. Stemmer, F. Fedler, J. Aderhold, J. Graul, V. Schwegler, C.

Kirchner, M. Kamp, and M. Heuken, Appl. Phys. Lett. 76, 3923 (2000).

[18] C. H. Ko, Y. K. Su, S. J. Chang, W. H. Lan, J. Webb, M. C. Tu, and Y. T. Cherng, Mater. Sci. Eng. B 96, 43 (2002).

[19] F. Horikiri, Y. Narita, and T. Yoshida, Jpn. J. Appl. Phys. 57, 086502 (2018).

[20] S. Matsumoto, M. Toguchi, K. Takeda, T. Narita, T. Kachi, and T. Sato, Jpn. J. Appl. Phys. 57, 121001 (2018).

[21] F. Horiki, H. Ohta, N. Asai, Y. Narita, T. Yoshida, and T. Mishima, Appl. Phys. Express 11, 091001 (2018).

[22] N. Asai, H. Ohta, F. Horikiri, Y. Narita, T. Yoshida, and T. Mishima, Jpn. J. Appl. Phys. 58, SCCD05 (2019).

[23] N. Harada, Y. Hori, N. Azumaishi, K. Ohi, and T. Hashizume, Appl. Phys. Express 4, 021002 (2011).

[24] Z. Zhang, S. Qin, K. Fu, G. Yu, W. Li, X. Zhang, S. Sun, L. Song, S. Li, R. Hao, Y. Fan, Q. Sun, G. Pan, Y. Cai, and B. Zhang, Appl. Phys. Express 9, 084102 (2016).

[25] Y. Kumazaki, K. Uemura, T. Sato, and T. Hashizume, J. Appl. Phys. 121, 184501 (2017).

[26] J. A. Bardwell, I. G. Foulds, J. B. Webb, H. Tang, J. Fraser, S. Moisa and S. J. Rolfe, J. Electron. Mater. 28, L24 (1999).

[27] H. Masher, D. W. DiSant, M. W. Dvorak, G. Soerensen, C. R. Bolognesi, J. A. Bardwell, H. Tang, and J. B. Webb, Electron. Lett. 36, 1969 (2000).

[28] H. Maher, D. W. DiSanto, G. Soerensen, and C. R. Bolognesi, Appl. Phys. Lett. 77, 3833 (2000).

[29] J. A. Bardwell, J. B. Webb, H. Tang, J. Fraser, and S. Moisa, J. Appl. Phys. 89, 4142 (2001).

[30] Z. H. Hwang, J. M. Hwang, H. L. Hwang, and W. H. Hung, Appl. Phys. Lett. 84, 3759 (2004).

[31] R. T. Green, W. S. Tan, P. A. Houston, T. Wang, and P. J. Parbrook, J. Electron.

Mater. 36, 397 (2007).

[32] D. H. van Dorp, J. L. Weyher, M. R. Kooijman, and J. J. Kelly, J. Electrochem. Soc. 156, D371 (2009).

[33] J. L. Weyher, F. D. Tichelaar, D. H. van Dorp, J. J. Kelly, and A. Khachapuridze, J. Cryst. Growth 312, 2607 (2010).

[34] S. Lee, S. Mishkat-Ul-Masabih, J. T. Leonard, D. F. Feezell, D. A. Cohen, J. S. Speck, S. Nakamura, and S. P. DenBaars, Appl. Phys. Express 10, 011001 (2017)

[35] F. Horikiri, N. Fukuhara, H. Ohta, N. Asai, Y. Narita, T. Yoshida, T. Mishima, M. Toguchi, K. Miwa, and T. Sato, Appl. Phys. Express 12, 031003 (2019).

[36] R. P. Buck, S. Singhadeja, and L. B. Rogers, Anal. Chem. 26, 1240 (1954).

[37] L. Dogliotti, and E. Hayon, J. Phys. Chem. 71, 2511 (1967).

[38] Y. Oshima, T. Eri, M. Shibata, H. Sunakawa, K. Kobayashi, T. Ichihashi, and A. Usui, Jpn. J. Appl. Phys. 42, L1 (2003).

[39] T. Yoshida, Y. Oshima, T. Eri, K. Ikeda, S. Yamamoto, K. Watanabe, M. Shibata, and T. Mishima, J. Cryst. Growth 310, 5 (2008).

Chapter 6

Fabrication of Recessed-gate structure with highly uniformity by CL-PEC etching

6.1. Introduction

AlGaN/GaN high electron mobility transistors (HEMTs) is expected for the next generation power switching devices due to the excellent electrical properties 1-4), which are high breakdown voltage, high saturation mobility, and high electron mobility and low on-state resistance utilizing 2-dimensional electron gases (2DEG) accumulating at the AlGaN/GaN interface. Common HEMTs shows the normally-on operation due to the 2DEG, however, the normally-off operation is favorable in the practical case on the viewpoint of power conservation and fail-safe. Recessed-gate structure is an attractive method to achieve the normally-off operation due to the simple way of shift the threshold voltage towards in the positive direction which is thinning the AlGaN layer just under the gate electrode, which leads to the depletion of 2DEG 5-8). For the nitride semiconductor devices, the recessed-gate structure have been fabricated by dry etching technique as Inductive Coupled Plasma Reactive Ion Etching (ICP-RIE) 5-7). However, this method induces damages on the semiconductor surface through the bombardment of reactive ions and radicals, which degrade device performance such as large leakage currents, current collapse and V_{th} instability 9-13). In addition, it is difficult for the dry etching method to control precisely the residual AlGaN thickness owing to the etching amount control by time 14).

Our group have discussed the photo-electrochemical (PEC) etching 15-28) as the low-damage etching process for the nitride semiconductor devices. The PEC etching progresses the cycle of the anodization on the semiconductor surface caused by supply of holes by photo-excitation surface and the dissolution of the oxide in the electrolyte. The (1) anodizing and (2) dissolution reaction of GaN are represented as:

$$2\mathrm{GaN} + 6OH^- + 6h^+(holes) \rightarrow Ga_2O_3 + 3H_2O + N_2 \;\cdots\; (1),$$
$$Ga_2O_3 + 6OH^- \rightarrow 2Ga_2O_3{}^{3-} + 3H_2O \;\cdots\; (2),$$

representively. The method has the characteristics of low-damage due to the natural chemical reaction, highly controllable of etching amount following "*Faraday's low*" and applicable to the semiconductor material with highly durability of the chemical etchants such as the nitride semiconductor [21-24]. There are many reports of the application of PEC etching to the nitride semiconductor device process such as smooth etching, removal of the surface damage after the dry etching, and fabrication of the trench structure and the recessed-gate structure on the AlGaN/GaN heterostructure [25-28].

Recently, contactless photo-electrochemical (CL-PEC) etching has appeared, which is the simplified PEC etching [29-42]. For the conventional PEC etching, the contact to the external circuit is required to collect the electrons generated by photo-excitation on the semiconductor surface. However, the sealing process of the contact point to the electrolyte is required in the PEC etching process, which is make the method difficult to apply the practical device process. On the other hand, for the CL-PEC etching, the electrons is directly consumed by the strong oxidizer, which the sulfate radical ($SO4^{\cdot -}$) is typically used as, in the electrolyte through the cathode pad on the semiconductor surface. Therefore, the above sealing process, which is inappropriate process to the practical device process, can be omitted in PEC etching. The $SO4^{\cdot -}$ radicals have strong oxidizability more than the hydrogen peroxide (H_2O_2) and can be generated by photodecomposition of the peroxodisulfuric ($S_2O_8^{2-}$) ions with UV light with the wavelength of below 310 nm. The simple setup of CL-PEC etching is shown in Fig. 1.

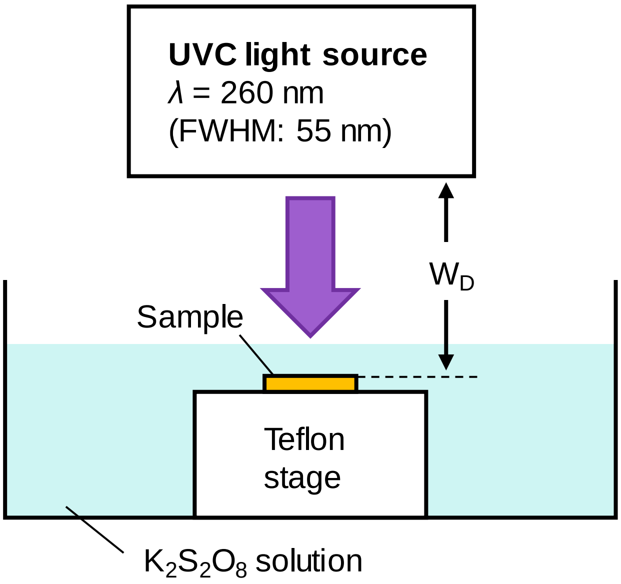

Fig. 6.1 Setup of CL-PEC etching in this experiment

The CL-PEC etching process only progresses under the UVC illumination to the sample in the electrolyte containing $S_2O_8^{2-}$ ions. Our group reported that the flatness on the etched surface equivalent to the flatness after the PEC etching was observed for

22+the CL-PEC etching of GaN [39-40]. In addition, the self-termination phenomenon is observed for the CL-PEC etching of AlGaN/GaN heterostructure. The phenomenon is that the etching rate becomes almost 0 when the residual AlGaN layer reaches the specific thickness and the etching don't progresses anymore. After the phenomenon, the residual AlGaN thickness has highly uniformity on the entire etched surface. We believed that the feature is prospective to fabricate recessed-gate structure with highly uniformity on the AlGaN/GaN heterostructure.

In this chapter, I investigated how the CL-PEC etching affects the electrical characteristics of Schottky diodes, metal-insulator-semiconductor (MIS) capacitors, and recessed-gate HEMTs fabricated on the etched surface of AlGaN/GaN heterostructures. After evaluation on the surface morphology on the etched surface, current-voltage (I-V) and capacitance-voltage (C-V) measurements were conducted on Schottky diodes and MIS capacitor. Then, the I-V characteristics of recessed-gate HEMTs were compared with those of planar-gate HEMTs fabricated on the same chip. From measurements made on multiple devices, the effect of CL-PEC etching on the uniformity of device characteristics is discussed.

6.2. Experimental details

The setup of the CL-PEC etching and the sample in this experiment shown are in Figs. 1 and 2, respectively.

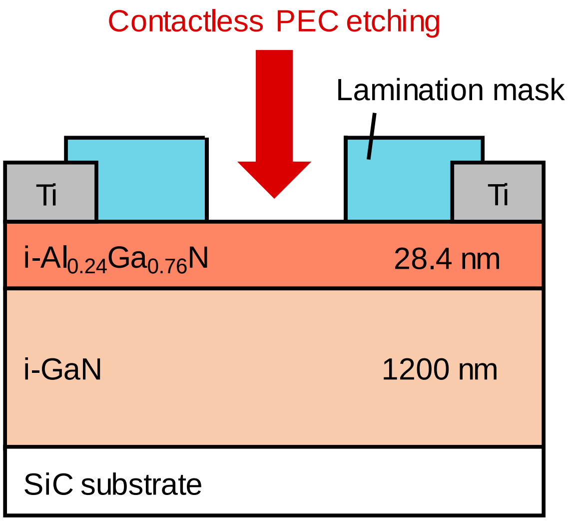

Fig. 6.2. Sample Structure

As the sample, an i-$Al_{0.24}Ga_{0.76}N$/i-GaN heterostructure grown on a SiC substrate with an AlN nuclear layer was used. Initial thickness of AlGaN layer and GaN layer were 28.4 nm and 1.2 µm. As the cathode pad for CL-PEC etching, Ti Pads of 100 nm were fabricated on the edge of the sample surface by electron-beam evaporation. The detail explanation was described in the past report 41). We conducted the CL-PEC etching by dipping the sample into a 0.025 mol L^{-1} $K_2S_2O_8$ electrolyte (pH = 3.4). The electrolyte was prepared by dissolving $K_2S_2O_8$ powder (molecular weight = 270.32 g mol^{-1}) into de-ionized water. SiN film (25 nm) was formed by sputtering and lithography to determine the etching region. Furthermore, the photoresist on the SiN film was remained after the patterning by lithography. In other words, a shade lamination layer of photoresist/SiN was used as an etching mask. The endurance of photoresist film to an acid electrolyte was explained in the chapter 6. The sample in the electrolyte was exposed to UV light by using a deep-UV flexible surface light with a luminous array film (Shikoh Tech LLC) that had a center wavelength of 260 nm with a full width at half maximum (FWHM) of 55 nm. For the setup of CL-PEC etching, the distance from the semiconductor surface to the light source (W_D) and the distance from the surface to the water surface were set to 30 mm and 5mm by a Teflon stage. The light intensity was measured of 4 mW/cm^2 in the atmosphere 40-42).

After the CL-PEC etching, the etching depth and the roughness on the etched surface were evaluated by atomic force microscope (AFM) and laser microscope. In addition, to improve surface morphology, a post-treatment with a 25wt. % solution of tetramethyl-ammonium hydroxide (TMAH) was conducted at 60 °C for 10 min. After the device isolation was conducted by ICP-RIE, Ti/Al/Ti/Au (20/50/20/50 nm) source and drain electrodes were deposited onto the AlGaN surface. Ohmic annealing was conducted at 830 °C for 1 min in an N_2 ambient with a SiN (25 nm) protection film. After removal of the SiN film, a Schottky-gate electrode was fabricated by electron-beam evaporation of the Ni/Au (20/50 nm) bilayer and the subsequent lift-off process. The gate length, gate-drain distance, gate-source distance, and gate width were 10, 10, 10, and 100 µm, respectively.

For the fabrication of the metal-insulator-semiconductor (MIS) gate structure, a 30-nm-thick Al_2O_3 film was deposited onto the AlGaN surface by atomic layer deposition (ALD), where water vapor and trimethyl-ammonium were introduced into a reactor in alternate pulse forms. Post-deposition annealing was conducted at 400 °C in an N_2 ambient after the ALD process. After the formation of the gate electrode, post-metallization annealing (PMA) was conducted at 300 °C in an N_2 ambient to further improve both the Al_2O_3 film quality and Al_2O_3/AlGaN interface quality 43).

In this study, Schottky barrier diodes (SBDs), MIS capacitors, Schottky-gate

HEMTs and MIS-gate HEMTs were fabricated on the same chip. To clarify the effect of CL-PEC etching, the electrical properties of these devices were compared with those formed on an unetched AlGaN surface of the same chip. Current-voltage (*I*-*V*) and capacitance-voltage (*C*-*V*) characteristics were measured with a Keysight Technologies B1500A Semiconductor Device Analyzer.

6.3. Etching Depth and Surface Roughness Evaluation

AFM observation was conducted on the etched surfaces prepared with different etching times, t_e to evaluate the changes in surface morphology during the CL-PEC process. The images at each t_e are shown in Figs. 6.2 (a) ~ (c).

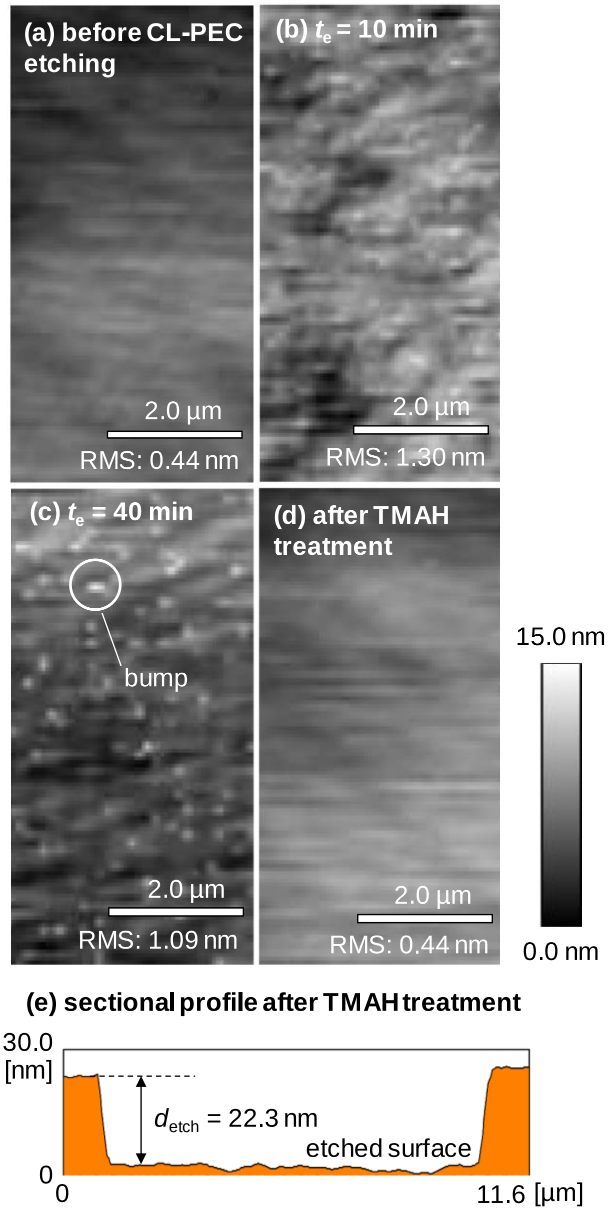

Fig. 6.3 AFM image of AlGaN surface: (a) before CL-PEC etching, (b) after CL-PEC eching for t_e = 10 min, (c) after CL-PEC etching for t_e = 40 min, and (d) after CL-PEC etching for t_e = 40 min with TMAH treatment. (e) Cross-sectional profile of etched and unethced region of sample shown in (d). RMS values were obtained by AFM measurements in 7×7 µm^2 area.

Atfter the CL-PEC etching at 10 min, average depth was 10.02 nm, the root-mean square (RMS) roughness was 1.30 nm in the 7×7 μm^2 on the etched surface, which was more than the one before the etching. At the 40 min, the average depth was 22.3 nm, where the residual AlGaN thicknes was calculated to be 6.1 nm from the initial AlGaN thickness was 28.4 nm and the etching rate was roughly estimated to be about 0.56 nm/min, and the RMS roughness was 1.09 nm in the 7×7 μm^2, which was improved from the roughness at the 10 min, however, small bumps appeared on the etched surface, as shown in Fig. 6.3 (c). As previously reported [39)], they originate from dislocation in the AlGaN/GaN epitaxial layer. In PEC etching, a portion of the dislocation was not etched due to the short lifetime of photo-carriers. To remove the bumps and improve the roughness on the etched surface, TMAH post-treatment was conducted at 60 °C for 10 min. Figs. 6.3 (d) and (e) show the AFM image and cross-sectional profile on the etched surface after the treatment, respectively. As a result, the difference of 22.3 nm wasn't change before and after the treatment and the bumps were removed after the treatment. The RMS roughness was decreased from 1.09 nm to 0.44 nm in the 7×7 μm^2 and the surface morphology was drastically improved, which was comparable to the unetched surface shown in Fig. 6.2 (a).

In addition, the etching of the AlGaN layer didn't proceed and difference didn't increase any further even if the t_e was set at 50 min or more. The phenomenon was observed in the wired PEC etching and previously reported as the self-termination by our group 27,. Briefly describing the model, the phenomenon occurs due to the stop of the oxidation on the semiconductor surface by the recombination of photo-carriers with the depletion of 2DEG density just under the thinned AlGaN layer. After the phenomenon, the residual AlGaN thickness was highly uniform on the entire etched area. I believe the self-termination phenomenon was prospective for the uniform and high-quality fabrication of the recessed-gate structure on the AlGaN/GaN HEMTs.

6.4. Electrical Characteristics of Schottky Barrier Diodes (SBDs) and MIS capacitor

Fig. 4 shows the $|I|$-V characteristics of SBDs and MIS-capacitors were fabricated on the etched surface by CL-PEC etching.

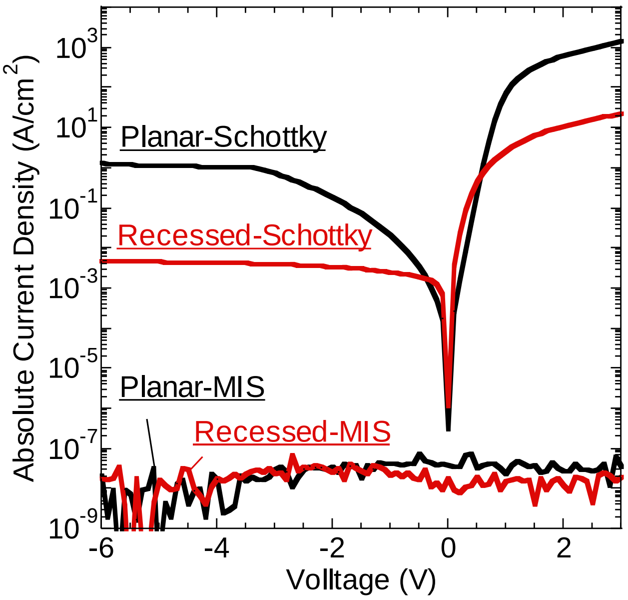

Fig. 6.4. Current-voltage characteristics of Schottky diodes and MIS capacitors fabricated on AlGaN/GaN heterostructures with and without CL-PEC etching.

For the planar SBDs on the nonetched surface, typical |*I*|-*V* characteristics was observed as the devices on the AlGaN/GaN heterostructure. The reverse currents increased with the reverse bias increase and showed the saturation tendency at -3.5 V. The result indicated that the 2DEG density decreased with reverse bias increase and depleted at -3.5 V. On the other hand, for the recessed SBDs on the etched surface, the reversed currents were less than the one of the planar devices and saturation voltage shifted near 0 V. It indicated that 2DEG was almost depleted at 0V and the devices could show normally-off operation on the etched surface. Fig. 4 also shows that the |*I*|-*V* characteristics of MIS-capacitors. For both planar and recessed devices, the reverse currents were almost not by MIS structure and the quality of Al_2O_3 insulator film was demonstrated.

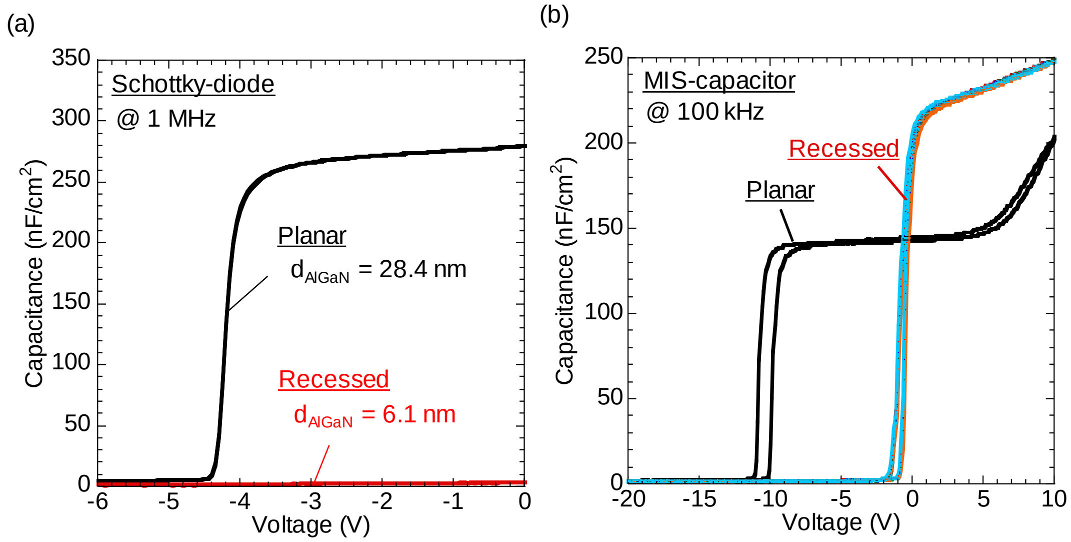

Fig. 6.5. Capacitance-voltage characteristics of (a) Schottky diodes and (b) MIS capaciors fabricated on AlGaN/GaN heterostructures. Five curves obtained for different devices are shown in same graph for recessed-MIS capacitors.

Figs. 6.5 (a) and (b) show the *C*-*V* characteristics of SBDs and MIS-capacitor. In Fig. 6.5 (a), for planar SBDs, the capacitance value was not observed below -4.4 V, increased above -3.5 V and saturated at -3.5 V. The capacitance at the saturated region occurred by behavior of AlGaN layer as a dielectric film between the Schottky electrode and GaN layer with 2DEG at AlGaN/GaN interface. Therefore, the capacitance value of the AlGaN layer per unit area C_{AlGaN} is described as the following equation:

$$\frac{1}{C_{AlGaN}} = \frac{d_{AlGaN}}{\varepsilon_0 \varepsilon_{AlGaN}}, \qquad (1)$$

where, d_{AlGaN} is the thickness of the AlGaN layer, ε_0 is the dielectric constant of vacuum and ε_{AlGaN} is the relative permittivity of AlGaN. With the equation, d_{AlGaN} was calculated as 29.23 nm, which was close to the designed value, where the C_{AlGaN} was 280.19 nF/cm^2 at 0 V and ε_{AlGaN} was 9.25. For the recessed devices, the capacitance value was not observed in the bias range from -6 V to 0 V. It results that the 2DEG depletion and normally-off operation for the recessed devices. In the bias range above 0 V, the capacitance couldn't be validly measured due to the leakage currents. I analyzed the *C*-*V* characteristics of planar devices to obtain the charge distribution in the depth direction from Schottky electrode/AlGaN interface to GaN bulk layer [44)]. The peak of the charge density was obtained at the AlGaN/GaN interface and the 2DEG density was calculated as 6.93×10^{12} cm^{-2}.

Fig. 6.5 (b) shows the *C-V* characteristics of MIS-capacitor. For the *C-V* curve of the planar MIS-capacitor, typical two-step was observed as a MIS capacitor fabricated on the AlGaN/GaN heterostructure 13). At a bias of less than -10 V, the capacitance could not be measured due to the depletion of 2DEG at the AlGaN/GaN interface. The capacitance value of the planar devices was obtained above -10 V, which indicated accumulation of electrons at the interface, and the combined capacitance of two dielectric films, that is, the AlGaN layer and the Al_2O_3 layer. The combined capacitance value C_S is described with the relational expression of combined capacitance for Al_2O_3 and AlGaN dielectric layers as:

$$\frac{1}{C_S} = \frac{1}{C_{AlGaN}} + \frac{1}{C_{Al_2O_3}} = \frac{d_{AlGan}}{\varepsilon_0 \varepsilon_{AlGaN}} + \frac{d_{Al_2O_3}}{\varepsilon_0 \varepsilon_{Al_2O_3}}, \quad (2)$$

where, C_{Al2O3} was the capacitance density, ε_{Al2O3} was relative permittivity and d_{Al2O3} was the thickness of the Al_2O_3 layer, respectively. By using the above equation, the d_{AlGaN} of the planar MIS-capacitor was calculated of 27. 1 nm with ε_{Al2O3} = 9.0, d_{Al2O3} = 29.3 nm measured by an ellipsometer, which was close to the designed value. Above 5 V, the capacitance increased again. It resulted that the electrons of 2DEG overcome the potential barrier of AlGaN layer and began to accumulate at the Al_2O_3/AlGaN interface. For the recessed devices, the rising voltage shifted near 0 V and the first step only observed. It should be resulted from that the first step integrated the second step as shown in the planar device's characteristics and the combined capacitance of Al_2O_3 and AlGaN layer exists after the first step can't be observed by the shift of first step near 0 V. The d_{AlGaN} of the recessed devices was calculated as 6.6 nm by using the above relation equation with the capacitance at 0 V. The thickness was very close to the residual AlGaN thickness of 6.1 nm measured by AFM. For the both recessed devices, the C-*V* curve analytics were conducted like the analytics of planar MIS devices. The strong charge distribution peaks were obtained at the AlGaN/GaN interface likewise planar MIS capacitor. The 2DEG density of planar and recessed devices was calculated of 8.01×10^{12} cm^{-2} and 4.90×10^{12} cm^{-2}, respectively. In addition, for the recessed devices, the *C-V* curves of five devices had highly uniformity on the same chip shown as Fig. 6.5 (b). The results should be due to the uniformity of d_{AlGaN} on the entire etched surface based on the self-termination phenomenon.

6.5. Electrical Characteristics of Schottky and MIS HEMTs

For the Schottky-HEMTs, the devices with the gate length of 10 µm and the distance from source electrode and drain electrode of 30 µm were fabricated and the characteristics was evaluated. The drain currents-drain voltage (I_D-V_D) characteristics of both planar Schottky HEMTs and recessed MIS HEMTs showed the good saturation characteristics and pinch-off characteristics shown as Fig. 6.6.

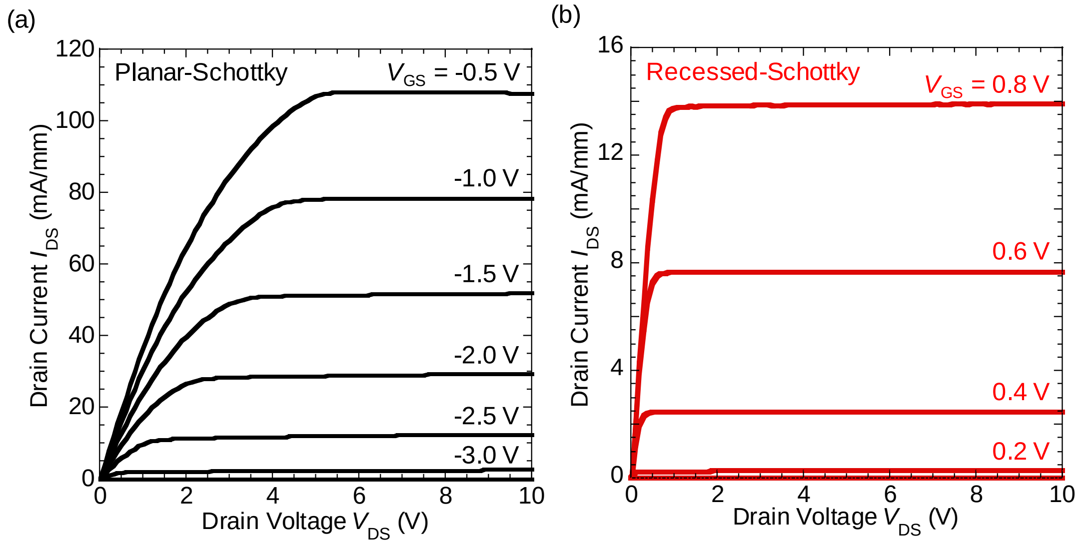

Fig. 6.6. Drain current-voltage characteristics of (a) planar-Schottky and (b) recessed-Schottky HEMTs with gate length of 10 µm and source-drain spacing of 30 µm.

Fig. 6.7 (a) showed the linear plots of the drain currents-gate voltage (I_D-V_G) characteristics and the trans-conductance (g_m) of the both devices in the saturation region (V_G = 10 V). The threshold voltage of the planar device and the recessed devices determined by the linear extrapolation method were -2.7 V and 0.4 V, respectively and the threshold voltage of recessed devices showed the positive shift. Fig. 6.7 (b) showed the semi plots of the [I_D|-V_G and the |I_G|-V_G characteristics. The drain leakage currents of the recessed devices were less than the ones of the planar devices and the Subthreshold Slope (SS) value of recessed devices was 130 mV/dec, which was less than the SS value of planar devices was 250 mV/dec. In addition, for the recessed Schottky devices, the nine characteristics of [I_D|-V_G on the same chip has highly uniformity at the positive bias. To evaluate the highly uniform quantitively, the variation of the threshold voltage of Schottky devices was evaluated. For the both recessed Schottky devices, to determine strictly the threshold voltage, the threshold voltage was determined not by the linear extrapolation but as the voltage at the drain currents of 10^{-4} A/mm. Figs. 6.8 showed the results..

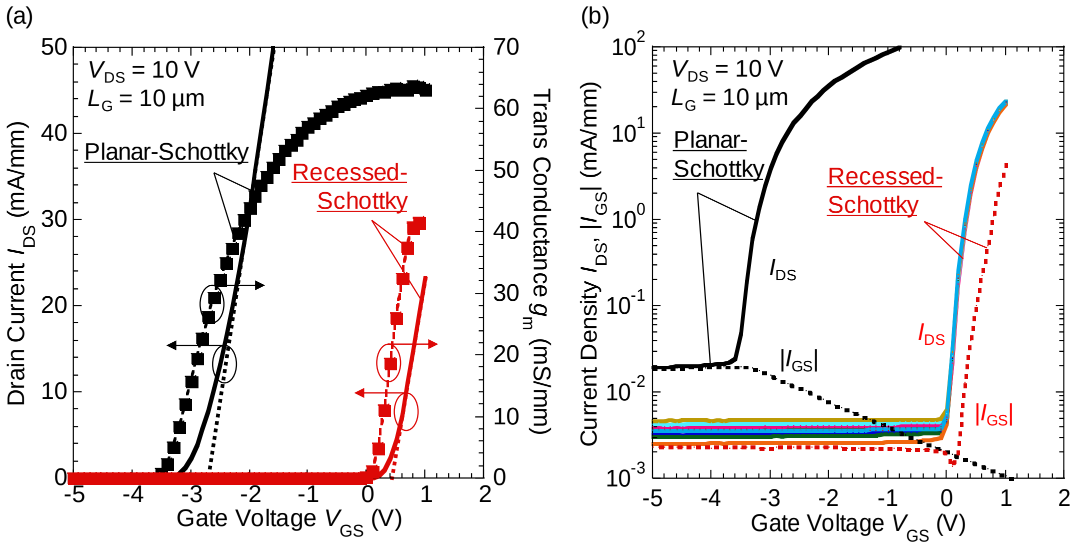

Fig.6.7. (a) Transfer characteristics of planar-Schottky and recessed-Schottky HEMTs in saturated region (V_{DS} = 10V); (b) Semi-log plots of I_{DS}-V_{GS} and $|I_{GS}|$-V_{GS} characteristics; Nine I_{DS}-V_{GS} curves obtained for different devices are shown in same graph for recessed-Schottky devices.

As a result, for the planar Schottky Devices, the average threshold voltage and the standard variation of the six devices were -3.39 V and 69.2 mV, respectively. In other hands, for the recessed Schottky devices, the average threshold voltage and the standard variation of the nine devices on the same chip were 0.14 V and 5.46 mV, respectively. The variation of threshold voltage of recessed Schottky devices was drastically improved. The uniformity should be due to the removal of the initial surface damage introduced by the sputtering method to deposit of the SiN film and the impurities by CL-PEC etching. In addition, the main factor should be the highly uniformity of the residual AlGaN thickness after the self-termination phenomenon as explained above. To confirm the improved variation visually, the Gaussian fitting was conducted with the obtained average threshold voltage and the standard deviation of the both Schotkky devices. The threshold voltage of recessed Schottky HEMTs had the strong peak in the narrow bias region compared with the broaden curves of planar Schottky HEMTs shown as Fig. 6.8.

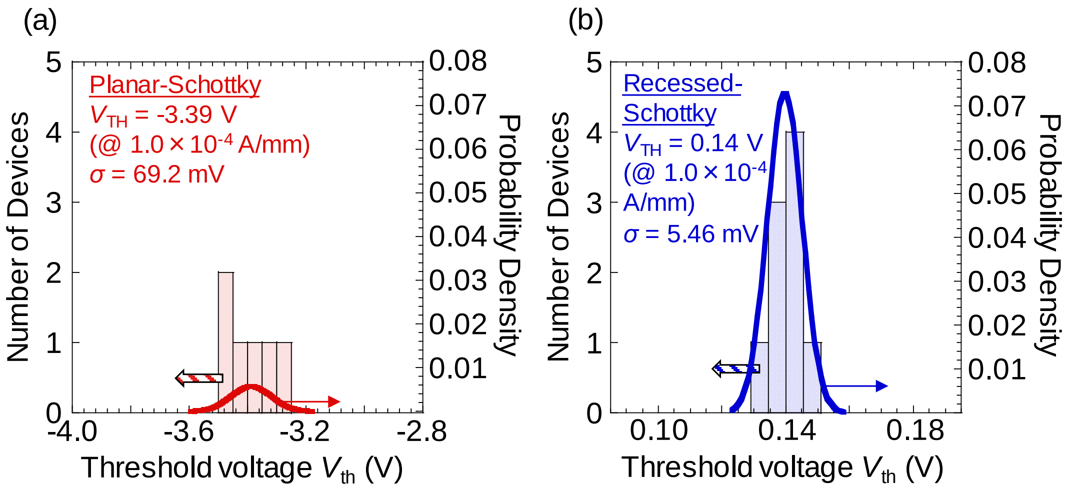

Fig. 6.8. Histograms of the threshold voltage V_{th} valued of ALGaN/GaN HEMTs for (a) six planar-Schottky devices, (b) nine recessed-Schottky devices.

Next, for the AlGaN/GaN MIS-HEMTs with the same gate length and the same distance between the source electrode and the gate electrode as the Schottky devices, the same evaluation was conducted. The I_D-V_D characteristics of the both MIS-HEMTs showed the good saturation characteristics and pinch-off characteristics shown as Fig. 6.9.

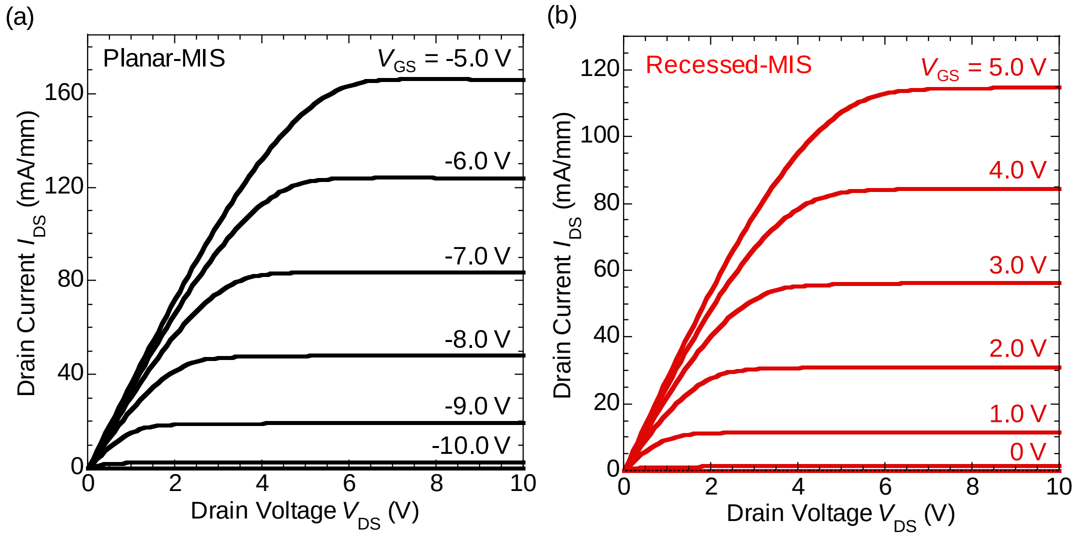

Fig. 6.9. Drain current-voltage characteristics of (a) planar-MIS and (b) recessed-MIS HEMTs with gate length of 10 μm and source-drain spacing of 30 μm.

In addition, for the recessed MIS devices, the MIS structure suppressed the gate leakage currents and enabled to apply higher gate voltage than the recessed Schottky devices. Fig. 6.10 (a) showed the linear plots of [I_D|-V_G characteristics and the g_m of both MIS devices in the saturation region (V_G = 10 V).

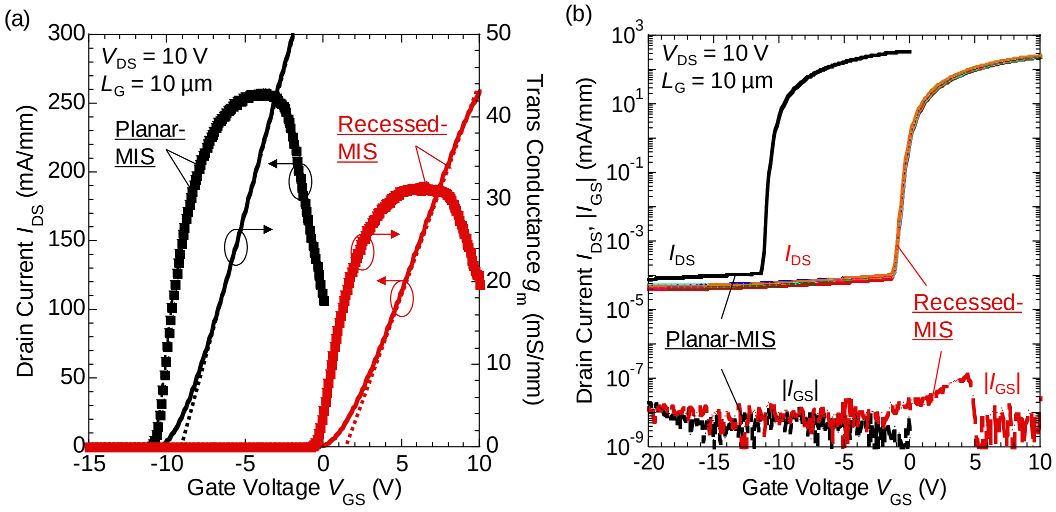

Fig. 6.10. (a) Transfer characteristics of planar-MIS and recessed-MIS HEMTs in saturated region (V_{DS} = 10 V). (b) Semi-log plots of I_{DS}-V_{GS} and |I_{GS}|-V_{GS} characteristics; Seven I_{DS}-V_{GS} curves obtained for different devices are shown in same graph for recessed-MIS devices.

The threshold voltage of the planar MIS devices and the recessed MIS devices determined by the linear extrapolation method were -9.0 V and 0.2 V, respectively. The threshold voltage of the recessed devices shifted into the positive direction. The g_m of recessed devices was less than the one of planar devices. The result should be the accumulation of electrons at the Al_2O_3/AlGaN interface by overcoming the AlGaN barrier layer and the measurements containing the currents by the parallel conduction in the drive voltage range of recessed devices. Fig. 6.10 (b) showed the semi-log plots of the [I_D|-V_G and the |I_G|-V_G characteristics. The leakage currents of the recessed devices were less than the planar devices and the SS value of the both devices was 150 mV/dec. In addition, for the recessed devices, the variation of I_D-V_G characteristics of the seven devices on the same chip had highly uniformity in the positive bias region. To evaluate the uniformity quantitively, the variation of the threshold voltage was evaluated like the evaluation of the Schottky devices. For the both recessed MIS devices, to determine strictly the threshold voltage, the threshold voltage was determined not by the linear extrapolation but as the voltage at the drain currents of 10^{-6} A/mm. As a result, for the planar Schottky Devices, the average threshold voltage and the standard variation of the six devices were -11.3 V and 272.9 mV, respectively. In other hands, for the recessed Schottky devices, the average threshold voltage and the standard variation of the seven devices on the same chip were -0.94 V and 16.7 mV, respectively. The variation of threshold voltage of recessed Schottky devices was drastically improved. The result occurred by the uniformity of the residual AlGaN thickness after the self-termination like the recessed Schottky devices. However, the threshold voltage of recessed MIS devices was in the negative bias region compared with the one of recessed Schottky Devices was in the positive bias region. The normally-on operation was due to the positive fixed charge from the defect level or the donor type interface states in the Al_2O_3 film. To reduce the influence and improve the Al_2O_3 and AlGaN interface, Post Metalization Annealing (PMA) treatment was conducted in this experiment and the threshold voltage shifted into the positive bias region after the PMA treatment. To achieve the complete normally-off operation, the optimization of the conditions for the insulator film deposition should be required. To confirm the improved variation visually, the Gaussian fitting was conducted with the obtained average threshold voltage and the standard deviation of the both MIS devices. The threshold voltage of recessed MIS HEMTs had the strong peak in the narrow bias region compared with the broaden curves of planar MIS HEMTs shown as Figs. 6.11.

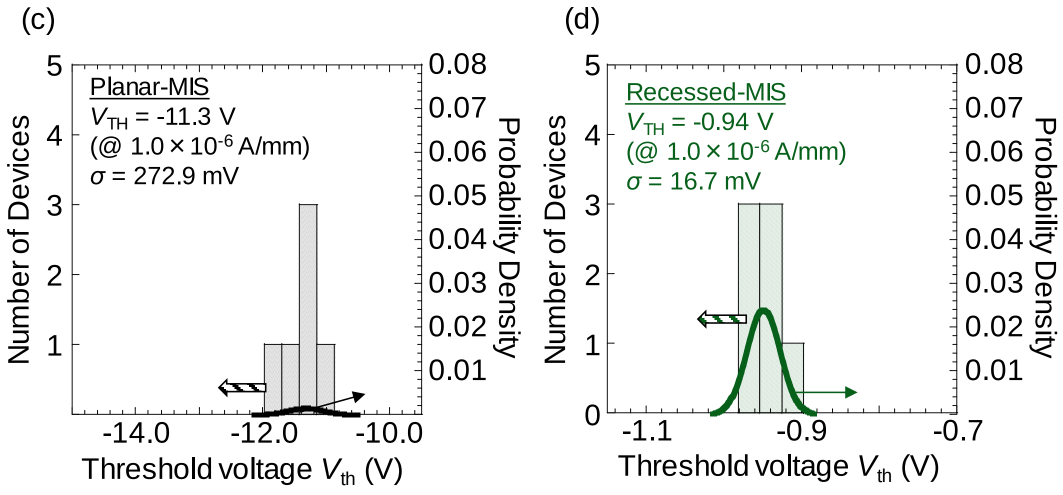

Fig. 6.11. Histograms of the threshold voltage V_{th} valued of AlGaN/GaN HEMTs for (a) six planar-MIS devices, (b) nine recessed-MIS devices.

The fabrication method of recessed gate structure utilizing the self-termination phenomenon had uniformity have been reported in large numbers. Son et al. reported that the AlGaN layer was completely removed by TMAH etching, in which the etching was self-terminated when the underlying GaN layer appeared on the surface 46). They also reported that a small variation in V_{th} with $\sigma = 110$ mV was obtained for fully recessed-gate AlGaN/GaN HEMTs due to uniform etching with self-termination. Another approach to controlling the V_{th} of AlGaN/GaN HEMTs is the regrowth technique, in which the AlGaN layer is grown again after recessed-gate etching is conducted on the AlGaN/GaN heterostructure. Okita et al. reported that the V_{th} of GaN-based gate injection transistors could be controlled by changing the regrowth thickness of the AlGaN layer and that the V_{th} was very small, $\sigma = 63$ mV for a 6 inch substrate 47). The variation of the threshold voltage of 5.46 mV for the recessed Schottky HEMTs and 16.7 mV for the recessed MIS HEMTs in this experiments were very small compared with the reports.

6.6. Conclusion

In this chapter, I reported that I conducted the CL-PEC etching to the AlGaN/GaN heterostructure and evaluate the surface morphology and the electrical characteristics of the each devices fabricated on the etched surface. The residual AlGaN thickness was 6.1 nm after the CL-PEC etching at 40 min measured by AFM. After the TMAH post-treatment at 60 °C for 10 min, the residual ALGaN thickenss didn’t change from before the post-treatment and the RMS roughness was 0.44 nm, which was improved equivalent to the surface roughness before the CL-PEC etching. For the *I*-*V* characteristics of SBDs on the etched surface, the leakage currents was suppressed and the positive shift of threshold voltage for the recessed devices. From the *C*-*V* characteristics of MIS-capacitors, the positive shift of threshold voltage and the improvement of the characteristics uniformity was obtained, and the 2DEG density was calculated. In addition, the residual AlGaN thickness and the Al_2O_3 thickness could be calculated from the obtained capacitance. For the recessed Schottky HEMTs and the recessed MIS HEMTs, the positive shift of the threshold voltage and the suppression of the leakage currents were obtained from the both planar devices. In addition, the drastically improvement of the variation of the threshold voltage was based on the highly uniformity of the residual AlGaN thickness after the self-termination phenomenon. The above results should indicate the CL-PEC etching method is progress for fabrication of the recessed gate structure for AlGaN/GaN HEMTs.

Reference

[1] M. A. Khan, A. Bhattarai, J. N. Kuznia, and D. T. Olson, Appl. Phys. Lett. 63, 1214 (1993).

[2] S. T. Sheppard, K. Doverspike, W. L. Pribble, S. T. Allen, J. W. Palmour, L. T. Kehias, and T. J. Jenkis, IEEE Electron Device Lett. 20, 161 (1999).

[3] U. K. Mishra, L. Shen, T. E. Kazior and Y. F. Wu, Proc. IEEE 96, 287(2008).

[4] A. S. A. Fletcher, and D. Nirmal, Superlattices and Microstructures 109, 519 (2017).

[5] J. Burm, W. J. Schaff, G. H. Martin, L. F. Eastman, H. Amano, and I. Akasaki, Solid-State Electron. 41, 247 (1997).

[6] W. Saito, Y. Takada, M. Kuraguchi, K. Tsuda, and I. Omura, IEEE Tras. Electron Devices 53, 356 (2006).

[7] J. W. Chung, W. E. Hoke, E. M. Chumbes, and T. Palacios, IEEE Electron. Device Lett. 31, 195 (2010).

[8] F. Roccaforte, G. Greco, P. Fiorenza, and F. Iucolano, Materials 12, 1599 (2019).

[9] X. A. Cao, H. Cho, S. J. Pearton, G. T. Dang, A. P. Zhang, F. Ren, R. J. Shul, L. Zhang, R. Hickman, and J. M. V. Hove, Appl. Phys. Lett. 75, 232 (1999).

[10] T. Hashizume, and R. Nakasaki, Appl. Phys. Lett 80, 4564 (2002).

[11] Z. Mouffak, A. Bensaoula, and L. Trombetta, J. Appl. Phys. 95, 727 (2004).

[12] K. Tang, W. Huang, and T. P. Chow, J. Electron Mater. 38, 523 (2009).

[13] Z. Yatabe, J. T. Asubar, and T. Hashizume, J. Phys. D: Appl. Phys. 49, 393001 (2016).

[14] N. M. Shrestha, Y. Li, T. Suemitsu, and S. Samukawa, IEEE Tras. Electron Devices 66, 1694 (2019).

[15] M. S. Minsky, M. White, and E. L. Hu, Appl. Phys. Lett. 68, 1531 (1996).

[16] C. Youtsey, I. Adesida, L.T. Romano, and G. Bulman, Appl. Phys. Lett. 72, 560 (1998).

[17] L. H. Peng, C. W. Chuang, J. K. Ho, C. N. Hunag, and C. Y. Chen, Appl. Phys. Lett. 72, 939 (1998).

[18] I. M. Huygens, K. Strubbe, and W. P. Gomes, J. Electrochem. Soc. 147, 197 (2000).

[19] T. Rotter, D. Mistele, J. Stemmer, F. Fedler, J. Aderhold, J. Graul, V. Schwegler, C. Kirchner, M. Kamp, and M. Heuken, Appl. Phys. Lett. 76, 3923 (2000).

[20] C. H. Ko, Y. K. Su, S. J. Chang, W. H. Lan, J. Webb, M. C. Tu, and Y. T. Cherng, Mater. Sci. Eng. B 96, 43 (2002).

[21] F. Horikiri, Y. Narita, and T. Yoshida, Jpn. J. Appl. Phys. 57, 086502 (2018).

[22] F. Horikiri, H. Ohta, N. Asai, Y, Narita, T. Yoshida, and T. Mishima, Appl. Phys. Express. 11, 091001 (2018).

[23] S. Matsumoto, M. Toguchi, K. Takeda, T. Narita, T. Kachi, and T. Sato, Jpn. J. Appl. Phys. 57, 121001 (2018).

[24] N. Asai, H. Ohta, F. Horikiri, Y. Narita, T. Yoshida, and T. Mishima, Jpn. J. Appl. Phys. 58, SCCD05 (2019).

[25] Y. L. Chiou, L. H. Huang, and C. T. Lee, IEEE Electron Device Lett. 31, 183 (2010).

[26] Z. Zhang, S. Qin, K. Fu, G. Yu, W. Li, X. Zhang, S. Sun, L. Song, S. Li, R. Hao, Y. Fan, Q. Sun, G. Pan, Y. Cai, and B. Zhang, Appl. Phys. Express 9, 084102 (2016).

[27] Y. Kumazaki, K. Uemura, T. Sato, and T. Hashizume, J. Appl. Phys. 121, 184501 (2017).

[28] K. Uemura, M. Deki, Y. Honda, H. Amano, and T. Sato, Jpn. J. Appl. Phys. 58, SCCD20 (2019).

[29] J. A. Bardwell, I. G. Foulds, J. B. Webb, H. Tang, J. Fraser, S. Moisa, and S. J. Rolfe, J. Electron. Mater. 28, L24 (1999).

[30] H. Maher, D. W. DiSant, G. Soerenesen, C. R. Bolognesi, H. Tang, and J. B. Webb, Appl. Phys. Lett. 77, 3833 (2000).

[31] H. Maher, D. W. DiSant, M. W. Dvorak, G. Soerensen, C. R. Bolognesi, J. A. Bardwell, H. Tang, and J. B. Webb, Electron. Lett. 36, 1969 (2000).

[32] J. A. Bardwell, J. B. Webb, H. Tang, J. Fraser, and S. Moisa, J. Appl. Phys. 89, 4142 (2001).

[33] R. T. Green, W. S. Tan, P. A. Houston, T. Wang, and P. J. Parbrook, J. Electron. Mater. 36, 397 (2007).

[34] J. L. Weyher, F. D. Tichelaar, D. H. van Dorp, J. J. Kelly, and A. Khachapuridze, J. Cryst. Growth 312, 2607 (2010).

[35] S. Lee, S. Mishkat-Ul-Masabih, J. T. Leonard, D. F. Feezell, D. A. Cohen, J. S. Speck, S. Nakamura, and S. P. DenBaars, Appl. Phys. Express 10, 011001 (2017).

[36] F. Horikiri, N. Fukuhara, H. Ohta, N. Asai, Y. Narita, T. Yoshida, T. Mishima, M. Toguchi, K. Miwa, H. Ogami, and T. Sato, Appl. Phys. Express 13, 046501 (2020).

[37] Z. H. Hwang, J. W. Hwang, H. L. Hwang, and W. H. Hung, Appl. Phys. Lett. 84, 3759 (2004).

[38] D. H. van Dorp, J. L. Weyher, M. R. Kooijman, and J. J. Kelly, J. Electrochem. Soc. 156, D371 (2009).

[39] F. Horikiri, N. Fukuhara, H. Ohta, N. Asai, Y. Narita, T. Yoshida, T. Mishima, M. Toguchi, K. Miwa, and T. Sato, IEEE Trans. Semicond. Manuf. 32, 489 (2019).

[40] F. Horikiri, N. Fukuhara, H. Ohta, N. Asai, Y. Narita, T. Yoshida, T. Mishima, M. Toguchi, K. Miwa, and T. Sato, Appl. Phys. Express 12, 031003 (2019).

[41] K. Miwa, Y. Komatsu, M. Toguchi, F. Horikiri, N. Fukuhara, Y. Narita, O. Ichikawa, R. Isono, T. Tanaka, and T. Sato, Appl. Phys. Express 13, 026508 (2020).

[42] M. Toguchi, K. Miwa, F. Horikiri, N. Fukuhara, Y. Narita, T. Yoshida, and T. Sato, Appl. Phys. Express 12, 066504 (2019).

[43] Y.Ando, S. Kaneki, and T. Hashizume, Appl. Phys. Express 12, 024002 (2019).

[44] O. Ambacher, J. Smart, J. R. Shealy, N. G. Weimann, K. Chu, M. Murphy, W. J. Schaff, and J. F. Eastman, J. Appl. Phys. 85, 3222 (1999).

[45] T. H. Hung, S. Krishnamoorthy, M. Esposto, D. N. Nath, P. S. Park, and S. Rajan, Appl. Phys. Lett. 102, 072105 (2013).

[46] D.H. Son, Y.W. Jo, C.H. Won, J.H. Lee, J.H. Seo, S.H. Lee, J.W. Lim, J.H. Kim, I.M. Kang, S. Cristoloveanu, J.H. Leea, Solid. Stat. Electron. 141, 7 (2018).

[47] H.Okita, M.Hikita, A.Nishio, T.Sato, K.Matsunaga, H.Matsuo, M.Tsuda, M.Mannoh, S.Kaneko, M.Kuroda, M.Yanagihara, A.Ikoshi, T.Morita, K.Tanaka, and Y.Uemoto, IEEE Tras. Electron Devices 64, 1026 (2017).

Chapter 7

Conclusion

In this paper, we focused on "photoelectrochemical (PEC) etching" as a new low-damage etching technique instead of dry etching, and investigated its application to nitride semiconductor electronic device fabrication processes. Specifically, for GaN and AlGaN nitride semiconductors, we clarified the photoelectrochemical characteristics of the electrolyte/nitride semiconductor interface, and developed an "anisotropic etching technique" for forming trench structures with high aspect ratios, a "recessed etching technique" for precisely controlling the threshold voltage of transistors, and an "etching technique" for improving the compatibility with existing contactless PEC etching process," which simplifies the electrochemical cell to improve its compatibility with existing semiconductor device processes. In particular, we found "etching self-stop phenomenon" in contactless PEC etching for AlGaN/GaN heterostructure, and achieved higher process controllability than conventional dry etching technology. The developed technique was applied to the fabrication process of recessed-gate AlGaN/GaN HEMTs, and its usefulness was discussed.

Chapter 4 shows the analyzed results of the electric field absorption effect observed at the electrolyte/GaN interface and developed an anisotropic PEC etching technique for GaN using this effect. By calculating the change in the optical absorption coefficient at each wavelength based on the potential barrier generated at the electrolyte/GaN interface and reproducing the experimental values of photocurrent values, we demonstrated that the Franz-Keldysh (F-K) effect occurs at the interface. We also applied the developed anisotropic PEC etching technique to initially processed low-donor-density GaN samples, and discussed the structural control and its usefulness for the formation of trench structures with high aspect ratio.

Chapter 5 shows the results that contactless PEC (CL-PEC) etching using acidic aqueous solution containing sulfuric acid radicals ($SO^{4\cdot-}$) was developed, and the results of applying it to the etching of GaN monolayer were presented. The results of the CL-PEC etching of GaN using acidic aqueous solutions containing $S_2O_8^{2-}$/$SO4^{\cdot -}$ are shown. It was clarified that the production rate of $SO4^{\cdot -}$, which is directly related to the etching rate, was demonstrated to be the same for both solutions by experiments and theoretical analysis, and the flatness of the etched surface was also confirmed to be the same. In addition, we demonstrated that the development of acid-based solutions can directly use positive photoresists as etching masks, which dramatically increases their suitability for existing device processes.

Chapter 6 shows the results that based on the results of Chapter 5, recessing of AlGaN/GaN heterostructures was performed using CL-PEC etching, and the surface conditions after etching and the electrical characteristics of various devices fabricated on the etched surface were evaluated. We found that the etching stopped in the middle of the upper layer of AlGaN (self-stop phenomenon) after recess processing by CL-PEC etching, and the remaining thickness of AlGaN at that time showed high uniformity within the sample surface. As a result of electrical characterization, Schottky-Barrier diodes, MIS-capacitors, Schottky-HEMTs and MIS-HEMTs fabricated on the recessed surface showed a decrease in leakage current compared to the devices fabricated on the non-recessed surface, and the threshold voltage increased in the positive direction as designed by the recess fabrication. The threshold voltage shifts positively as per the recess fabrication design. Furthermore, we found that the CL-PEC etching significantly improved the uniformity of device characteristics and discussed the factors behind this. From these results, it is shown that this etching method is promising as a nitride semiconductor device process.

Research achievements

Publications:

Journal papers (Thesis-related)

[1] M.Toguchi, K.Miwa, F.Horikiri, N.Fukuhara, Y.Narita, O.Ichikawa, R.Isono, T.Tanaka, and T.Sato: "Self-terminating contactless photo-electrochemical (CL-PEC) etching for fabricating highly uniform recessed-gate AlGaN/GaN high-electron-mobility transistors (HEMTs)", J. Appl. Phys., Vol.130, No.2, pp.024501-1-10 (2021) (IF=2.546, TC=0)

[2] M.Toguchi, K.Miwa, and T.Sato: "Communication-Anisotropic Electrochemical Etching of Porous Gallium Nitride by Sub-Bandgap Absorption Due to Franz-Keldysh Effect", J. Electrochem. Soc., Vol.166, No.12, H510-H512 (2019) (IF=4.316, TC=1)

[3] M.Toguchi, K.Miwa, F.Horikiri, N.Fukuhara, Y.Narita, T.Yoshida, and T.Sato: "Electrodeless photo-assisted electrochemical etching of GaN using a H3PO4-based solution containing S2O82- ions", Appl. Phys. Express, Vol.12, No.6, pp.066504-1-4 (2019) (IF=2.895, TC=9)

Journal papers (Others)

[1] 佐藤 威友, 渡久地 政周 :「2 段階エッチング法を用いたポーラス窒化ガリウム(GaN)の形成とその光学特性の制御」, 電気化学, 89 巻 4 号, pp.365-369 (2021).

[2] M.Shimauchi, K.Miwa, M.Toguchi, T.Sato and J.Motohisa: "Fabrication of GaN nanowires containing n(+)-doped top layer by wet processes using electrodeless photo-assisted electrochemical etching and alkaline solution treatment", Vol.14, No.11, pp.111003-1-4, (2021).

[3] F.Horikiri, N.Fukuhara, H.Ohta, N.Asai, Y.Narita, T.Yoshida, T.Mishima, M.Toguchi, K.Miwa, H.Ogami and T.Sato: "Thermal-assisted contactless

photoelectrochemical etching for GaN", Vol.13, No.4, pp.046501-1-5, (2020).

[4] K.Miwa, Y.Komatsu, M.Toguchi, F.Horikiri, N.Fukuhara, Y.Narita, O.Ichikawa, R.Isono, T.Tanaka, T.Sato: "Self-termination of contactless photo-electrochemical (PEC) etching on aluminum gallium nitride/gallium nitride heterostructure", Vol.13, No.2, pp.026508-1-4 (2020).

[5] F.Horikiri, N.Fukuhara, H.Ohta, N.Asai, Y.Narita, T.Yoshida, T.Mishima, M.Toguchi, K.Miwa and T.Sato: "Photoelectrochemical Etching Technology for Gallium Nitride Power and RF Devices", Vol.32, No.4, pp.489-495 (2019).

[6] T.Sato, M.Toguchi, Y.Komatsu, and K.Uemura: "Low-Damage Etching for AlGaN/GaN HEMTs Using Photo-Electrochemical Reactions," IEEE Trans. Semicond. Manuf., Vol.32, No.4, pp.483-488 (2019).

[7] F.Horikiri, N.Fukuhara, H.Ohta, N.Asai, Y.Narita, T.Yoshida, T.Mishima, M.Toguchi, K.Miwa, T.Sato: "Simple wet-etching technology for GaN using an electrodeless photo-assisted electrochemical reaction with a luminous array film as the UV source", Vol.12, No.3, pp.031003-1-6 (2019).

Conferences:

International conferences

[1] M.Toguchi, K.Miwa, F.Horikiri, N.Fukuhara, Y.Narita, O.Ichikawa, R.Isono, T.Tanaka, and Taketomo Sato: "Fabrication of Recessed-Gate AlGaN/GaN HEMTs Utilizing Contactless Photo-Electrochemical (CL-PEC) Etching", 2020 Pacific Rim Meeting on Electrochemical and Solid State Science (PRiME 2020), H01-1818, Online, October 4-9, 2020.

[2] M.Toguchi, K.Miwa, F.Horikiri, N.Fukuhara, Y.Narita, T.Yoshida, and T.Sato: "Contactless Photoelectrochemical Etching of n-GaN in $K_2S_2O_8$ solution", Materials Research Meeting 2019, D4-11-P05, Kanagawa, Japan, December 10-14, 2019.

[3] M.Toguchi, K.Miwa, F.Horikiri, N.Fukuhara, Y.Narita, T.Yoshida, and T.Sato: "Evaluation of Radical Production Rate from $S_2O_8^{2-}$ ions for GaN etching", The 9th Asia-Pacific Workshop on Widegap Semiconductors (APWS2019), TuP-ED-5, Okinawa, Japan, November 10-15, 2019.

[4] M.Toguchi, K.Miwa, F.Horikiri, N.Fukuhara, Y.Narita, T.Yoshida, and T.Sato: "Electrochemical Characterization on n-type GaN for Simple wet-etching utilizing $S_2O_8^{2-}$ containing solution", 13th International Conference on Nitride Semiconductors, EP01.08, Bellevue, Washington, USA, July 7-12, 2019.

[5] M.Toguchi and T.Sato: “Formation of GaN Porous Structures and Control in Pore Depth Utilizing Anodic Etching with Specific Photoabsorption”, 3rd International Symposium on Anodizing Science and Technology, O-26, Awaji Island, Hyogo, Japan, June 2-5, 2019.

[6] M.Toguchi, S.Matsumoto, and T.Sato: “Control of Pore Depth in GaN Porous Structures Utilizing a Photoabsorption Process Under below-Bandgap Illumination”, 233rd ECS Meeting, Seattle Sheraton and Washington State Convention Center, Seattle, USA, May 13-17, 2018.

[7] M.Toguchi, S.Matsumoto, and T.Sato: “Photo-electrochemical Formation of Porous Nanostructures on n-type GaN utilizing Franz-Keldysh Effect”, The 8th International Symposium on Surface Science, Tsukuba International Congress Center, Tsukuba, Japan, October 22-26, 2017.

Domestic conferences (in Japanese)

[1] 渡久地 政周, 三輪 和希, 堀切 文正, 福原 昇, 成田 好伸, 市川 磨, 磯野 僚多, 田中 丈士, 佐藤 威友 :「低損傷コンタクトレス光電気化学エッチングを利用したリセスゲートAlGaN/GaN HEMTsの作製」, 2021年電子デバイス研究会（ED）, ED2021-34, オンライン開催, 11月25日-26日, 2021 年.

[2] 渡久地 政周, 三輪 和希, 堀切 文正, 福原 昇, 成田 好伸, 市川 磨, 磯野 僚多, 田中 丈士, 佐藤 威友 :「コンタクトレス光電気化学エッチングによるリセスゲートAlGaN/GaN HEMT の作成 (2)」, 2021年 第68回 応用物理学会春季学術講演会, 19p-Z25-3, オンライン開催, 3月16日-19日, 2021 年.

[3] 渡久地 政周, 三輪 和希, 堀切 文正, 福原 昇, 成田 好伸, 吉田 丈洋, 佐藤 威友 :「K2S2O8/H3PO4 混合溶液を用いた n-GaN のコンタクトレスエッチング」, 2019年 第80回 応用物理学会秋季学術講演会, 21a-E301-3, 北海道大学 札幌キャンパス, 北海道札幌市, 9月18日-21日, 2019 年.

[4] 渡久地 政周, 三輪 和希, 堀切 文正, 福原 昇, 成田 好伸, 吉田 丈洋, 佐藤 威友 :「ペルオキソ二硫酸イオン（S2O82-）含有電解液におけるGaNの電気化学特性」, 2019年 第66回 応用物理学会春季学術講演会, 10a-M121-7, 東京工業大学 大岡山キャンパス, 東京都目黒区, 3月9日-12日, 2019 年.

[5] 渡久地 政周, 武田 健太郎, 佐藤 威友 :「窒化ガリウム加工基板に対する選択的光電気化学エッチングの検討」, 2018年電気化学秋季大会, 1L16, 金沢大学角間キャンパス, 石川県金沢市, 9月25日-26日, 2018年.

[6] 12) 渡久地 政周, 松本 悟, 佐藤 威友 :「表面加工を施した窒化ガリウムの特異的光吸収特性と光電気化学エッチングの制御」, 2018 年 電気化学会第 85 回大会, 1L07, 東京理科大学葛飾キャンパス, 東京都葛飾区, 3 月 9 日−11 日, 2018 年.

[7] 14) 渡久地 政周, 佐藤 威友 :「Franz-Keldysh 効果を用いた窒化ガリウムの光電気化学反応制御」, 2017 年電気化学会秋季大会, 1L30, 長崎大学文教地区キャンパス, 長崎市, 9 月 10 日−11 日, 2017 年.

Patent (in Japanese):

[1] 発明者：堀切文正、福原昇、佐藤威友、渡久地政周、「構造体の製造方法と製造装置および中間構造体」、特許出願番号：2019-86053、特許番号：特許第 6694102 号、令和 1 年 8 月 14 日出願